University of California
Santa Barbara

Improved Methods for Oceanographic High Frequency Radars

A dissertation submitted in partial satisfaction
of the requirements for the degree

Doctor of Philosophy
in
Mechanical Engineering

by

Brian Michael Emery

Committee in charge:

Professor Libe Washburn, Chair
Professor Eckart Meiburg
Professor Igor Mezić
Professor Frédéric Gibou
Professor Shivkumar Chandrasekaran

March 2018

The Dissertation of Brian Michael Emery is approved.

Professor Eckart Meiburg

Professor Igor Mezić

Professor Frédéric Gibou

Professor Shivkumar Chandrasekaran

Professor Libe Washburn, Committee Chair

March 2018

Improved Methods for Oceanographic High Frequency Radars

by

Brian Michael Emery

For Eliza, Cormick, and Abigale - and their bright future.

Acknowledgements

I have many people to thank for the data, support, assistance, and encouragement that I received in getting to this point. I feel very fortunate to have had the opportunity to take on a Ph.D. at this 'advanced' stage in my career. Without the backing and consent that I received along the way, it would not have been possible. Before saying thanks, I must acknowledge funding agencies, publishers and coauthors with the appropriate language.

Chapter 2 previously appeared in the Journal of Oceanic and Atmospheric Technology [1]. The American Meteorological Society holds the copyright, and the work is used here with permission. The chapter is based upon work supported by the United States Department of Commerce under contract WC133R10CN0212, and benefited from the U. S. Integrated Ocean Observing System Program Office's HF Radar support. Any opinions, findings, conclusions or recommendations expressed in this publication are those of the author(s) and do not necessarily reflect the views of the Department of Commerce.

Chapters 3 and 4 are based in part upon work supported by the National Science Foundation under Grant Number OCE-1658475. Any opinions, findings, and conclusions or recommendations expressed in this material are those of the authors and do not necessarily reflect the views of the National Science Foundation

Preliminary results from Chapter 4 were published in the Proceedings for the 2016 IEEE Conference on Antenna Measurements & Applications (CAMA) [2].

Chapter 2 benefited from the AIS data obtained from Megan McKenna and John Hildebrand, both associated with Scripps Institution of Oceanography. Without being aware of AIS, I would have never had the idea to use it in the research that became this chapter.

The content of Chapter 2 resulted from a collaboration with Don Barrick, and Chad

Whalen of Codar Ocean Sensors Ltd., and with Jack Harlan of the National Oceanic and Atmospheric Administration, who appear as co-authors of the publication. Working with them was an honor and a privilege, and their efforts where instrumental in obtaining SBIR funds to make the idea a reality.

Along with Don Barrick, I would like to thank Bill Rector, also of Codar Ocean Sensors, Ltd., for providing the simulation software used in [3], which provided a significant head start for what became the simulation software used in Chapters 3 and 4. I am also grateful for many helpful discussions early in the analysis stage.

The boat operations to measure antenna patterns where run by David Salazar, Cristoph Pierre and Eduardo Romero. David Salazar, Eduardo Romero, and Cyril Johnson where essential in operating and improving the HF radar sites. The intellectually free and stimulating work environment we have together improved this work in countless ways.

Chapters 3 and 4 were improved through the joint proposal writing and associated discussions with Anthony Kirincich of Woods Hole Oceanographic Institution, with whom it has been a great pleasure to collaborate.

In the Mechanical Engineering department, I must thank Laura Reynolds and Frédéric Gibou for the excellent support and guidance I received as a graduate student. I am proud to have been a part of their excellent program.

As a simultaneous student and staff throughout this process, I frequently pushed the limits of the bureaucracy at UCSB, and thus I am very grateful for the patience and expertise of the administrative staff. At the Marine Science Institute, Luisa Velez, Veronica Perez and Tim Schmidt made things happen when they needed to happen. The assistance of Edna Arellano in human resources was invaluable for navigating the tuition payment maze. I am indebted to them all.

I am incredibly impressed with the members of my committee, and am very grateful

to have had the opportunity to work with them either as a student in their classes, or in collaboration. The excellence of the department is a direct outcome of their dedication to it.

Previous to my time as a student, I had the pleasure to work with Sally MacIntyre, whose excitement and enthusiasm for science is highly contagious. Her encouragement played a major role in my decision to become a Ph.D. student.

I am at a loss for words for how to thank Libe Washburn, who serve as my committee chair, mentor, advisor, and primary supervisor throughout this process. Without his support and approval - and the financial backing he made possible - this would have never happened.

Finally, the support of my wife, Katherine Emery was essential. I am grateful for her encouragement, and for her efforts with our children during the many long days and nights over the last few years.

Curriculum Vitæ

Brian Michael Emery

Education

2018	Ph.D. University of California Santa Barbara, Mechanical Engineering
1996	M.S. University of California Santa Barbara, Mechanical Engineering
1992	B.S. University of California Santa Barbara, Physics

Publications

1. Zhang, Wei, Naoto Ebuchi, Yasushi Fukamachi, Feng Cheng, Kay I Oshima, **Brian Emery** Takenobu Toyota, Hiroto Abe, Kunio Shirasawa. "Sea Ice Observation by High-Frequency Ocean Radar", Manuscript submitted for publication (2018).
2. Washburn, Libe, Eduardo Romero, Cyril Johnson, **Brian Emery**, and Chris Gotschalk. "Measurement of antenna patterns for oceanographic radars using aerial drones." Journal of Atmospheric and Oceanic Technology 34, no. 5 (2017): 971-981.
3. **Emery, Brian**, Libe Washburn, Chad Whelan, Don Barrick, and Jack Harlan. "Measuring antenna patterns for ocean surface current HF radars with ships of opportunity." Journal of Atmospheric and Oceanic Technology 31, no. 7 (2014): 1564-1582.
4. MacIntyre, Sally, José R. Romero, Gregory M. Silsbe, and **Brian M. Emery**. "Stratification and horizontal exchange in Lake Victoria, East Africa." Limnology and Oceanography 59, no. 6 (2014): 1805-1838.
5. Ohlmann, J. Carter, Joe H. LaCasce, Libe Washburn, Arthur J. Mariano, and **Brian M. Emery**. "Relative dispersion observations and trajectory modeling in the Santa Barbara Channel." Journal of Geophysical Research: Oceans 117, no. C5 (2012).
6. Ohlmann, Carter, Peter White, Libe Washburn, **Brian Emery**, Eric Terrill, and Mark Otero. "Interpretation of coastal HF radarderived surface currents with high-resolution drifter data." Journal of Atmospheric and Oceanic Technology 24, no. 4 (2007): 666-680.
7. **Emery, Brian M.**, Libe Washburn, Milton S. Love, Mary M. Nishimoto, and J. Carter Ohlmann. "Do oil and gas platforms off California reduce recruitment of bocaccio (Sebastes paucispinis) to natural habitat? An analysis based on trajectories derived from high-frequency radar." Fishery Bulletin 104, no. 3 (2006): 391-400.

8. **Emery, Brian M.**, Libe Washburn, and Jack A. Harlan. "Evaluating radial current measurements from CODAR high-frequency radars with moored current meters." Journal of Atmospheric and Oceanic Technology 21, no. 8 (2004): 1259-1271.
9. Washburn, Libe, **Brian M. Emery**, Burton H. Jones, and Daniel G. Ondercin. "Eddy stirring and phytoplankton patchiness in the subarctic North Atlantic in late summer." Deep Sea Research Part I: Oceanographic Research Papers 45, no. 9 (1998): 1411-1439.

Grants

1. NSF Collaborative Research: Resolving complex coastal flows via advances in high-frequency radar, Co-PI, $536,279.
2. Satomi Family Graduate Dissertation Fellowship, 2017, $4,500.
3. NOAA Fellowship Automated Comparisons for IOOS HF Radar Quality Control, 2017, $25,970.
4. NOAA Fellowship Automated Comparisons for IOOS HF Radar Quality Control, 2016, $85,620.
5. NOAA Fellowship Automated Comparisons for IOOS HF Radar Quality Control, 2015, $83,125.
6. Ralph M. Parsons Foundation Fellowship, 2014, $4,074.
7. NOAA SBIR Phase II, 2011. HF Radar Calibration with Automatic Identification System Ships of Opportunity, $399,883.
8. NOAA SBIR Phase I, 2010. Ocean Current Radar Calibration with Ships of Opportunity and the Automatic Identification System, $94,977.

Proceedings and Reports

1. Emery, B.M. and Washburn, L., 2016 Improved direction of arrival methods for oceanographic HF radars, In Antenna Measurements & Applications (CAMA), 2016 IEEE Conference on (pp. 1-4). IEEE.
2. Washburn, L., Romero, E., Johnson, C., Gotschalk, C. and Emery, B., 2016, Antenna calibration for oceanographic radars using aerial drones, In Antenna Measurements & Applications (CAMA), 2016 IEEE Conference on (pp. 1-4). IEEE.
3. Emery, B. and L. Washburn, Automated Comparisons for IOOS HF Radar Quality Control, NOAA IOOS Final Report, October, 2016.
4. Whelan, C., Emery, B., Teague, C., Barrick, D., Washburn, L., and J. Harlan, 2012, Automatic calibrations for improved quality assurance of coastal HF radar currents, Oceans 2012 IEEE/MTS, 14-19 Oct. 2012, doi: 10.1109/OCEANS.2012.6405104.

5. Emery, B. M., and S. MacIntyre, Expanding observations of mixing in Toolik Lake with the North American Regional Reanalysis, NSF Arctic LTER final report contribution, 2011.
6. Emery, B. M. and L. Washburn, Evaluation of SeaSonde Hardware Diagnostic Parameters as Performance Metrics, NOAA IOOS final report, October 2007.
7. Emery B. M., K. E. Laws, L. Washburn, and J. D. Paduan, Error Characterization in High Frequency Radar Ocean Surface Current Observations, NOAA IOOS final report, January 2007.
8. Emery, B.M., L. Washburn, and J.A. Harlan, 2003, Evaluating radial component current measurements from CODAR high frequency radars and moored in situ current meters, Proceedings of the First International Radiowave Oceanography Workshop, Timberline Lodge, OR, 9-12 April.
9. Washburn, L., E. H. Beckenbach, B. M. Emery, and J.A. Harlan, 2003, HF radar observations of surface currents in the vicinity of Pt. Conception California, Proceedings of the First International Radiowave Oceanography Workshop, Timberline Lodge, OR, 9-12 April.

Oral Presentations

1. Emery, B. and L. Washburn, Alternative Direction Finding Methods for Oceanographic HF Radars, IOOS HF Radar Townhall, AGU Ocean Sciences Meeting, Portland, OR, 11-16 Feb. 2018.
2. Emery, B. and L. Washburn, Alternative Direction Finding Methods for Oceanographic HF Radars, Radiowave Oceanography Workshop, Lüneburg, Germany, 18 Sept. 2017.
3. Emery, B., L. Washburn and J. Harlan, Automated Comparisons for Quality Control, Radiowave Operators Working Group (ROWG-9), Galveston, TX, 14-15 March 2107.
4. Emery, B., and L. Washburn, Improved Direction of Arrival Methods for Oceanographic HF Radars, IEEE Conference on Antenna Measurements and Applications (CAMA), Syracuse NY, 23-27 Oct. 2016.
5. Emery, B., Improved Methods for Oceanographic HF Radars, ME Grad Slam Event, 2016 Mechanical Engineering Annual Convocation, University of California, Santa Barbara, Oct. 12, 2016.
6. Emery, B., L. Washburn, and K. Brown, Improving Uncertainty Estimates for Radial Current Observations, Radiowave Oceanography Workshop, Woods Hole Oceanographic Institution, 4 Nov. 2015.
7. Emery, B., L. Washburn, C. Whelan, C. Teague, and D. Barrick, Calibration of Ocean Current Mapping HF Radars, Center for Interdisciplinary Research in Fluids (CIRF), College of Engineering, Univ. of Calif. Santa Barbara, 22 January 2014.

8. Emery, B., L. Washburn, C. Whelan and D. Barrick, Measuring Antenna Patterns from AIS Ships of Opportunity, ROWG 6, Nov. 2012, University of South Florida.
9. Washburn, L., B. Emery, C. Johnson, and C. Ohlmann, Oceanographic applications and developments in hardware and software using an array of high frequency radars in the Southern California Coastal Ocean Observing System, Radiowave Oceanography Workshop 10, Sept. 26-29, 2010.
10. Emery, B., M. Nishimoto, L. Washburn, and M. Love, Do oil and gas platforms off California reduce recruitment of Bocaccio (Sebastes paucispinis) to natural habitat? An analysis based on trajectories derived from high frequency radar, ROWG 4, Old Dominion University (Norfolk, VA) June 2-4, 2009.
11. Emery, B., A Review of ROWG 2, ROWG 3, Sept, 2007, Scripps Institution of Oceanography, San Diego, CA.

Poster Presentations

1. Emery, B., and L. Washburn, Uncertainty Estimates for HF Radar Coastal Ocean Currents, Ocean Sciences Meeting, Portland, OR, 11-16 Feb. 2018.
2. Emery, B., and L. Washburn, Oil Spill Trajectories from HF Radars: Investigating Alternatives to MUSIC for Oceanographic HF Radars, AGU Fall Meeting, San Francisco, CA, Dec. 2016.
3. Emery, B., L. Washburn, L., I. Mezic, H. Arbabi, S. Loire, C. Ohlmann, and J. Harlan, Oil Spill Trajectories from HF Radars: Lagrangian Stochastic Model and Applied Dynamical Systems Methods, AGU Ocean Sciences, New Orleans, LA, Feb. 2016.
4. Washburn, L., E.Romero, C. Johnson, B. Emery and C. Gotschalk, New Applications for Autonomous Aerial Vehicles (Drones) in Coastal Oceanographic Research, AGU Ocean Sciences, New Orleans, LA, Feb. 2016.
5. MacIntyre, S., J. P. Fram, Paul J. Kushner, and B. Emery, Effects of Large Scale Forcing on Thermal Regime and Mixing Dynamics of Lakes in the Alaskan Arctic, LTER All Scientists Meeting, Estes Park, CO, September 2012.
6. Emery, B., L. Washburn, D. Barrick, and C. Whelan, Antenna Patterns from AIS Ships of Opportunity, ROWG 5, Santa Barbara, CA, April, 2011.
7. MacIntyre, S., A. Jonsson, M. Jansson, J. Aberg, D. Turney, B. Emery, and S. Miller, Buoyancy Flux, Turbulence, and the Gas Transfer Coefficient in a Stratified Lake, AGU Fall Meeting, San Francisco, CA, December, 2010.
8. Reams, E., C Johnson, B. Emery, and L Washburn, Liquid Cooling for a SeaSonde Transmitter, ROWG 3, Scripps Institution of Oceanography, San Diego, CA, Sept., 2007.

9. Johnson, C., B. Emery, and L Washburn, Custom Transmit Antennas for SeaSondes, ROWG 3, Scripps Institution of Oceanography, San Diego, CA, Sept, 2007.
10. Yu, G., B. Emery, and L Washburn, Effects of Antenna Pattern Smoothing on SeaSonde Radial Data, ROWG 3, Scripps Institution of Oceanography, San Diego, CA, Sept, 2007.

Professional Service

- Reviewer, International Journal of Remote Sensing (1)
- Reviewer, Journal of Atmospheric and Oceanic Technology (4)
- Reviewer, Marine Technology Society Journal (1)
- Reviewer, IEEE Journal of Oceanic Engineering (1)

Activities

- Steering Committee Member, Radiowave Operators Working Group (ROWG), 2004-present
- Participant, Learning From Data telecourse, California Institute of Technology, spring 2012
- Radiowave Operators Working Group ROWG-5 Workshop Host, Santa Barbara, CA, 2011

Published Code

https://github.com/brianemery

https://github.com/rowg/hfrp_additions

Other

Citation data: http://scholar.google.com/citations?user=n3JbRg0AAAAJ

ORCID: 0000-0001-5760-6722

QAQC website http://hfradar.msi.ucsb.edu/comparisons/

Abstract

Improved Methods for Oceanographic High Frequency Radars

by

Brian Michael Emery

HF radars measure coastal ocean surface currents with a spatial and temporal resolution that remain unmatched by other approaches. Because they observe the scientifically and economically important coastal zone, these radars often form an integral part of coastal ocean observing systems. Thus, improvements to the techniques they employ and the data they produce would have far reaching impacts.

Several opportunities exist to improve HF radar data. First, idealized antenna patterns are widely used despite the fact that the most accurate observations are obtained when the radars use measured antenna patterns. Second, the radars produce maps of surface current velocities without estimates of the measurement uncertainties. Third, advances in signal processing techniques over the last few decades have not been evaluated for use with these radars.

To simplify and automate the antenna pattern measurement (APM), a method is presented for obtaining antenna pattern measurements for HF radars from ships of opportunity. Positions obtained from the Automatic Identification System (AIS) are used to identify signals backscattered from ships in ocean current radar data. The ship signal and ship position data are then combined to determine the APM. Data screening methods are developed and shown to produce APMs with low error when compared with APMs obtained with standard approaches.

To produce estimates of uncertainty in the surface current observations, a method to estimate uncertainty in the radar directional measurement [4] is identified and combined

with previous results to produce an estimate of the uncertainty in the radial component observations produced by individual HF radars. The method is evaluated with radar simulations that incorporate complex ocean current scenarios. These simulations suggest processing modifications that inform the application to observational data. Uncertainty estimates are further evaluated using archive data from two operational HF radars. Results from these radars suggest that the uncertainty estimates can be used for data quality control, and would be suitable for incorporation into numerical models.

Finally, an evaluation of alternative signal processing techniques suggests that significant improvements in spatial coverage are possible. Oceanographic HF radars typically employ Multiple Signal Classification (MUSIC) for direction of arrival (DOA) estimation. Signal processing literature suggests that several alternative DOA methods may provide advantages over MUSIC when applied to HF radars, which attempt to resolve complex and dynamic flows given poor signal conditions and constrained antenna designs. Results of radar simulations suggest that the Maximum Likelihood method produces improved spatial coverage at higher, though manageable, computational cost.

These results imply improvements in the ocean current maps produced by HF radars in terms of more accurate maps, quantified uncertainty, and improved spatial coverage. Improved observations of near shore dynamics will benefit the many practical applications employing these observations, including plume dispersal studies, oil spill response, and search and rescue.

Contents

Chapter 1

Introduction

Approximately 400 oceanographic HF radars operate globally for the purpose of mapping coastal ocean surface currents. These maps provide scientists, decision makers, planners, and emergency managers hourly maps of currents with kilometer-scale spatial resolution. Ocean current maps have been used to aid oil spill response, water quality monitoring, plume monitoring, marine navigation, and search and rescue operations. These applications often require incorporation of surface currents into forecast models. While these maps provide an unprecedented view of ocean surface currents, several factors combine to limit the the usefulness of the data, both in these applications and in scientific studies of the coastal ocean.

First, a well known source of error in the ocean current maps is the use of idealized receive antenna patterns in the radar measurement. In addition to the surface current velocity, the radars determine the location of the measurement in terms of range and direction. Antenna patterns are important for obtaining direction, and the accuracy of the directional measurement depends on knowing the antenna pattern. Presently, about 50% of the HF radars in the Integrated Ocean Observing System (IOOS) use idealized antenna patterns, even though antenna patterns typically diverge from their

idealized representation. A primary reason for this is the cost and logistical challenge of obtaining the antenna pattern measurement. Chapter 2 presents a method to simplify and automate the calibration of HF radars using radar backscatter from ships along with their positions received through the Automatic Information System (AIS). This method (published in [1]) turns a costly and logistically challenging task into a software product that produces frequent calibrations of the HF radars.

Another factor is the need to provide, along with the surface current observations, estimates of the measurement uncertainties. For example, [5] urges the HF radar community to "develop standard quality control and uncertainty estimates so that search areas can be modeled more effectively". While [6] suggests that "further efforts to understand error structure in HF radar derived data are clearly warranted". Several early papers provided methods for calculating uncertainties [7, 8], but changes in HF radar techniques have made these results obsolete. Chapter 3 identifies a method to estimate uncertainty in the direction to the signal source [4], and combines this with previous results to produce an estimate of the uncertainty in the radial component observations produced by individual HF radars. Simulation techniques are employed to evaluate the uncertainty estimates and inform the application of the estimation technique to observational data. With processing adjustments suggested by the simulation-based analysis, the method is applied to archive data from two operational HF radar sites. Comparisons along the common baseline between the radars suggest that the uncertainty estimates capture a substantial fraction of the error variance.

Finally, Chapter 4 investigates advances in direction finding methods from fields outside of oceanography, in light of the increased computer processing power that is now available. The investigation evaluates the alternative methods using a simulation-based approach that models the backscattered radar signal as a function of ocean currents,

waves and HF noise. The simulations use surface currents from a high resolution numerical model, providing a more complex and realistic test of the direction of arrival methods. Results suggest that alternative processing methods will result in maps of ocean surface currents with improved spatial coverage.

The combined application of the advances presented here will result in more accurate surface current maps, a measure of the data uncertainty, and improved spatial coverage from oceanographic HF radars. These advances will broaden the acceptance of the technique in the larger oceanographic community, and further integrate the HF radar into coastal ocean observing systems. This integration will advance the understanding of the dynamics of the coastal ocean, and enhance the scientific, environmental, and economic applications that utilize that understanding.

Chapter 2

Measuring Antenna Patterns for Ocean Surface Current HF Radars with Ships of Opportunity

2.1 Introduction

Due to their ability to map surface currents with high temporal and spatial resolution, HF radars have become a key component of coastal ocean observing systems. Of the approximately 400 HF radars operating globally, about 140 are funded by the National Oceanic and Atmospheric Administration (NOAA) Integrated Ocean Observing System (IOOS). Typical applications, such as oceanographic research, search and rescue (SAR) operations, and hazardous material spill response, all benefit from accurate HF radar surface current measurements. Additionally, precise, high-resolution antenna patterns are necessary for successful deployment of emerging bi-static and multi-static HF radar systems.

The antenna pattern describes the response of the receive antennas to a signal source

as a function of bearing, allowing the bearing to a given signal to be more accurately determined. Several studies have demonstrated improved comparisons between HF radar and in situ ocean current measurements when using a measured pattern (APM) for bearing determination [9, 10, 11]. Best practices for the operation and maintenance of HF radars prescribe regular measurement of antenna patterns as a necessary component of the quality assurance and quality control (QA/QC) of HF radar data [12]. Therefore, an automated method for determining APMs would assist operators in the QA/QC of HF radar data.

The most common type of HF radar is the SeaSonde (manufactured by CODAR Ocean Sensors, Ltd.), which uses three co-located receive antennas. This type of HF radar determines direction to the signal source via direction finding (DF), as opposed to a phased array of receive antennas, which can use beam forming (e.g. [13]). The SeaSonde receive antennas consist of two orthogonally mounted loop-stick antennas (loops hereafter) along with one vertical monopole antenna [14]. Usually the transmit antenna is separated from the receive antennas by at least one radar wavelength ($\sim$25 m at 13 MHz), though combined receive-transmit antenna systems are now in use. The receive antenna pattern quantifies the directional sensitivity of the loop antennas in terms of the amplitude and phase of a signal source. The standard method for APM involves a small boat carrying a GPS and signal source (e.g. transponder) around a site following a circular arc at a range of a few km [15]. The known direction to the signal source is combined with the received signal to determine the antenna pattern. While current measurements made with phased array radars may be improved after accounting for non-ideal antenna patterns [16], and methods described here could be used to determine the APM for these systems, this study primarily addresses SeaSonde DF systems.

At HF frequencies, several factors can distort antenna patterns compared with undis-

torted patterns, typically referred to as ideal patterns [15]. These factors include flaws in the antennas, and conductive objects in the antenna near field (i.e. within one wavelength) such as vegetation and fences, soil moisture, variable nearby ocean levels. Based on experience with operating 13 SeaSonde HF radars in the vicinity of Santa Barbara, California, and making about 40 antenna pattern measurements, we have found that moderately distorted patterns are typical. [17] defined a parameter to quantify the distortion of APMs. Values of the distortion parameter for the transponder-measured patterns in this study were typically less than the average of the 19 measured patterns used by [17]. Antenna pattern measurements at individual sites made over several years show changes through time, though rates of changes are not well constrained due to infrequent measurement.

Previous studies have used HF signals backscattered from ships of opportunity to calibrate phased arrays [18, 19, 20]. These approaches differed from APM methods described here in that the procedures produced relative phase corrections of the array of receive antennas. The methods described were not developed for DF systems that need the relative magnitudes of the three antennas in addition to the phase. Furthermore, the positions of the backscattering ships of opportunity were unknown.

The approach for measuring antenna patterns described here uses commercial ships of opportunity that transmit their positions using the Automated Identification System (AIS). The AIS system, designed and used primarily for collision avoidance, broadcasts ship identification and position information every 2-10 s while underway. The broadcasts include ship identification (Maritime Mobile Service Identity (MMSI)), latitude, longitude, speed, and heading, and are receivable using low-cost equipment and software. The AIS system operates in the maritime VHF band, with a maximum operational range on the order of 100 km. The AIS supplies critical position data for using ships to derive

antenna patterns.

This study documents a general method for measuring antenna patterns for DF-type HF radars using ships of opportunity broadcasting with AIS. Section 2.2 describes how ship signal is identified in HF radar data and the methods used to estimate antenna patterns from ship backscatter. Section 2.3 shows patterns produced by the method, defines a metric for comparison with transponder-measured patterns, and shows the results of the comparisons. In section 2.4 we discuss the implications of these results, and the conclusions are stated in section 2.5.

2.2 Methods

Data were obtained from four SeaSondes operated by the University of California, Santa Barbara as part of the IOOS surface current mapping network. Three radars used in this study operate near 13 MHz (Table 2.1) and are located along the mainland coastline adjacent to shipping lanes leading to the ports in southern California. The SeaSondes at Refugio State Beach (RFG), Coal Oil Point (COP), and Mandalay Generating Station (MGS, Fig. 2.1) are located near sea level and operate with stock transmit antennas. The fourth SeaSonde on Santa Cruz Island (SCI) is located ∼450 m above sea level and is set back from the ocean by about 2000 m to the north, ∼800 m to the south. It operates with a custom-built dipole transmit antenna that produces more extensive coverage than stock transmit antennas. The receive antenna for each site consists of the standard SeaSonde crossed loops and monopole, separated from the transmit antenna by more than ∼25 m. The HF radars operate with 100 kHz bandwidth, 1.5 km range resolution, and a 2 Hz sweep rate (Table 2.1).

Antenna patterns were measured for each site ($\mathbf{A}_{TRANS}$ hereafter) based on the ship-transponder method described in [15], within the time spanned by the AIS data (Table

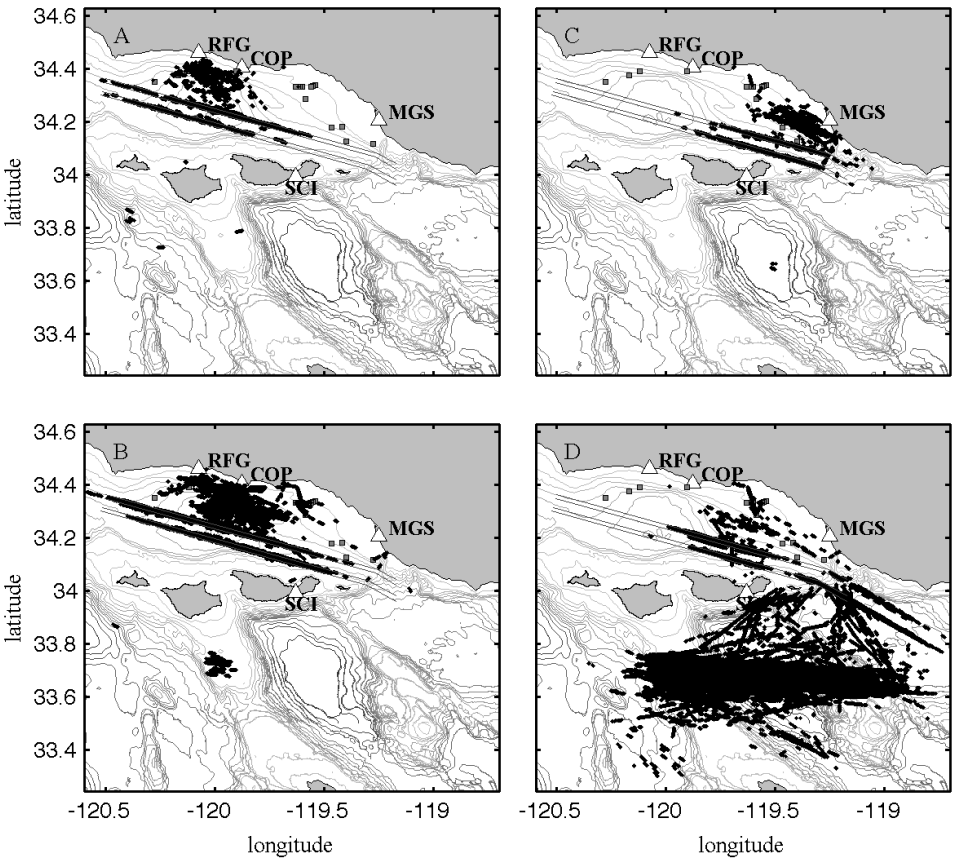

Figure 2.1: Maps of the Santa Barbara Channel and surrounding area. UCSB HF radar sites used in this study are shown (triangles), along with AIS positions from ships (black dots) which resulted in $\mathbf{A}_{SHIP}$ estimates for the HF Radars at a) Refugio State Beach (RFG), b) Coal Oil Point (COP), c) Mandalay Generating Station (MGS), and d) Santa Cruz Island (SCI) site. Lines show the charted shipping lanes, and small gray squares show oil production platforms.

Site	Transmit Frequency (MHz)	Doppler Bin Width (cm s^{-1})	Observation Dates (2010)	$\mathbf{A}_{TRANS}$ Date 2010	Distortion Parameter
RFG	12.149	4.86	1 Jul - 9 Sept	5 Aug	0.21
COP	13.439	4.36	1 Jul - 9 Sept	18 Aug	0.17
MGS	13.554	4.32	7 Jul - 31 Aug	13 Aug	0.20
SCI	13.439	4.36	1 Aug - 29 Sept	9 Sept	0.14

Table 2.1: Site HF transmit signal characteristics, observation dates, and distortion parameter computed using the method of [17]. Of the 19 measured patterns examined by [17], the mean value of the distortion parameter was 0.29 and the standard deviation of values was 0.16.

2.1). $\mathbf{A}_{TRANS}$ then served as ground truth for evaluating antenna patterns derived from backscattering from ships ($\mathbf{A}_{SHIP}$ hereafter). One difference in our determination of $\mathbf{A}_{TRANS}$ compared with the [15] method was the use of a signal source transmitting a constant signal rather than a transponder. This signal source had a longer range than typical transponders and allowed $\mathbf{A}_{TRANS}$ to be determined from ranges of 15 km for SCI and 2.5 km for the other sites.

2.2.1 AIS ship data

AIS antennas, receivers, and dedicated computers record the AIS broadcasts [21] at the SCI and COP sites (at approximately 450 m and 10 m elevation respectively). An Icom IC-PCR1500 radio receives the broadcasts and sends the coded signal to a computer running AIS decoding software [22]. The resulting files contain ship speed, heading, latitude, longitude, time and MMSI. From 1 July 2010 through 29 September 2010 (2184 hours) AIS data from 1536 individual ships were received and used to generate files with range, bearing, and the radial component of the ship velocity relative to each of four radars sites. Range and radial velocity are then used to identify ships moving at a non-zero radial velocity within the operating range of each radar. Figure 2.1 shows

locations of ship observations that provided backscattered signals for estimating $\mathbf{A}_{SHIP}$. GPS errors, radial velocity errors due to ship motions (pitch and roll) and aliasing of these motions contribute to errors in the determined bearing. To put an upper bound on the errors from these sources, the standard deviation of the bearings traversed by the ship during the FFT window (256s time series) is computed (Table 2.2). Errors in bearings determined from AIS are likely much less than the $2-3^o$ standard deviations.

Site	Mean (^{o})	Stdev (^{o})	Max (^{o})	Min (^{o})	Median (^{o})	N
RFG	3.95	3.38	20.2	0.030	2.95	1178
COP	3.32	2.32	37.3	0.005	2.95	4687
MGS	3.19	1.87	20.0	0.015	2.92	1218
SCI	2.28	1.63	20.9	0.004	1.99	8702

Table 2.2: Statistics of bearings traversed by ships during FFT windowing time, as observed by each HF radar site.

2.2.2 HF radar processing

Signal processing parameters for the UCSB SeaSondes are similar to other HF radars operating at these frequencies, which are briefly summarized here. SeaSondes use a frequency modulated continuous wave signal, with interruptions (FMICW), such that each sweep of the entire range (signal transmitted, backscattered and received), is completed at 2 Hz. A matrix of the received complex signals is recorded every 256 seconds for each antenna, with columns corresponding to range, and rows corresponding to each sweep [14]. For SeaSondes these matrices are referred to as range files. FFTs are computed on the columns of this matrix (512 points) and then combined with their complex conjugates to form auto and cross-spectra [8]. Typically, algorithms to remove ship backscatter are applied at this point; thus the cross spectra from individual FFTs (i.e. with no ensemble averaging) are used in the estimation of $\mathbf{A}_{SHIP}$. For SeaSondes the files containing

un-averaged FFTs are referred to as CSQ files. For processing spectra to estimate ocean surface currents, the next steps would be ship signal removal [14], ensemble averaging of the cross spectra, then the application of the Multiple Signal Classification (MUSIC) algorithm [23, 24, 25, 26, 27]. For processing of ship-based patterns, the ship signal identified in spectra by AIS data is extracted and processed as described below.

2.2.3 Detecting ship signals in cross spectra

AIS broadcasts are used to determine where in the range and Doppler frequency space to look for backscattered ship signal. As a ship moves through a radars coverage area, transmitted HF radar waves are backscattered from the ship and are detected by the receive antenna. Under certain combinations of the ships range and motion relative to the HF site, the backscattered signal will have power levels comparable to the Bragg peaks from resonant ocean surface waves. Like the Bragg scattered signal, the position of the ship peak in the cross spectra is determined by the ship radial velocity and corresponding Doppler shift. Figure 2.2 shows example HF radar cross spectra from COP containing the backscattered signal and AIS-determined radial velocities of two ships. The x-axis was converted from frequency to its Doppler velocity equivalent, given by $v = \Delta f {k_0}^{-1}$ (where the radar wave number k_0 is defined as, $k_0 = 2\pi f c^{-1}$, $c = 3.00 \times 10^8$ m s^{-1} is the speed of light, f is the transmit carrier frequency, and Δf is the Doppler shift). The resonant Bragg backscatter peaks (from ocean surface waves) are shown near $\pm$400 cm s^{-1}, the deep water velocity of the ocean surface waves. Figure 2.2A shows a strong signal associated with a ship centered on $\sim$72 cm s^{-1} along with the AIS reported radial velocities of a second ship expected between 520 cm s^{-1} and 750 cm s^{-1}. Successive plots in time (top to bottom) show changes in the range and radial velocities of the ships, and resulting changes in the backscattered signal power as the ships transit relative to COP.

The width of the ship peaks (and Doppler region identified with AIS data) is assumed to result from a combination of changes in the ships radial velocity and any pitching or rolling motions during the 256s time series. Processing described below is applied to each Doppler bin found within the AIS defined area, such that the combination of one ship and one FFT can yield several estimates of $\mathbf{A}_{SHIP}$ at adjacent bearings, along with different signal-to-noise ratios (SNRs).

2.2.4 Relationship between backscattered signal and antenna patterns

The relationship between the signal observations, as found in the HF radar cross spectra, to the antenna pattern, is given by [27]. [27] models received signal voltages as a linear combination of the incident signals, antenna response, and noise. In the general case, the received complex voltages X_i on antenna i (with $i = 1, 2, M$, where $M = 3$ for SeaSondes) from d incident signals given by F_j ($j = 1, 2, ...d$), plus the assumed uncorrelated noise W_i, is expressed,

$$\begin{bmatrix} X_1 \\ X_2 \\ X_3 \end{bmatrix} = \begin{bmatrix} a_1(\theta_1) & a_1(\theta_2) & \cdots & a_1(\theta_d) \\ a_2(\theta_1) & a_2(\theta_2) & \cdots & a_2(\theta_d) \\ a_3(\theta_1) & a_3(\theta_2) & \cdots & a_3(\theta_d) \end{bmatrix} \begin{bmatrix} F_1 \\ F_2 \\ \vdots \\ F_d \end{bmatrix} + \begin{bmatrix} W_1 \\ W_2 \\ W_3 \end{bmatrix}, \tag{2.1}$$

where $a_i(\theta_j)$ is the complex response of antenna i to signal F_j arriving from direction θ_j. The column vector of complex numbers $\left[a_1(\theta_j)\ a_2(\theta_j)\ a_3(\theta_j)\right]^T$ is the antenna pattern at θ_j. Writing the matrix of $a_i(\theta_j)$ as $\mathbf{A}$, Eqn. (2.1) becomes,

$$\mathbf{X} = \mathbf{AF} + \mathbf{W}, \tag{2.2}$$

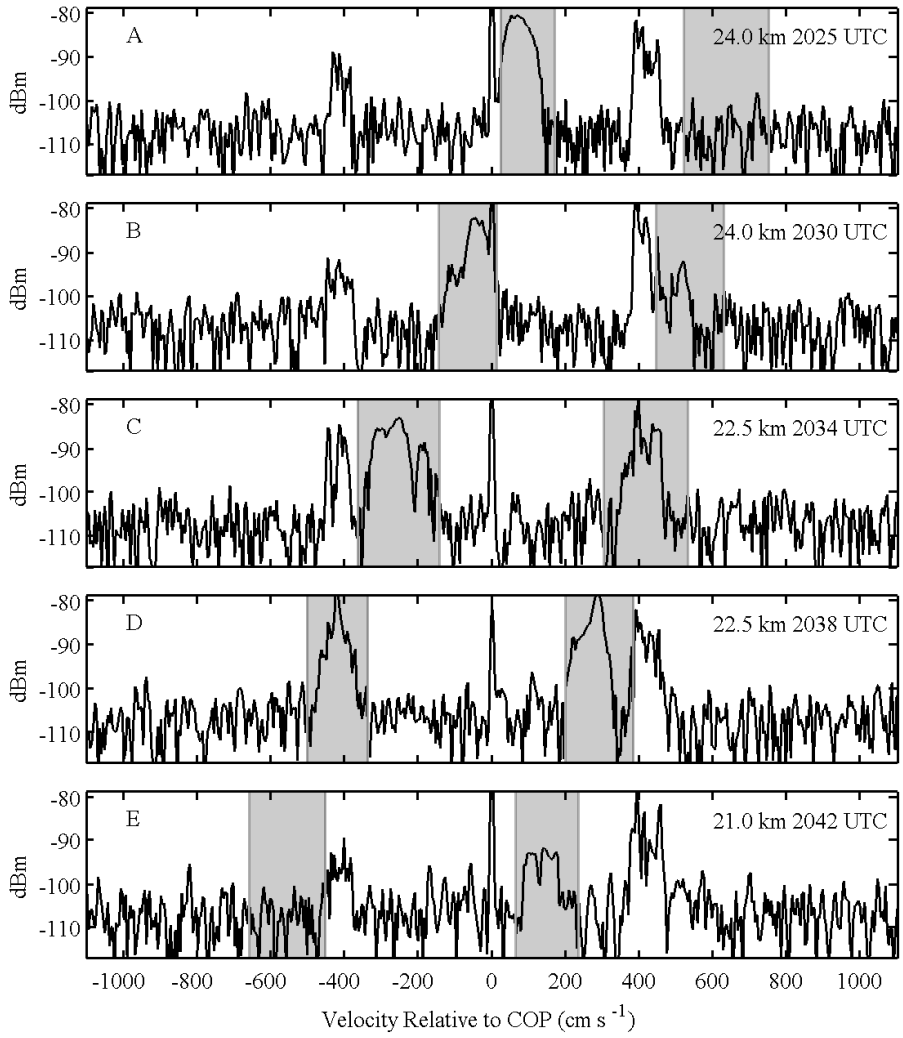

Figure 2.2: Five sequential HF radar cross spectra from COP on 6 December 2008. For each plot, the vertical axis shows signal power (dBm), and the horizontal axis shows radial velocity (derived from Doppler shifted frequency). Range cell distance and time indicated in upper right. Signal above $\sim$ 100 dBm scattered from ocean surface waves (containing ocean current information) can be seen near $\pm$400 cm s^{-1}. Gray shaded areas show ranges of radial velocities of two ships from AIS data, showing the change in radial velocity with time. The ships are the 280 meter Cosco Hongkong, and 213 meter Wan Hai 313. The increase and decrease of backscattered signal levels from the ships can be seen as the ships move through the Santa Barbara Channel.

(Note that $\mathbf{A}$ represents the matrix of antenna responses from d incident signals (Eqn. (2.1) and Eqn. (2.2)), while $\mathbf{A}_{TRANS}$ defined previously represents the antenna pattern at all θ_j). The covariance matrix $\mathbf{S}$ is then obtained from $\mathbf{X}$,

$$\mathbf{S} \equiv \overline{\mathbf{X}\mathbf{X}^H} = \mathbf{A}\overline{\mathbf{F}\mathbf{F}^H}\mathbf{A}^H + \overline{\mathbf{W}\mathbf{W}^H}, \tag{2.3}$$

Where ^{H} denotes complex conjugate transpose. Assuming the noise variance σ^2 is equal on each antenna, and defining $\mathbf{P} = \overline{\mathbf{F}\mathbf{F}^H}$ we obtain Eq. (4) of [27],

$$\mathbf{S} \equiv \overline{\mathbf{X}\mathbf{X}^H} = \mathbf{A}\mathbf{P}\mathbf{A}^H + \sigma^2\mathbf{I}, \tag{2.4}$$

where $\mathbf{I}$ is the identity matrix. Eqn. 2.4 expresses the cross spectra signal power (observed at a given Doppler frequency) as a function of the incident signals, noise, and the antenna pattern.

In the special case of a single signal source with a known location, such as backscatter from a ship broadcasting AIS data, Eqn.2.4 can be used to determine the antenna pattern at the bearing of the ship. In this case, $d = 1$, and the matrix $\mathbf{A}$ becomes a column vector $\left[a_1(\theta_j)\ a_2(\theta_j)\ a_3(\theta_j)\right]^T$, with θ_j given by the bearing to the ship. With $d = 1$, P is a scalar, the rank of the matrix $\mathbf{A}P\mathbf{A}^H$ is one, and Eqn. 2.4 becomes:

$$\mathbf{S} = P\mathbf{A}\mathbf{A}^H + \sigma^2\mathbf{I}, \tag{2.5}$$

Since P is now a scalar and σ^2 adds to the diagonals, $\mathbf{A}\mathbf{A}^H$ and $\mathbf{S}$ share the same eigenvectors. The 3×3 matrix $\mathbf{A}\mathbf{A}^H$ has one non-zero eigenvalue and the corresponding eigenvector is a scalar multiple of $\mathbf{A}$, the antenna pattern vector at θ_j. These properties result from matrices of the form $\mathbf{A}\mathbf{A}^H$ when $\mathbf{A}$ is a vector ([28], p 98). In other words,

the vector $\mathbf{A}$ becomes the single basis vector for the matrix $\mathbf{A}\mathbf{A}^H$. The practical result is that for a known single source, the signal data in the cross spectra files represented by $\mathbf{S}$, are a scalar multiple of the antenna pattern, $\mathbf{A} = \left[a_1(\theta_j)\ a_2(\theta_j)\ a_3(\theta_j)\right]^T$ at θ_j. Thus, the antenna pattern A at θ_j can be derived directly from the elements of the rank 1 matrix $\mathbf{S}$. To recover the antenna pattern, we choose the third column of the matrix $\mathbf{S}$ given by s_{j3}, and normalize by s_{33},

$$\mathbf{A} = \left[\frac{s_{13}}{\Re(s_{33})}\ \frac{s_{23}}{\Re(s_{33})}\ 1\right]^T. \tag{2.6}$$

Note that for SeaSondes, the imaginary part of s_{33} is zero because the phase ϕ is defined as zero on antenna 3 (the monopole) (where the real and imaginary components are related to the magnitude (r) and phase ϕ by Eulers formula, $re^{i\phi} = r\cos(\phi) + ir\sin(\phi)$). Eqn. 2.6 shows the antenna pattern $\mathbf{A}$ at bearing θ_j in terms of the signals observed in the SeaSonde cross-spectra.

2.2.5 Assigning bearing

The final step to complete the determination of $\mathbf{A}_{SHIP}$ is to associate observations of the antenna pattern in $\mathbf{A}(\theta_j)$ to the ship bearing θ_j. From the AIS latitude and longitude, reported at approximately 10-s intervals, the range to the HF radar site is computed, and from this the time-centered radial velocities and corresponding bearing to the HF radar are computed, producing a time series of ship radial velocity and bearing. These observations form a table during the time of the 256 s FFT (with columns radial velocity and bearing, each row at a new time). The FFT separates the received signals into Doppler frequency bins and their equivalent Doppler radial velocities. The radial velocity of each signal bin is matched with the AIS-determined ship radial velocity, associating a bearing to the ship with each signal bin through a table look-up. The collection of

column vectors $\mathbf{A}(\theta_j)$ at all observed values of θ_j $(j = 1, 2, ...b)$ is the matrix $\mathbf{A}$,

$$\mathbf{A}_{SHIP} = \big[\mathbf{A}(\theta_2)\ \mathbf{A}(\theta_2)\ \ldots \mathbf{A}(\theta_d)\big]. \tag{2.7}$$

For SeaSondes, $\mathbf{A}_{SHIP}$ is a matrix with three rows, with the third row consisting of all ones, as can be seen from Eqn. (2.6).

2.2.6 Comparison Metric

At each bearing, we quantify the difference between the complex quantities $\mathbf{A}_{SHIP}$ and $\mathbf{A}_{TRANS}$ using the Euclidean distance D between the two at the same bearing. Before computing D, $\mathbf{A}_{SHIP}$ and $\mathbf{A}_{TRANS}$ are put into an equivalent form consisting of only real numbers. Beginning with Eqn. (2.7), the third row is dropped, and $\mathbf{A}_{SHIP}$ is rewritten in terms of the real and imaginary components, for example,

$$\mathbf{A}_{SHIP} = \Big[\Re(a_1(\theta))\ \Im(a_1(\theta))\ \Re(a_2(\theta))\ \Im(a_2(\theta))\Big]^T. \tag{2.8}$$

Simplifying the notation, the subscripts R and I designate real and imaginary components:

$$\mathbf{A}_{SHIP} = \big[a_{1R}\ a_{1I}\ a_{2R}\ a_{2I}\big]^T. \tag{2.9}$$

At a given θ, Eqn. (2.9) gives the four components of $\mathbf{A}_{SHIP}$ as a vector of real numbers. For two estimates of the antenna pattern at a given bearing (e.g. $\mathbf{A}_{SHIP}(\theta)$ and $\mathbf{A}_{TRANS}(\theta)$), the Euclidean distance D is defined,

$$D(\theta) = ([\mathbf{A}_{SHIP}(\theta) - \mathbf{A}_{TRANS}(\theta)]^T[\mathbf{A}_{SHIP}(\theta) - \mathbf{A}_{TRANS}(\theta)])^{\frac{1}{2}}, \tag{2.10}$$

where D is the distance between two points in a four dimensional space. D quantifies the difference between the two patterns at given bearing, producing a scalar measure of their similarity. Note that the MUSIC algorithm uses the inverse of D^2 in the direction of arrival calculation [27], and that D is dimensionless since both $\mathbf{A}_{SHIP}$ and $\mathbf{A}_{TRANS}$ have been normalized.

2.2.7 Signal-to-noise ratios for thresholding

Four SNRs are defined for thresholding, to separate ship backscatter from other signal sources. Other signal sources include first and second order backscatter from the ocean surface, broadband and narrowband noise from other HF radar transmitters, and natural external sources such as worldwide thunderstorms. These signals typically persist in time, or are broadband, often spread over many Doppler bins and several range cells. When measuring antenna patterns with transponders, the signal is typically characterized by a narrow peak in frequency and range, with power levels well above the noise. Away from the peak, the signal level falls rapidly into background noise in adjacent bins and adjacent range cells. The typical characteristics of transponder signals are also desirable when measuring antenna patterns with ship backscatter. Ship backscatter signals are also transient, typically present in a given Doppler bin for only a single FFT. The SNRs described below are designed to exploit the differences in signal characteristics, enabling reliable separation of ship backscatter from other signal sources.

Each SNRs is produced according to the equation,

$$SNR = S_{SIGNAL} - \langle S_{NOISE} \rangle, \tag{2.11}$$

where S_{SIGNAL} is the power observed (dBm) in the monopole auto spectra, in the range cell and Doppler bin assumed to contain ship backscatter. $\langle S_{NOISE} \rangle$ is the average of

bins assumed to contain only noise, as explained below. The four SNRs are determined by varying spectral bins used to compute S_{NOISE}.

Site	SNR_{BKGND}	SNR_{LOCAL}	SNR_{RANGE}	SNR_{TIME}
RFG	6.1	10.3	59.4	24.2
COP	6.0	20.6	28.5	44.9
MGS	8.4	22.8	27.7	41.1
SCI	3.3	20.6	29.2	46.9

Table 2.3: Percent of points rejected due to each SNR criterion, for each HF radar site.

The first SNR, denoted SNR_{BKGND}, is computed from Eqn. (2.11) with $\langle S_{NOISE} \rangle$ defined as the average power over two frequency ranges, Δf_{BKGND} = 0.701 to 0.960 Hz, and -0.701 to -0.960 Hz, (Fig. 2.3a). SeaSonde software typically uses noise levels in the region defined by Δf_{BKGND} to compute SNR of the first order Bragg scatter peaks. Following the SeaSonde method, an initial $\langle S_{NOISE} \rangle$ is obtained, then spectral points more than three standard deviations from the mean are removed and $\langle S_{NOISE} \rangle$ is recomputed on the remaining points.

The second SNR, SNR_{LOCAL}, is computed using Eqn. (2.11) after computing as the mean spectral power spanning a range of Doppler frequency bins (Δf_{LOCAL}) adjacent to the ship peak. Here $\langle S_{NOISE} \rangle$ is the average of 20 Doppler bins found on either side of the spectral region identified by AIS (Fig. 2.3a). Bragg signals are excluded from this calculation, such that the resulting $\langle S_{NOISE} \rangle$ may depend on fewer than the 40 Doppler bins.

The third SNR, SNR_{RANGE}, is computed using Eqn. (2.11) with $\langle S_{NOISE} \rangle$ determined from multiple range cells. Unlike SNR_{BKGND} and SNR_{LOCAL}, which are computed from single range cells, SNR_{RANGE} is computed using $\langle S_{NOISE} \rangle$ based on spectra power found in the same Doppler bin (f_{SHIP}), but in several range cells spanning two intervals (Δr). The Δr intervals each span six range cells, beginning two range cells

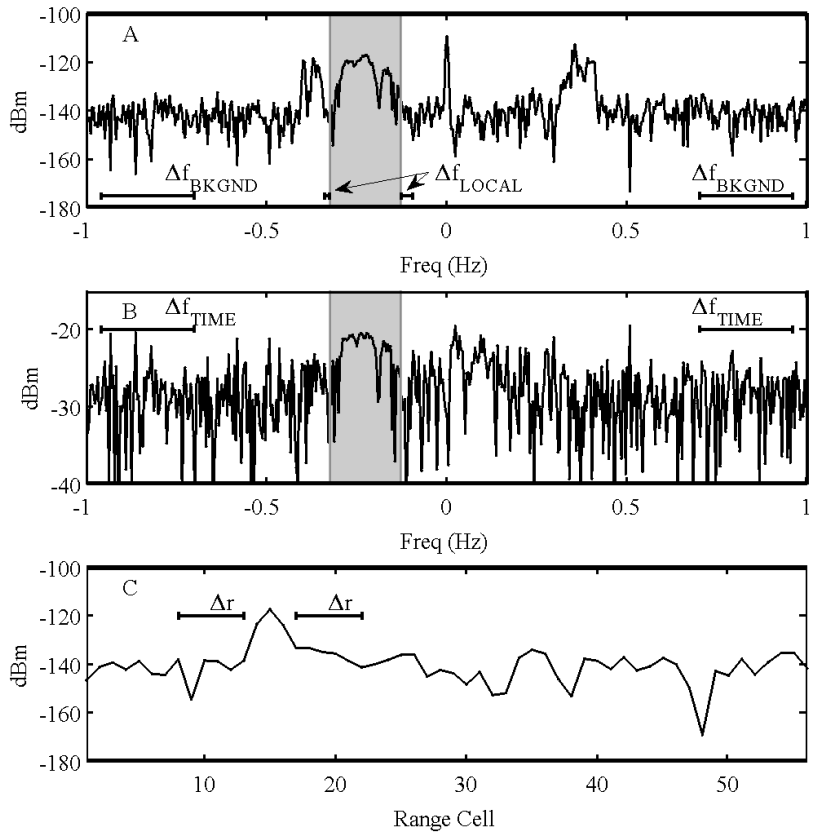

Figure 2.3: a) HF radar cross spectra as a function of frequency (from Fig.2.3c) along with the ship radial velocity from AIS (gray shaded area), for range cell 15. Horizontal bars near the bottom of the figure show range of frequency (Δf) over which average noise levels are computed for SNR_{BKGND} and SNR_{LOCAL}. b) Cross spectra signal after removing hourly mean, along with range of frequency (Δf_{TIME}) over which average noise levels are computed for SNR_{TIME}. c) Cross spectra plotted as a function of range cell index, for the frequency bin centered at -0.227 Hz. Horizontal bars show the range cells (Δr) used to compute the average noise level for SNR_{RANGE}, spanning range cells 8-13 and 17-22.

away from S_{SIGNAL}. For example, if the ship S_{SIGNAL} is located in range cell 15 and Doppler bin f_{SHIP}, then $\langle S_{NOISE} \rangle$ is computed from signals found at f_{SHIP} in the Δr intervals extending between range cells 8-13 and 17-22, as shown in Fig. 2.3c. The Δr intervals begin two range cells away from S_{SIGNAL}, because ship backscatter signal may be present in adjacent range cells due to pulse stretching in the receiver [8].

The fourth SNR, SNR_{TIME}, uses the time domain properties of both S_{SIGNAL} and $\langle S_{NOISE} \rangle$ to separate short term signal sources, such as ships, from persistent signal sources, such as currents and waves. Prior to the Eqn. (2.11) calculation, the time-centered, hourly averaged cross spectrum is subtracted from the individual cross spectra containing S_{SIGNAL}. As shown in Fig. 2.3b, this removes much of the first and second order Bragg signal, along with any other signals persisting on hourly or longer time scales. SNR_{TIME} is then computed with Eqn. (2.11) using S_{SIGNAL} from the residual, and $\langle S_{NOISE} \rangle$ over Doppler regions defined by Δf_{BKGND} as in SNR_{BKGND}. Calculation of SNR_{TIME} is similar to real time HF radar processing methods, which apply an Infinite Impulse Response (IIR) filter to remove ship backscatter [14].

The above methods produce four SNRs for each signal observation that may contain ship backscatter. Low SNR from any of the four methods suggests the presence of contaminating interference or other non-ship signal. When applying thresholds to the SNRs, the lowest value of SNR of the four prevents the $\mathbf{A}_{SHIP}$ point from passing a given SNR threshold. Thus the minimum of the four methods is found:

$$SNR_{MIN} = min(SNR_{BKGND}, SNR_{LOCAL}, SNR_{RANGE}, SNR_{TIME}), \tag{2.12}$$

such that each $\mathbf{A}_{SHIP}$ observation is associated with one SNR value for use in thresholding. The fraction of points rejected due to a given SNR method is shown in Table 2.3. Comparisons below show results of $\mathbf{A}_{SHIP}$ after requiring $SNR_{MIN} > 11$ dB. Justifica-

tion for this threshold is described later.

2.2.8 AIS based thresholds

Three additional metrics are computed from the AIS data for thresholding. Threshold values were determined empirically, as discussed below. The first is the standard deviation of the ship radial velocity observed during the 256-s cross spectra interval (σ_{SHIP}). $\mathbf{A}_{SHIP}$ observations obtained from ships when $\sigma_{SHIP} > 150$ cm s^{-1}were excluded from the analysis. The second metric is the distance between ships and oil platforms (Δd_p). $\mathbf{A}_{SHIP}$ exhibits large errors when ships are close to these structures, so ships with $\Delta d_p <$ 1500 m were excluded. The third metric Δd_s is defined as the minimum separation in range and Doppler bins between ships. This metric identifies ships that are in nearly the same range cell and traveling at nearly the same radial velocity relative to a site. Ships separated by $\Delta d_s < \pm 1$ range cell and $< \pm 20$ Doppler bins were excluded.

2.3 Results

2.3.1 Observations

Estimates of $\mathbf{A}_{SHIP}$ and $\mathbf{A}_{TRANS}$ show reasonable agreement for RFG, COP, MGS, and SCI as shown in Figures 2.4, 2.5, 2.6, and 2.7, respectively. At RFG, some bearings exhibit differences, but the overall shape of $\mathbf{A}_{TRANS}$ is reproduced by the 5^o bin averages of $\mathbf{A}_{SHIP}$, including small scale structure near $165^o - 170^o$ (Fig. 2.4 a,b). (Bins with $N <$ 5 not shown). A significant difference in the angular coverage is observed, as $\mathbf{A}_{TRANS}$ extends from 90^o to 275^o, while the $\mathbf{A}_{SHIP}$ covers 120^o to 250^o (Fig. 2.4a). The difference in angular coverage results from the orientation of the shipping lanes relative to the site (Fig. 2.1a), such that ships at bearings near the edges of $\mathbf{A}_{TRANS}$ are at greater range

and the backscattered signal levels are low. Figure 2.8 shows histograms of $\mathbf{A}_{SHIP}$ data points versus bearing for each site, illustrating the effect of range on the number of available data points at RFG (Figure 2.8a). Figures 2.8a and 2.8b also show low values in histogram bins where most ships pass through the zero Doppler bin, near 195^o for RFG and COP. Background signal levels are consistently high near zero Doppler due to backscatter from stationary objects, for example from land [29], making SNR of the ship backscatter signal relatively low in this region of the Doppler spectrum.

COP has a similar orientation to the shipping lanes as RFG, but results shown in Fig. 2.5 have some important differences from RFG. $\mathbf{A}_{SHIP}$ at COP was produced from about five times more observations than at RFG (15691 data points at COP vs. 3043 at RFG, Fig. 2.8 a,b), though these came from only 40% more ships (246 at COP vs. 174 at RFG). COP typically has higher levels of transmitted power than RFG (data not shown), and RFG also experiences elevated levels of diurnal background noise [30]. Lower signal and higher noise levels significantly reduce the number of ships producing antenna pattern estimates at RFG. Differences between Figs. 2.4 and 2.5 demonstrate the broader angular coverage obtained at COP, with observations spanning 200^o, vs. approximately 130^o for RFG. The maps (Fig. 2.1 a,b), and the ship observations vs. bearing (Fig. 2.8 a,b) also illustrate this difference. Disagreement between $\mathbf{A}_{SHIP}$ and $\mathbf{A}_{TRANS}$ observed at COP for bearings $< 140^o$ coincides with the presence of a building and several trees in the near field of the receive antenna at these bearings. Bearings less than 120^o coincide with the presence of a cluster of oil production platforms, suggesting that multipath scatter from these objects may be important even with $\Delta d_p > 1500$ m. Disagreement is also observed between $\mathbf{A}_{SHIP}$ and $\mathbf{A}_{TRANS}$ for bearings $< 200^o$ in the a_{2I} component (Fig. 2.5 d).

Results for MGS Loop 1 $\mathbf{A}_{SHIP}$ agree with $\mathbf{A}_{TRANS}$ between 190^o and 290^o (Fig.

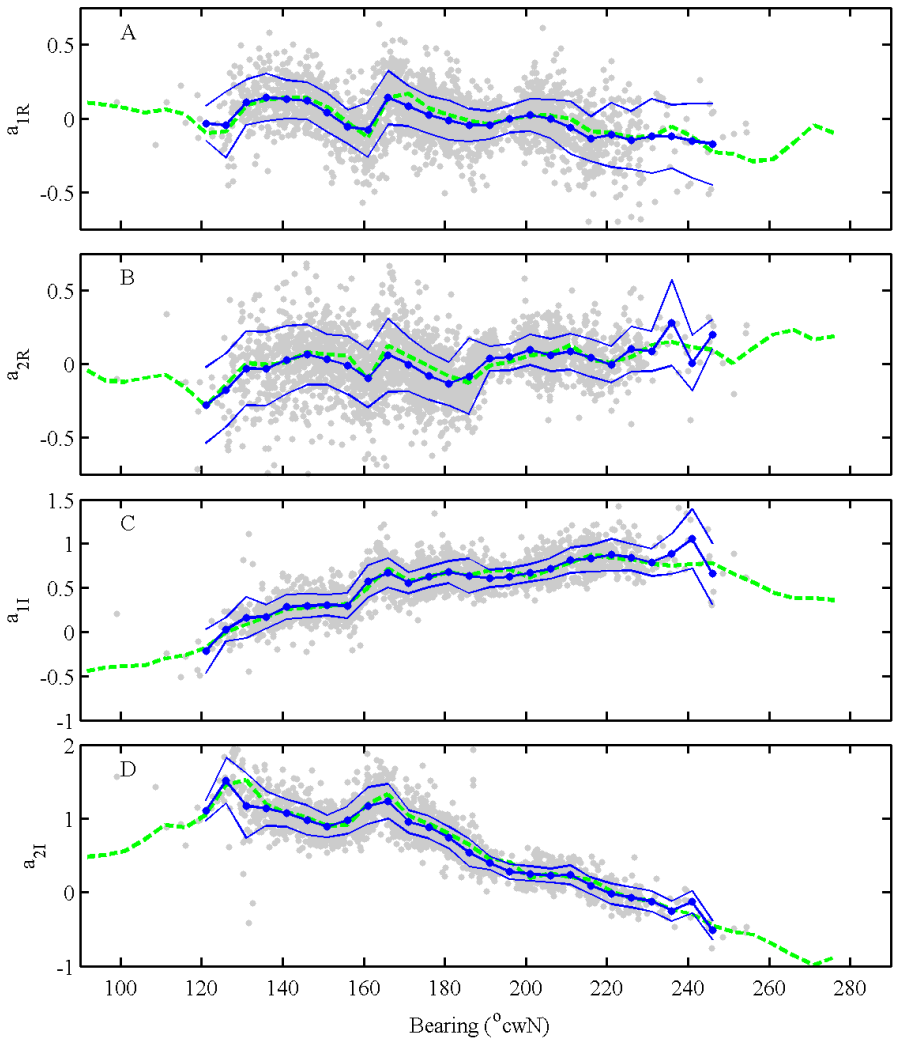

Figure 2.4: RFG $\mathbf{A}_{TRANS}$ (green dashed line) and individual $\mathbf{A}_{SHIP}$ (gray dots) with 5^o bin averages (large blue dots) $\pm$bin standard deviations (blue lines), a) Loop 1 real, b) Loop 2 real, c) Loop1 imaginary, d) Loop 2 imaginary). Note that in each plot the vertical axes were adjusted to best show the data.

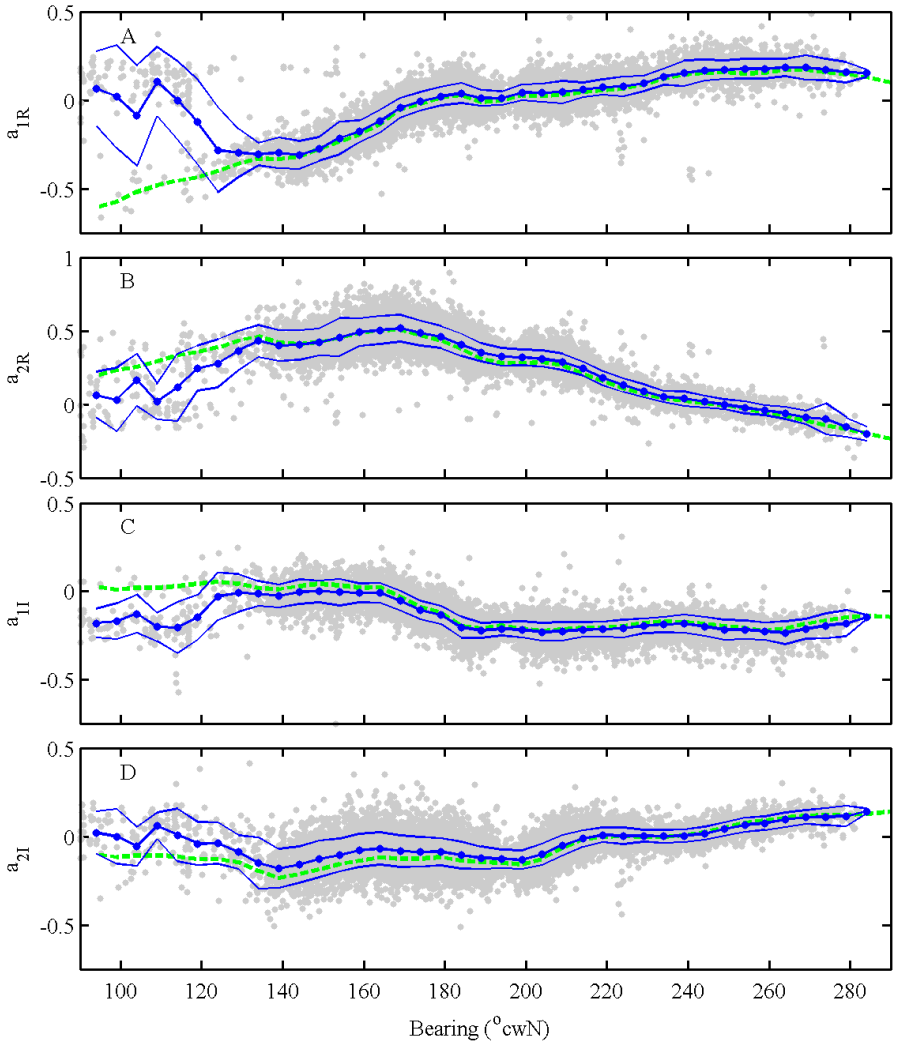

Figure 2.5: As in Fig. 2.4, for COP.

2.6), while the methods diverge for bearings less than 190^o. Due to the orientation of the shipping lanes relative to the site (Fig. 2.1c), few ship observations are obtained north of 280^o, while the transponder pattern continues to 330^o. However, several $\mathbf{A}_{SHIP}$ observations were obtained at bearings east of $\sim 170^o$ where $\mathbf{A}_{TRANS}$ ends, despite the long distances that the HF radar waves must travel over land.

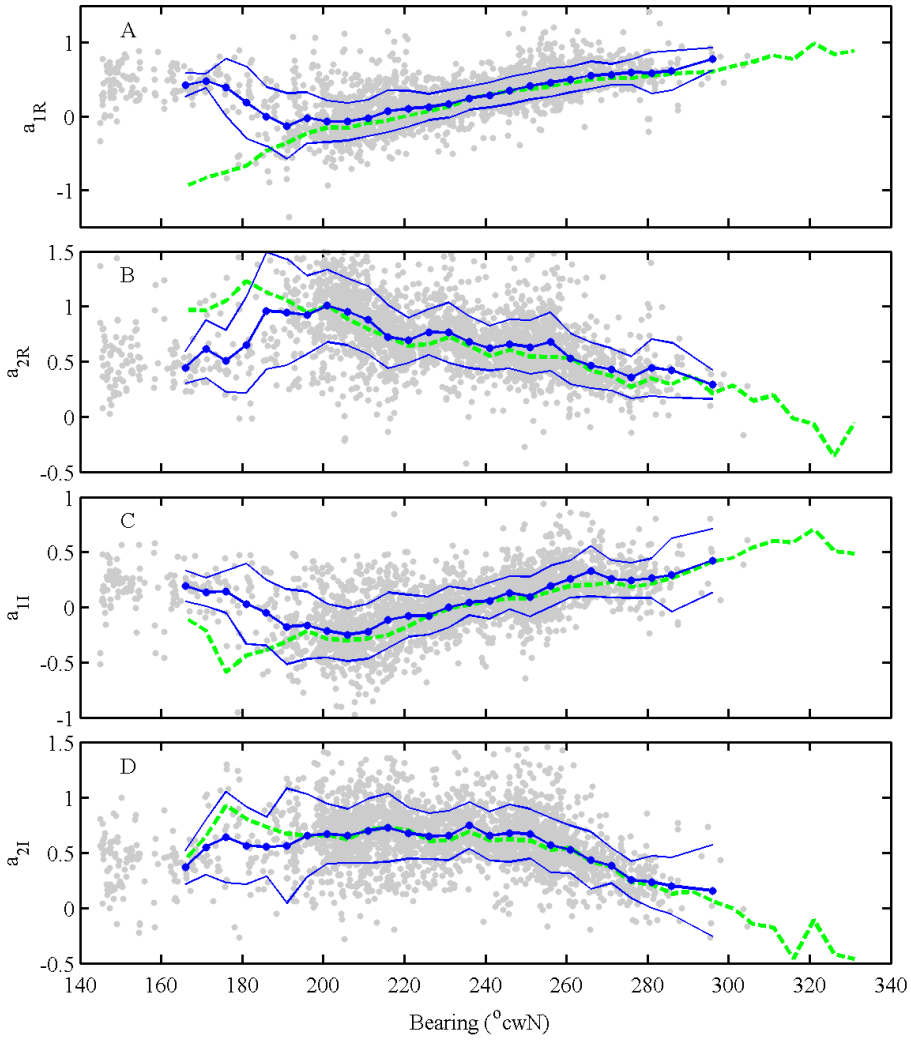

Figure 2.6: As in Fig. 2.4, for MGS.

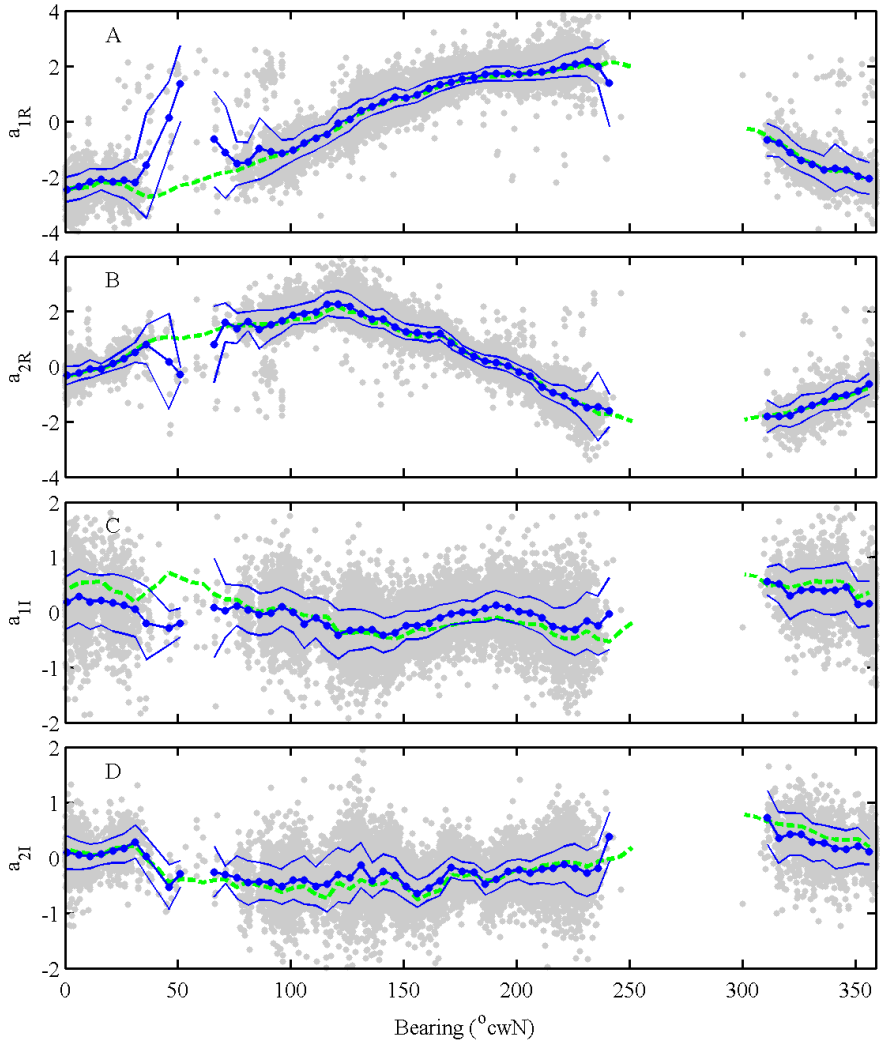

Figure 2.7: As in Fig. 2.4, for SCI.

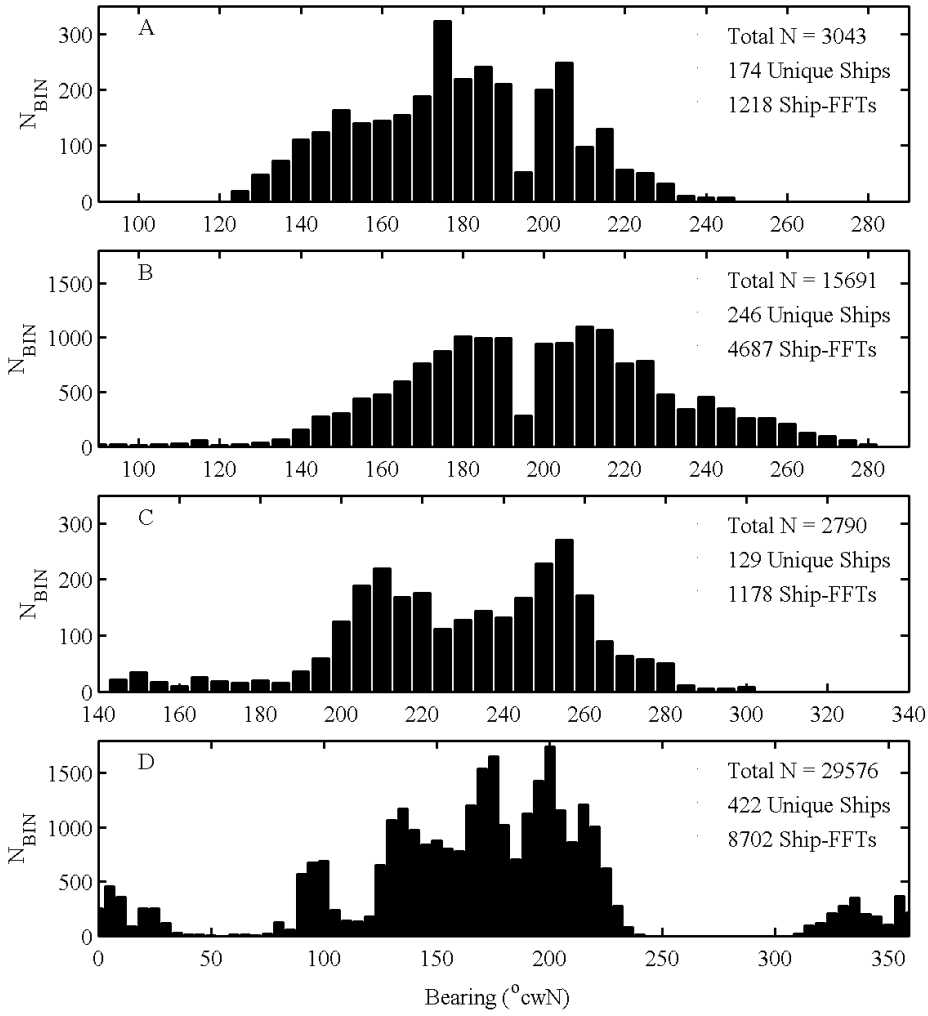

Figure 2.8: The number of $\mathbf{A}_{SHIP}$ data points per 5^o bin as a function of bearing for a) RFG, b) COP, c) MGS and d) SCI. Both horizontal and vertical axes adjusted to best show the data.

$\mathbf{A}_{TRANS}$ from SCI spans approximately 280^o in bearing (Fig. 2.7) with coverage both north and south of the Santa Cruz Island. Agreement between $\mathbf{A}_{SHIP}$ and $\mathbf{A}_{TRANS}$ is observed, except between $\sim 30^o$ to $\sim 80^o$, where HF radar waves travel long distances over land. The 5^o bin averages of $\mathbf{A}_{SHIP}$ reproduce small scale structure in $\mathbf{A}_{TRANS}$, such as Fig. 2.7d between 150^o to 200^o. A comparable number of observations were obtained within the Santa Barbara Channel as were obtained at RFG, though a longer time period was covered with the SCI data (Table 2.1). Backscatter from 422 unique ships produced 29,576 $\mathbf{A}_{SHIP}$ observations (Fig. 2.8d) during the two months spanned by the SCI data. Fig. 2.8d shows that most observations originated from south of the island, between 120^o and 240^o (Fig. 2.1d). Fig. 2.8 also shows the number of individual ship-FFT combinations, to provide a lower bound on the number of independent observations.

2.3.2 Comparison metric (D) example and results

Prior to comparing $\mathbf{A}_{TRANS}$ and $\mathbf{A}_{SHIP}$ using D, a simple case is presented to build intuition and guide interpretation of the results. The range of nominal values of D is illustrated by comparing D between two COP $\mathbf{A}_{TRANS}$ measurements from May 2006 and August 2010 (amplitudes Fig. 2.9a, and phases Fig. 2.9b). Minor differences in the amplitudes and phases, due to minor changes in the site hardware and receive antenna near field environment, result in D ranging from 0.1 to 0.4 (Fig. 2.9c). Figure 2.9c indicates the range of D that can be expected between two antenna patterns that are qualitatively similar.

Figure 2.10 shows D between the 5^o bin averages of $\mathbf{A}_{SHIP}$ and $\mathbf{A}_{TRANS}$ for each HF radar site, summarizing the comparisons shown in Figs. 2.4-2.7. Figure 2.10a illustrates the similarity between $\mathbf{A}_{SHIP}$ and $\mathbf{A}_{TRANS}$ at RFG, with the exception of 130^o and near 240^o, where D captures the differences observable in Fig. 2.4d (at 130^o), and Figs. 2.4b-d

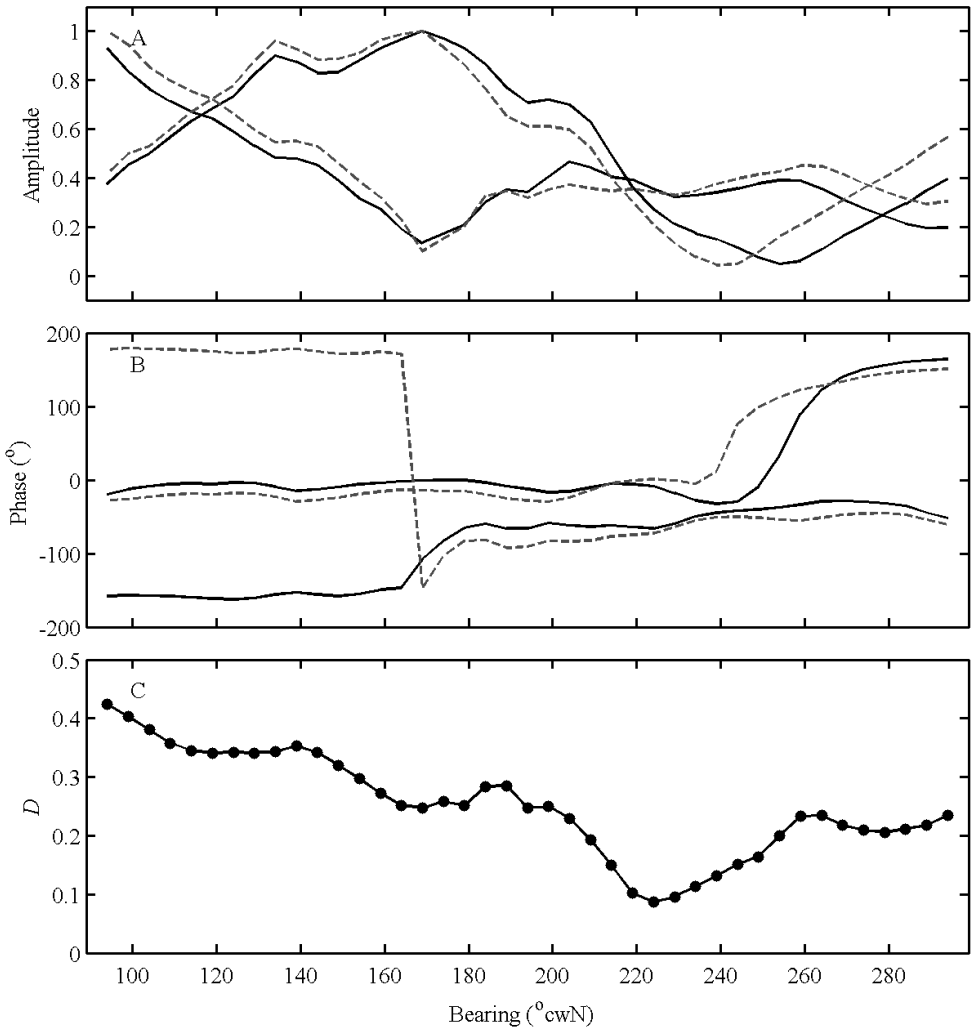

Figure 2.9: $\mathbf{A}_{TRANS}$ for COP measured 22 May 2006 (black solid lines) and 18 August 2010 (gray dashed lines) in terms of the amplitudes (a) and phases (b). c) D as a function of bearing between the COP 22 May 2006 and 18 August 2010 $\mathbf{A}_{TRANS}$.

(near 240^o). For COP, differences between $\mathbf{A}_{SHIP}$ and $\mathbf{A}_{TRANS}$ at bearings less than 135^o observable in Fig. 2.5 are shown by D in Fig. 2.10b, along with the close agreement observed at other bearings with $D < 0.1$. Fig. 2.10c shows agreement for MGS between 200^o and 295^o. Comparing Fig. 2.10c with Fig. 2.8c suggests that high D at MGS (outside 200^o - 295^o) may relate to the low N observed there. Minimum values of D for SCI (Fig. 2.10d) lie near $D = 0.15$, with larger values of D, e.g. near 120^o, corresponding to differences observed in Figs. 2.7 c, d. Overall, Fig. 2.10 shows that the lowest values of D, and thus the lowest errors, are observed at COP (Fig.2.10b).

2.3.3 D vs. SNR_{MIN}

Values and scatter of D decrease rapidly with increasing SNR_{MIN} at all four sites (Fig. 2.11). For SNR greater than 10 dB, the broad scatter in D narrows, such that $SNR_{MIN} >\sim$15 dB is associated with low D. SCI is an exception with some points with $SNR_{MIN} > 10$ and $D \sim 1.25$. Values of D averaged over bins of width $\Delta SNR = 1$ dB are also shown (open circles), along with the number N of points per bin (right-hand y-axis) showing that each site has more than 1000 observations with $SNR_{MIN} >$10 and more than 100 observations with $SNR_{MIN} >$15.

2.4 Discussion

A goal of this research is to evaluate the method as the sole source of antenna pattern measurements. In estimating $\mathbf{A}_{SHIP}$ (Figs. 2.4-2.7), significant agreement between $\mathbf{A}_{SHIP}$ and $\mathbf{A}_{TRANS}$ was found (e.g. Fig. 2.10, with $D <$0.2) when the following empirical thresholds were used:

$SNR_{MIN} > 11$ dB,

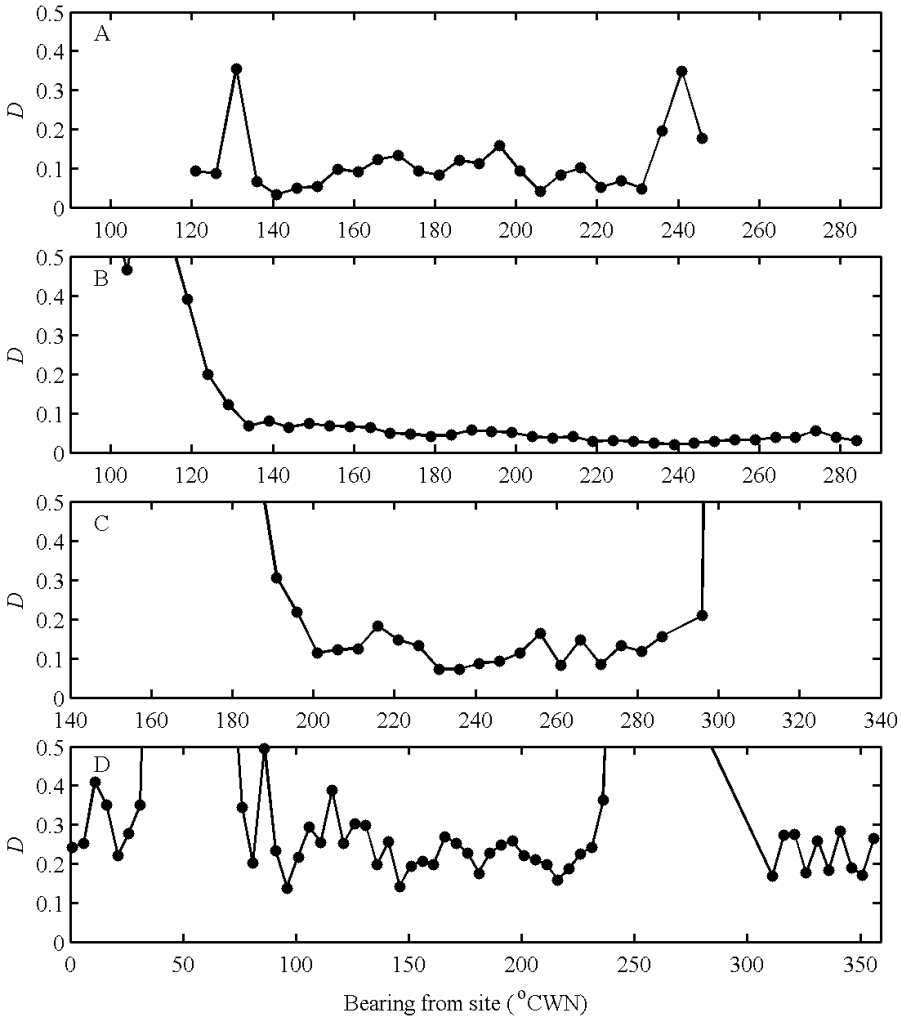

Figure 2.10: D as a function of bearing between $\mathbf{A}_{SHIP}$ and $\mathbf{A}_{TRANS}$ for each of the four HF radar sites a) RFG, b) COP, c) MGS and d) SCI.

$\sigma_{SHIP} < 150$ cm s^{-1},

$\Delta d_p > 1500$ m,

$\Delta d_s > \pm 1$ range cell and $> \pm 20$ Doppler bins.

Figure 2.11 guided the choice of the SNR_{MIN} threshold, which produces low overall error as measured by D. Limiting the standard deviation of radial velocity (σ_{SHIP}) identifies ships with smaller changes in radial velocity during the 256-s integration times of the cross spectra. Both Δd_p and Δd_s thresholds removed multi-source signals, which produced errors in $\mathbf{A}_{SHIP}$. Since each threshold is applied to metrics computed only from the AIS and HF radar data, we suggest the method can serve as an independent source of APMs. While this analysis produced APMs at 5^o resolution (Figs. 2.4-2.7), with sufficient data density, 1^o bins with output every 1^o are possible.

These results corroborate a theoretical and experimental analysis of ship tracking with HF radars [31]. Using a SeaSonde with measured antenna patterns, the study found a power law relationship between SNR and the uncertainty in bearing to a target, such that uncertainty decreased with increasing SNR. The analysis indicates that uncertainty in the FFT signal power, due to contributions from noise, leads to uncertainty in the MUSIC determined bearing. Our results similarly show decreased error with increasing SNR (Fig. 2.11). The results differ in that the errors here are between two antenna patterns ($\mathbf{A}_{SHIP}$ and $\mathbf{A}_{TRANS}$ as quantified by D) at a known signal bearing, while the [31] results determine the uncertainty in the signal bearing. [31] also suggests that contributions from noise (quantified by SNR) explain most of the scatter in $\mathbf{A}_{SHIP}$ observed in Figs. 2.4-2.7. Both analyses suggest rejecting data with SNR below 7-10 dB. These combined results demonstrate that SNR is the most important metric for accurate APM determination.

Scatter in $\mathbf{A}_{SHIP}$ (Figs. 2.4-2.7) resulting from errors in the AIS and the GPS positions they report are probably small. Methods used to assign bearings to $\mathbf{A}_{SHIP}$ described

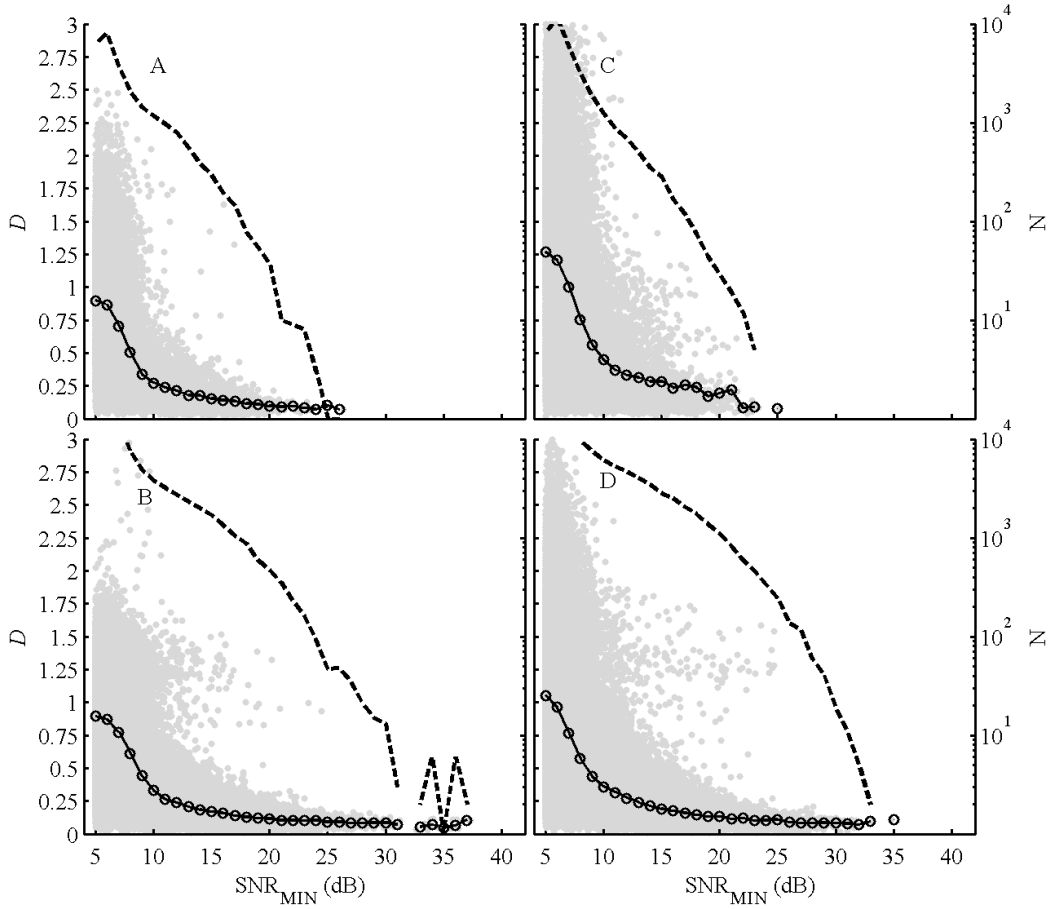

Figure 2.11: D vs. the minimum observed SNR (gray dots, left axis), with their bin average (open circles, left axis), and N data points per bin on a log scale (dashed line, right axis). For a) RFG, b) COP, c) MGS and d) SCI.

in section 2.2.5 depend on associating the radial velocity of the received signal with an estimate of the ship position within the FFT time period. As suggested by Table 2.2, errors in ship positions are likely less than the 2-3^o standard deviations of bearings traversed during the FFT time period. [31] indicates that $SNR_{MIN} = 11$ is equivalent to a bearing uncertainty of about 12^o. Thus errors in bearing resulting from GPS or other AIS position errors are likely a small fraction of the errors in estimates of $\mathbf{A}_{SHIP}$. Both of these sources of error and uncertainty are likely reduced through bin averaging of $\mathbf{A}_{SHIP}$.

While the [31] study associates SNR with bearing uncertainties (in degrees), results here associate SNR with a value of D, the difference between $\mathbf{A}_{SHIP}$ and $\mathbf{A}_{TRANS}$. Associating a value of D with a bearing uncertainty in the ocean current data is identified as a question for future investigations.

This analysis can address two additional questions regarding the generation of patterns from ships. First, how frequently can $\mathbf{A}_{SHIP}$ be generated and at what level of error? Figure 2.12 shows the number of cumulative unique bearings θ spanned by $\mathbf{A}_{SHIP}$ as a function of time ($N_{SHIP}(t)$), divided by total number of bearings in $\mathbf{A}_{TRANS}$ (N_{TRANS}; both N_{SHIP} and N_{TRANS} at 1^o resolution). Counting observations at 1^o resolution enables estimates of the time to produce five points per bin in a 5^o average. The times required to generate $\mathbf{A}_{SHIP}(\theta)$ for various error levels, set by SNR_{MIN}, are shown by the different lines. For example, Figure 2.12a shows that $\mathbf{A}_{SHIP}$ at RFG covers about 75% of the 1^o bearings of $\mathbf{A}_{TRANS}$ with $SNR_{MIN} > 10$ after 60 days. COP (Fig. 2.12b) covers about 95% of $\mathbf{A}_{TRANS}$ bearings during the same time period. $\mathbf{A}_{SHIP}$ covering 75% of $\mathbf{A}_{TRANS}$ with $SNR_{MIN} > 10$ can be generated in approximately 53 days at RFG, 9 days at COP, 12 days at MGS, and 2 days SCI. Of course these times depend on the level of ship traffic. Applying thresholds such as $SNR_{MIN} > 10$ sets error between $\mathbf{A}_{SHIP}$ and $\mathbf{A}_{TRANS}$ at $D = 0.25$ after averaging, as indicated by Fig. 2.11.

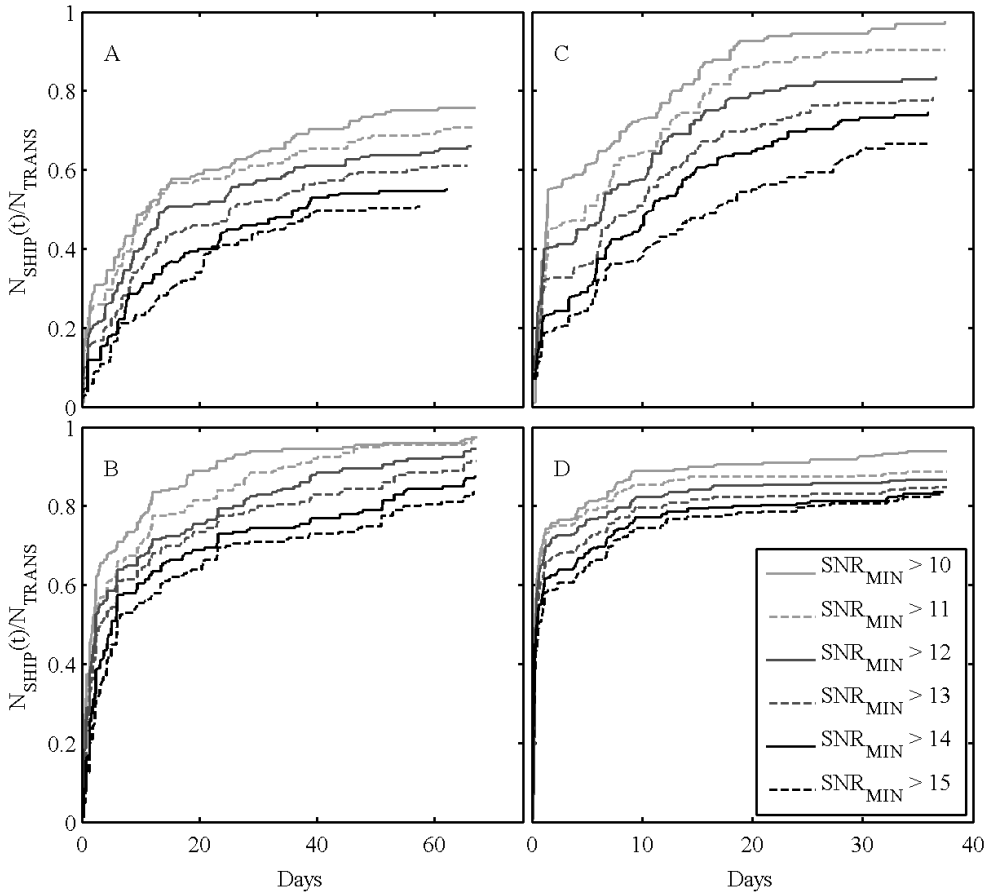

Figure 2.12: Curves showing the ratio $N_{SHIP}(t)N_{TRANS}$ vs. time in days. The five curves for each subplot are for different SNR_{MIN} thresholds (legend, Fig. 12 d). Gaps resulting from HF radar or AIS outages where truncated to one day. For a) RFG, b) COP, c) MGS and d) SCI.

Second, how many ships are needed to generate a pattern? This question can be answered by substituting the number of ships n for time t to obtain the ratio $N_{SHIP}(n)/N_{TRANS}$. Figure 2.13 shows that $\mathbf{A}_{SHIP}$ covering 75% of $\mathbf{A}_{TRANS}$ with $SNR_{MIN} > 10$ can be generated from 155 ships at RFG, 50 ships at COP, 48 ships at MGS, and 47 ships at SCI.

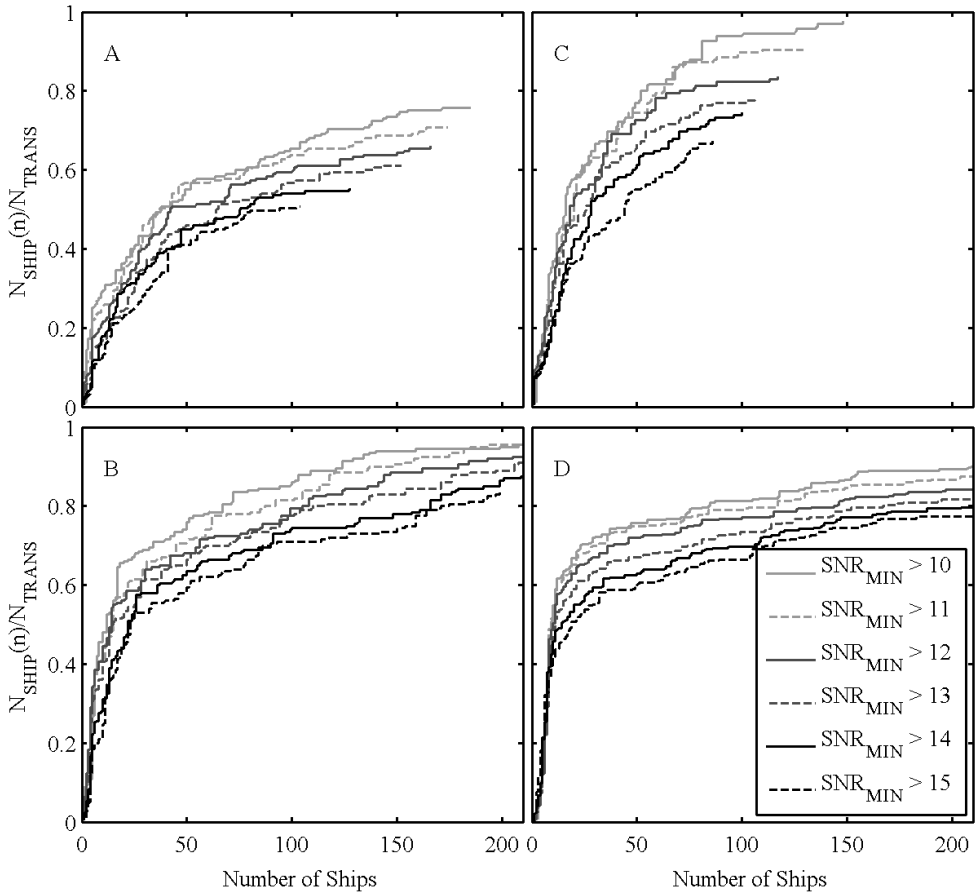

Figure 2.13: Curves showing the ratio $N_{SHIP}(n)/N_{TRANS}$ vs. the number of unique ships. The five curves for each subplot are for different SNR_{MIN} thresholds (legend, Fig. 13 d). For a) RFG, b) COP, c) MGS and d) SCI.

Results presented here demonstrate the difficultly of using ocean current HF radar for ship detection. Between 500 and 630 ships reporting positions with AIS passed within

the coverage areas of the four HF radars. Defining a positive detection as an observation with $SNR_{MIN} > 10$, between 30% and 85% of the ships where detected. However, these positive detections represent a small fraction of the time (less than about 5%) that the ships were within the coverage area. This result illustrates the need for modified HF radar processing schemes for ship detection, such as described by [32].

2.5 Conclusions

Methods presented here demonstrate the use of ship backscatter to measure antenna patterns for direction-finding HF radars. The Santa Barbara Channel, with shipping lanes within the coverage area of several SeaSonde HF radars, provides an ideal testing ground for developing this technology. The analysis supports the following conclusions:

- AIS and ship backscatter in cross spectra can be used to independently estimate the receive antenna pattern;
- The difference between transponder measured patterns and ship backscatter patterns depends on SNR_{MIN} when $SNR_{MIN} >\sim$10 dB. Using $SNR_{MIN} > 11$ dB as a threshold for ship based patterns produces low error when these are compared to patterns measured with standard methods.
- Significant fractions of the antenna pattern can be measured with as few as 50 ships of opportunity, or on timescales on the order of days depending on the local ship traffic and SNR.

Additional questions about HF radar antenna patterns that can be addressed using this method include: How do antenna patterns change through time? What causes them to change? On what time scales do they change?

These results suggest that some HF radar deployments will still require transponder calibrations, particularly at bearings near the coast, depending on ship traffic and the geography of the HF site. In unique situations (e.g. HF radar deployed on an island), the methods would cover an equivalent range of bearings. Methods presented here can provide information about APM changes at a site APM and indicate the need for a transponder calibration. In this way, the method could augment or minimize the need for transponder-based patterns. Given the cost of transponder pattern measurements, it is likely that a software implementation of this method would be a cost effective way to measure antenna patterns. Because many HF radars operate with idealized patterns, methods for automating antenna pattern measurement would significantly improve surface currents mapped with HF radar.

Chapter 3

Uncertainty Estimates for Oceanographic HF Radars

3.1 Introduction

The high spatial and temporal resolution maps of ocean surface current produced by High Frequency (HF) radars have advanced coastal oceanography by giving context to nutrient flows, improving model results and illustrating transport mechanisms, to name a few examples. While these contributions have been important, improved understanding of ocean surface processes has been limited by the fact that the HF radar measurement errors are not well quantified. These errors can be large, and their sources complex. Incomplete knowledge of the errors limit the usefulness of the data, particularly for estimating divergence and vorticity, and for applications such as pollution tracking and search and rescue. Recommendations urge the HF radar community to "develop ... uncertainty estimates so that search areas can be modeled more effectively" [5], and that "further efforts to understand error structure in HF radar derived data are clearly warranted" [6]. The purpose of this paper is to improve the understanding and quantification of error in

oceanographic HF radars.

Oceanographic HF radars commonly use one of two methods for bearing determination, beam forming [16, 33, 34] or direction finding (DF) with Multiple Signal Classification, (MUSIC, [27]). MUSIC was invented in the 1970s [23, 24, 25, 26, 27] and was later adapted for ocean current HF radars [3]. Beam forming radars typically use linear arrays of receive antennas and electronically steer the radar look direction, forming a beam, the width of which is a function of look direction. MUSIC can be used independent of receive antenna array geometry, and is considered a "super-resolution" method, with the ability to resolve signal sources separated by a fraction of the antenna beamwidth [35].

MUSIC and its class of direction finding methods are generally considered to have superior performance to beam forming [35]. For large samples and high SNR, MUSIC accuracy approaches that of the computationally demanding Maximum Likelihood method, though MUSIC shows limitations with low SNR, small numbers of samples, or closely spaced signal sources [35]. Because of the relative simplicity of beam forming, the errors in data from these radars are well understood, which is not the case for oceanographic radars employing MUSIC.

Previous publications have investigated errors in oceanographic HF radar measurements, the majority of these comparing independent measures of currents with the radar measurements. Studies using the Ocean Surface Current Radar (OSCR), a phased array system using beam forming, were successful at validating the measurement and attributing a substantial fraction of the differences to geophysical processes [16, 33, 36]. Similar methods applied later to Wellen Radars (WERA; [37]) and radars employing MUSIC [30, 11] identified errors present in the radial components and were able to attribute errors to idealized antenna patterns for the CODAR systems. Other work has shown the importance of measured antenna patterns [10, 38], the influence of spatial current

variability on velocity differences [39], and improvements in comparisons when using screening metrics based on properties of the MUSIC direction of arrival (DOA) function [40]. Simulation based evaluations have been used to compare MUSIC and beam forming [3, 41], to investigate the affect of distortions in antenna patterns [17], and to investigate MUSIC performance in different ocean current scenarios [42]. With a few exceptions [43], studies of oceanographic radars have not isolated the variables governing error, or quantified the errors in such a way that they could be estimated and used operationally.

Individual HF radars measure the component of velocity directed toward or away from the radar as a function of range and bearing. Errors in the radial velocity components result from numerous sources such as interference, variable SNR, the DF algorithm, and irregularities in the receive antenna pattern measurement (APM). The resulting errors in radial velocities then propagate into the spatially averaged total vectors. The widely used SeaSonde HF radar, manufactured by CODAR Ocean Sensors Ltd. in Mountain View, CA, produces two uncertainties termed the spatial quality factor and the temporal quality factor. These factors, actually the standard deviations in time and space of the sub-hourly measurements, may be close to the final uncertainty product needed by modelers [44], but require further verification of their utility for incorporation into total vector estimates [45]. These uncertainties are typically produced from a relatively small number of observations, and do not explicitly account for the effect of SNR on the bearing uncertainty. Others have found that screening radial data by SNR improved comparisons with in situ measurements [46]. Meanwhile in many publications on MUSIC performance it is commonly understood that the DOA accuracy is a function of the SNR [47, 48, 49].

Outside of oceanography MUSIC has been thoroughly studied and several publications derive analytical expression for error based on the DOA function. Stoica and Nehorai (1989) [4] derived the DOA error variance based on a Taylor expansion of the MUSIC

DOA function and the statistical properties of the eigenvectors of the data covariance matrix. A later paper by Xu and Buckley (1992) [50] maintained higher order terms in the expansion, resulting in an additional expression for bias error (a result independently derived elsewhere [51]). Given these expressions, it is possible to compute an estimate of the uncertainty for a given MUSIC DOA solution. In the context of oceanographic HF radars, the ability to produce a MUSIC solution along with an estimate of the directional error would go a long way toward meeting the needs of users outlined above.

The studies of MUSIC error necessarily [4, 50] make simplifying assumptions about the signal environment that may or may not apply to oceanographic HF radars. For example, they assume perfectly known antenna patterns and signals that originate from a known number of point sources in otherwise Gaussian noise. In contrast, oceanographic HF radars operate in variable environments, often with distorted APMs, interference and complex signal source distributions. Furthermore, the theoretical expressions they derive have not been evaluated for use operationally.

We evaluate the utility of the error expressions [4] as applied to oceanographic HF radars. Prior to evaluating error estimates, we review the processing of oceanographic HF radars to identify the factors contributing to errors. We then give the analytical error expressions from [4], and put them in context of oceanographic data processing. We evaluate these expressions with a simulation-based approach as done in previous publications, though with input current fields obtained from a high resolution ocean model. Finally, we demonstrate the utility of the uncertainty estimates by using comparisons along the baseline between operational radars.

3.2 Oceanographic HF Radar Processing and Errors

Fig. 3.1 summarizes the signal processing of oceanographic HF radar data. Boxes on the left are based on previous publications (Figs. 1 from both [52, 53]), and are specific to the processing of SeaSonde data [54]. Other operational HF radars use a slightly different scheme with details specific to beam forming. However, it has been shown that the scheme in Fig. 3.1 can be used for somewhat arbitrary receive antenna configurations (e.g. [55, 56]). Errors in radial velocities ($\mathbf{v}_r$) arise at several points as shown on the right in Fig. 3.1. Here we briefly summarize the signal processing, while describing the errors and uncertainties that arise in HF radar observations.

1. *Range uncertainty due to windowing.* The first FFT of the antenna voltage time series separates signals by range (c.f. [52]). Assuming the conversion of a continuous flow field into discrete range rings can be understood as a discretization process, we can use the theory for analog-to-digital conversion to estimate error in the range determination. Given a range cell width $\Delta\mathbf{r}$, the range uncertainty can be estimated [57]:

$$\sigma_{\mathbf{r}} = \sqrt{\frac{1}{12}}\Delta\mathbf{r} \approx 0.29\Delta\mathbf{r}, \tag{3.1}$$

where the factor of $\frac{1}{12}$ is the variance introduced when representing the uniformly distributed range with the discretized value. Furthermore, windowing (e.g Hamming) applied to the FMCW sweep to convert frequency to range causes 20% overlap in adjacent range cells [8], and thus an increase in the range increment. In this case, the range increment $\Delta\mathbf{r}$ is increased by a factor of 1.2, and (3.1) becomes $\sigma_{\mathbf{r}} = 0.35\Delta\mathbf{r}$.

2. *Frequency quantization error.* For oceanographic radars signals arrive nearly simultaneously from all angles within view. FFT processing of the time series produced by step 1 sorts signal variance by Doppler frequency, which are then processed by MUSIC

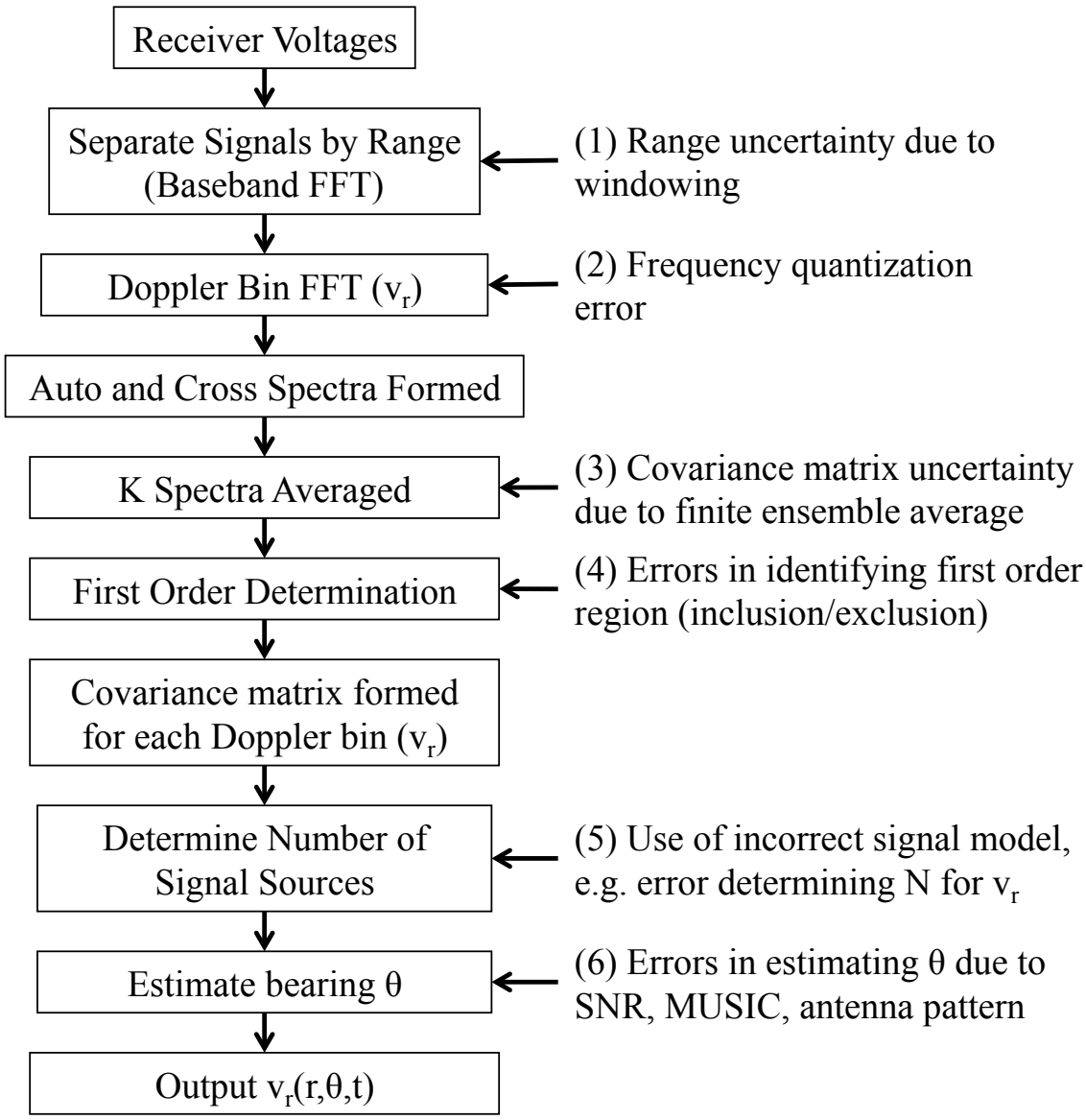

Figure 3.1: HF radar data processing flow for estimating radial velocities, with error sources. [Adapted from [52, 42]].

separately. The requirement for a noise subspace in the eigen decompositon limits MUSIC to processing only up to $M-1$ signals, while the FFT pre-processing allows a radar with just a few receive antennas (e.g. $M=3$) to produce DOA solutions for many more than M signals in a given time period. After FFT processing, HF radars (e.g. SeaSondes [54]) auto and cross multiply the FFT outputs to form power spectra.

The FFT calculation and formation of cross-spectra (c.f.[54, 53]) introduces errors in $\mathbf{v}_r$ due to the discretization of frequency bins. Using (3.1) but substituting $\Delta\mathbf{v}_r$ for $\Delta\mathbf{r}$, we can estimate the velocity uncertainty:

$$\sigma_{\mathbf{v}_r} \approx 0.29\Delta\mathbf{v}_r. \tag{3.2}$$

Here $\Delta\mathbf{v}_r$ is the radar radial velocity increment,

$$\Delta\mathbf{v}_r = \frac{\lambda_{TX}}{2}\frac{SWR}{n_{FFT}}, \tag{3.3}$$

computed with the transmitted wavelength λ_{TX}, the sweep rate (SWR), and FFT length (n_{FFT}) [8]. For a radar with $\Delta\mathbf{v}_r = 4.3$ cm s^{-1}, $\sigma_{\mathbf{v}_r} = 1.2$ cm s^{-1}, though longer FFTs reduce this to less than 1 cm s^{-1}[40, 58].

3. *Covariance matrix uncertainty due to finite ensemble averages.* After cross multiplying, we average K cross spectra, and form the covariance matrix $\mathbf{C}(f)$ for each frequency bin (c.f. [53]). Finite sampling periods and the dynamic nature of the ocean surface limit K (the number of independent estimates, or "snapshots" [49]). Uncertainty in the covariance matrix resulting from the choice of K influences the direction finding estimate as investigated below.

4. *Error in identifying first-order region.* After forming the cross spectra we must determine what portion of the spectrum contains the signal from the first order scatter-

ing process, which includes the ocean current information. To identify frequency bins containing the first order signal, operational SeaSondes use empirical methods [8], or image processing techniques [59]. Errors arise in two ways: 1) when non-current signal is interpreted as originating from ocean currents; or 2) when signal from ocean currents is excluded from processing. These errors can be large in uncommon situations, such as when high winds (> 15 m s^{-1}) combine with strong currents (> 2 m s^{-1}), causing the first order and second order signal regions to become indistinguishable [60]. On average, these errors are probably less than or equal to the reported 2-8 cm s^{-1} [30, 58] noise levels, based on estimates from the power spectra of the HF radar currents.

5. *Incorrect determination of the number of signal source bearings.* Once the $M \times M$ covariance matrix has been formed, MUSIC finds the eigen-structure by decomposing the covariance matrix into M orthogonal eigenvectors and eigenvalues, and then uses the noise eigenvectors to determine the source DOA(s) (c.f.[27, 61, 62]). The SeaSonde uses a hypothesis testing approach to determine if the covariance matrix results from a single bearing $N = 1$, or from dual bearings $N = 2$ [8]. In some situations, such as low SNR, the distinction between a single or dual bearing situation becomes unclear. Discriminating between the two can lead to errors.

For both the SeaSonde and other arrays, the impact of incorrect determination of N has not been quantified. Previous work [54] suggests changes in SeaSonde hypothesis testing parameters that lead to more dual angle solutions, reducing gaps in maps of $\mathbf{v}_r$. The role of hypothesis testing in producing gaps makes this source of error difficult to quantify. A Simulation based study using an 8-element array indicated problems determining N, leading to high errors in the resulting DOAs [41]. Another potential source of error, discussed later, is the possibility of the ocean surface presenting situations with $N > M - 1$. The performance of MUSIC when $N > M - 1$ has not received much

attention, though several publications investigate MUSIC performance for spatially non-white noise (e.g. [63]) which may have a similar impact on the accuracy of the DOA solutions.

6. *Error in estimating the DOA*. As implemented for oceanographic HF radar processing, MUSIC errors result in either misplaced $\mathbf{v}_r$ in θ, or in an inability to determine θ for a given $\mathbf{v}_r$. Several factors contribute to errors in θ that result from MUSIC. As mentioned above, the covariance matrix is formed from the average of a limited number of time series segments (K). This produces uncertainty in the data covariance matrix and resulting DOA estimate. Other factors include the SNR, the accuracy and characteristics of the antenna pattern measurement, and the angular separation of the signal sources (c.f. [48]).

The effects of some of these have been identified for oceanographic HF radars, with one study finding average errors as large as 19^o resulting from the use of ideal patterns [30], with other studies finding errors in θ in the range $0 - 10^o$ when measured antenna patterns were used [10, 11, 38, 40]. Some work suggests that errors related to the antenna pattern are more likely to present themselves as a bias, rather than as a random error [15, 64, 10]. A simulation based study found no relationship between SNR and DOA accuracy for radars with MUSIC [41], but this was likely due to the use of minimum SNRs in the range of 10-15 dB. A later study suggested a substantial decrease in accuracy beginning around 10 dB, based on the relationship between SNR and error in deriving APMs from ship backscatter [1].

Of these six sources of error, 6. *Error in estimating the DOA* is the error for which analytical expressions exist for estimating the resulting uncertainty.

3.3 Signal Models and Simulation Methods

To present expressions for the error variance, we must first define the data model and related notation. In the simplified case of N discrete signal sources ($N < M$), following [27, 4] we define the voltage time series measured at the receive antenna output ($\mathbf{Y}$) as the product of the N signal sources impinging on the array from bearings $\theta_1, \theta_2, ..., \theta_N$ given by $\mathbf{X}(t)$, and the array response $\mathbf{A}$, plus noise $\mathbf{e}(t)$:

$$\mathbf{Y} = \mathbf{A}\mathbf{X}(t) + \mathbf{e}(t). \tag{3.4}$$

Here the $M \times N$ matrix $\mathbf{A}$ gives the the response of the M antennas to each signal source,

$$\mathbf{A} = \begin{bmatrix} | & | & & | \\ \mathbf{a}(\theta_1) & \mathbf{a}(\theta_2) & ... & \mathbf{a}(\theta_N) \\ | & | & & | \end{bmatrix}, \tag{3.5}$$

where the $M \times 1$ vectors $\mathbf{a}(\theta)$ represent the antenna pattern at each θ. The $N \times K$ matrix $\mathbf{X}(t)$, gives the typically complex valued signal from the N discrete sources, described below. Noise given by the $M \times K$ vector $\mathbf{e}(t)$ is assumed to be Gaussian-distributed with zero mean and variance σ^2. Given $\mathbf{A}$, the source locations θ_N, and $\mathbf{e}(t)$, we compute $\mathbf{Y}$ with (3.4) and then the $M \times M$ data covariance matrix,

$$\mathbf{C} = \frac{1}{K}\mathbf{Y}\mathbf{Y}^H, \tag{3.6}$$

where H denotes the Hermitian conjugate. The matrix $\mathbf{C}$ forms the input to MUSIC. Expressions (3.4), (3.5) and (3.6) define the basic signal model for a general $\mathbf{X}(t)$.

3.3.1 Discrete Source Model

We first use (3.4) with a relatively simple $\mathbf{X}(t)$, which allows us to investigate error estimates in simplified scenarios, before applying them to complex simulations of ocean backscatter. Here we define $\mathbf{X}(t)$ as an $N \times K$ matrix of K independent realizations of up to $N = M-1$ point sources. The time series from each source, located at $\theta_1, \theta_2, ..., \theta_N$ are made up of zero mean, normally distributed random numbers [65]. This model defines independent, discrete signal sources commonly used to test DOA methods (e.g. [49]). For each Monte-Carlo simulation, we vary both the values for sources ($\mathbf{X}(t)$), and the noise $\mathbf{e}(t)$, with a given SNR.

3.3.2 Oceanographic Radar Simulations

For simulations of backscatter from oceanographic HF radars, we use a modified version of the signal model used in previous studies [3, 41, 53, 17]. Following these we define $\mathbf{X}(t)$,

$$\mathbf{X}(t) = \boldsymbol{\gamma}_+ \exp\left(i(\omega_B + \boldsymbol{\omega}_c)t\right) + \boldsymbol{\gamma}_- \exp\left(i(-\omega_B + \boldsymbol{\omega}_c)t\right). \tag{3.7}$$

The expression (3.7) models the signal backscattered from the ocean surface, with combined Doppler shift resulting from the advancing and receding Bragg-resonant waves ($\pm\omega_B$) and the currents ($\boldsymbol{\omega}_c$). We compute $\omega_B = (2k_{TX}g)^{\frac{1}{2}}$ based on the radar wave number $k_{TX} = \frac{2\pi f_{TX}}{c}$, the radar transmit frequency f_{TX}, the gravitational acceleration g and the speed of light c. The radial component of the ocean surface current provides $\mathbf{v_r}$ for computing $\boldsymbol{\omega}_c = 2k_{TX}\mathbf{v_r}$. The matrix $\boldsymbol{\gamma}_\pm$ defines a decorrelation factor discussed below.

Prior to producing the covariance matrix, our simulations follow the processing steps

used by oceanographic radars as explained in step 2 above. After forming $\mathbf{Y}$, we compute the FFTs and then auto and cross multiplying these to form power spectra. After averaging K of these, we identify frequency bins containing the first order signal [59], and form the covariance matrix $\mathbf{C}(f)$ for each frequency bin separately (c.f. [53]).

In simulations for this study we obtain $\mathbf{v_r}$ from the 100m resolution Regional Ocean Modelling System (ROMS) [66]. ROMS is a Reynolds-averaged numerical simulation with turbulence parameterized on scales smaller than scales typically resolved by the HF radar. We divide the ROMS $\mathbf{v_r}$ into 1.5 km range cells, each with $\mathcal{O}(1 \times 10^4)$ grid points, such that $\mathbf{v}_r$ defines $\mathbf{X}(t)$ with (3.7) at all θ in view of the simulated radar. Fig. 3.2 shows an example of the radial component of the hourly averaged ROMS surface currents for a simulated range cell, between 15 km and 16.5 km range. The radial currents in the example span 180^o, with $n = 7426$ data points, such that each 1^o bin is resolved by about 41 grid points. Previous studies used simpler ocean current scenarios, such as a uniform flow with a random component to represent small scale turbulence [3], a current jet [41], or radial currents resulting from a large eddy [42]. We speculate that the complex radial velocity profiles obtained from ROMS are more representative of the real ocean, and that they provide a realistic and rigorous test of error estimation schemes.

The factor $\boldsymbol{\gamma}_{\pm}$ in (3.7) decorrelates simulated signals, modelling a poorly understood process occurring with ocean backscatter. While signals backscattered from the sea surface ultimately originate from a single source (the transmit antenna), it is generally assumed that the signals become uncorrelated after scattering from the sea surface, for angular separations as small as $0.5^o - 2.0^o$ [8, 3]. The reference [8] attributes the value of 0.5^o to [67], which discusses de-correlation times (about $25s$) rather than angular separations, and speculates that the mechanism decorrelating the signals is the differential motion of scattering ocean wave trains. Given these unknowns, we decorrelate signals at

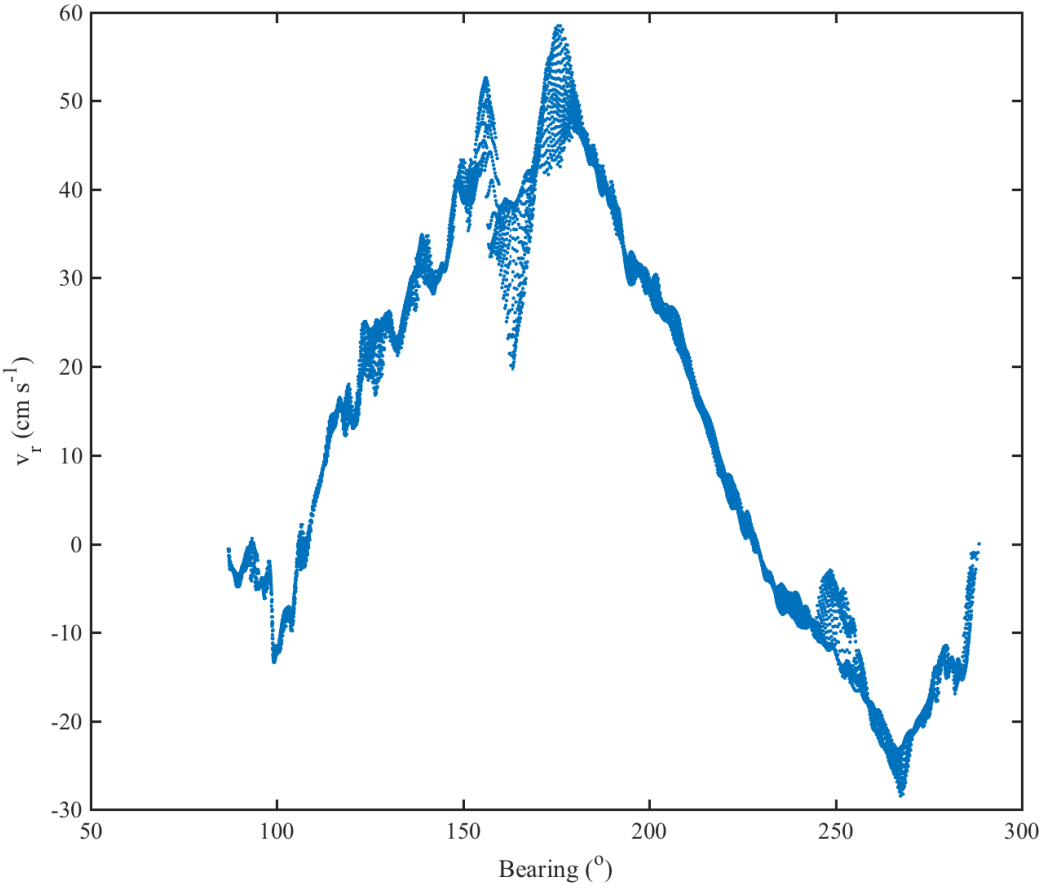

Figure 3.2: Radial velocity vs. Bearing from the Regional Ocean Modeling System (ROMS), found in a 1.5 km wide range cell, 19.5 km from a simulated HF radar site.

less than 1^o when modeling the backscattered signal.

In terms of the direction of arrival estimation, 1^o is typically less than the resolution of MUSIC, defining resolution as the "ability to distinguish between tightly spaced" sources [48]. The MUSIC resolution limit is approximated by,

$$\Delta\theta = \theta_{HPBW} SNR^{-\frac{1}{p}}, \tag{3.8}$$

where p ranges between $2-4$ [48, 68]. To estimate $\Delta\theta$ we first compute the half-power beamwidth (θ_{HPBW}) by first computing the beam pattern $\mathbf{B}$ following [49],

$$\mathbf{B} = \frac{1}{M}\mathbf{A}(\theta_o)^H\mathbf{A}(\theta), \tag{3.9}$$

where θ_o is a reference angle, and then finding θ_{HPBW} as the range of θ where $|\mathbf{B}|^2 \geq 0.5max|\mathbf{B}|^2$ [49]. Defined this way, the SeaSonde $\theta_{HPBW} = 131^o$, while a uniform linear array (ULA) with $\frac{1}{2}\lambda_{TX}$ spacing and M=16 has $\theta_{HPBW} = 6.5^o$. These values suggests minimum $\Delta\theta$ on the order of 25^o for the SeaSonde. Using data we processed from SeaSondes (which has the individual MUSIC solutions) we plotted the angular difference between dual bearing solutions vs SNR (not shown) indicating a minimum $\Delta\theta$ on the order of 10^o. For the purposes of simulating ocean current backscatter, these results suggest that decorrelating sources separated by $\sim 1^o$ adequately approximates backscatter from the ocean surface.

To decorrelate simulated signals, we construct $\boldsymbol{\gamma}_\pm$ beginning with an $N \times 1$ vector of zero mean normally distributed random numbers, $\gamma_\pm$. We then compute $\boldsymbol{\gamma}_\pm = diag(\gamma_\pm)$, resulting in an $N \times N$ matrix with non-zero values only on the diagonal. We draw new values of $\boldsymbol{\gamma}_\pm$ for each data snapshot, with differnent values multiplying both the approaching $\boldsymbol{\gamma}_+$ and receding $\boldsymbol{\gamma}_-$ Bragg peaks separately. Without this randomizing com-

ponent, the simulation equations present constant, correlated sources of signal. Previous simulation-based studies model wind, assuming a Pierson-Moskowitz cardioid pattern [69] as a function of θ that multiplies $\mathbf{A}$ in (3.4), with randomness that decorrelates signals in the way that we use $\boldsymbol{\gamma}_{\pm}$ [3, 41]. Essentially $\boldsymbol{\gamma}_{\pm}$ in (3.7) is equivalent to assuming a uniform presence of Bragg waves, while the use of the Pierson-Moskowitz model for the wave field is equivalent to assuming fully developed seas.

In processing the DOA solutions from the ocean current radar simulations, we perform the signal detection step (5. above and in Fig. 3.1) using a 'clairvoyant' method. The purpose of the signal detection step is to determine if the data covariance matrix is the result of N signal sources, where $N \in \{1, 2, ..., M-1\}$. With simulations, we can determine N directly from the simulation inputs, i.e. the profile of $\mathbf{v}_r$. For example in Fig. 3.2 radial velocities less than -23 cm s^{-1} occur only in the region spanning $265^o - 270^o$. We designate this case a 'single bearing' case, with other cases termed 'two bearing' (velocities between 2.4 and 9.5 cm s^{-1}), and 'three bearing' (velocities between 26 and 30 cm s^{-1}). Thus the profiles of $\mathbf{v}_r$ require some interpretation for determining N, as the criteria for what constitutes a spatially coherent source patch is somewhat subjective, but this method removes signal detection as a significant source of error in the DOA solutions.

3.4 Error Calculations

3.4.1 Analytical DOA Uncertainty Expressions

Stoica and Nehorai (1989) derive an expression for the MUSIC DOA error variance based on the statistical properties of the errors in the eigenvectors of $\mathbf{C}$ [4]. Beginning with the M eigenvalues of $\mathbf{C}$, $\lambda_1, ...\lambda_M$, we associate the largest N with the signal and

form the $M \times N$ matrix of signal eigenvectors $\mathbf{S} = [\mathbf{s}_1, ..., \mathbf{s}_N]$. We then associate the remaining $M - N$ eigenvectors with the noise, and form the $M \times (M - N)$ matrix $\mathbf{G} = [\mathbf{g}_1, ..., \mathbf{g}_{M-N}]$. The MUSIC error variance of the i^{th} DOA is then given by:

$$\sigma^2_{MU} = \frac{1}{2K} \frac{\mathbf{a}^H(\theta_i)\mathbf{U}\mathbf{a}(\theta_i)}{h(\theta_i)}, \tag{3.10}$$

where $\mathbf{U}$ is defined,

$$\mathbf{U} = \sigma^2 \left[\sum_{k=1}^{N} \frac{\lambda_k}{(\sigma^2 - \lambda_k)^2} \mathbf{S}_k \mathbf{S}^H{}_k \right], \tag{3.11}$$

and $h(\theta_i)$ is given by,

$$h(\theta_i) = \frac{d\mathbf{a}(\theta)}{d\theta}^H \mathbf{G}\mathbf{G}^{\mathbf{H}} \frac{d\mathbf{a}(\theta)}{d\theta}, \tag{3.12}$$

given the noise variance σ^2 (in volts^2), the receive array vector $\mathbf{a}(\theta)$, and its derivative with respect to θ. As the eigenvalues approach the noise variance, the denominator in (3.11) goes to zero, or $(\sigma^2 - \lambda_k) \rightarrow 0$, and the MUSIC error variance becomes large. The expressions (3.10)-(3.12) produce estimates of the error variance in radians squared. We define the DOA uncertainty σ_{MU} as the positive square root of (3.10) converted into degrees.

Assuming an ideal pattern for SeaSondes, the array derivative in (3.12) can be evaluated analytically, but for APMs from operational radars we must evaluate the array derivative numerically. We compute these derivatives using the second order accurate centered difference:

$$\frac{da(\theta_j)}{d\theta} = \frac{a(\theta_{j+1}) - a(\theta_{j-1})}{2\Delta\theta}, \tag{3.13}$$

with edges evaluated using the first order accurate, forward and backward one-sided approximations [70].

3.4.2 Cramer-Rao Lower Bound

In addition to estimates of σ_{MU}, we show the Cramer-Rao Lower Bound (CRB), which is the statistical lower bound on the error variance for any DOA calculation [4, 48]. Here we use its square root (σ_{CRB}) to illustrate factors controlling the DOA error, to compare with uncertainties estimated with (3.10), and to compare with simulation results. We compute the CRB from assumed values of SNR, K, N, and the antenna pattern $\mathbf{a}(\theta)$. Following [48] we estimate a covariance matrix $\mathbf{C}_y$ directly from these known variables, along with the identity matrix $\mathbf{I}$,

$$\mathbf{C}_y = \sum_{n=1}^{N} SNR_n \mathbf{a}(\theta_n)\mathbf{a}(\theta_n)^H + \mathbf{I}. \tag{3.14}$$

We then define the $(i,j)^{th}$ element of the $N \times N$ Fisher Information matrix,

$$\mathbf{F}_{i,j} = trace\left[\mathbf{C}_y^{-1}\frac{\partial \mathbf{C}_y}{\partial \theta_i}\mathbf{C}_y^{-1}\frac{\partial \mathbf{C}_y}{\partial \theta_j}\right]. \tag{3.15}$$

From $\mathbf{F}$ the CRB is given by,

$$\sigma^2{}_{CRB} \geq \frac{1}{K}\mathbf{F}^{-1} \equiv CRB. \tag{3.16}$$

The derivative of $\mathbf{C}_y$ with respect to θ in (3.15) is computed as,

$$\frac{\partial \mathbf{C}_y}{\partial \theta_i} = SNR_i \frac{d\mathbf{a}(\theta_i)}{d\theta}\mathbf{a}(\theta_i)^H + SNR_i \mathbf{a}(\theta_i)\frac{d\mathbf{a}(\theta_i)^H}{d\theta}, \tag{3.17}$$

and the array derivatives are computed with (3.13).

3.4.3 Simulation DOA Errors

We show the errors in the DOA estimates as the RMS difference between the simulated source bearing, designated θ_S, and the DOA determined with MUSIC θ_{MU}. We compute the RMS difference (σ_{RMS}) for a given ensemble of DOA solutions (n) as,

$$\sigma_{RMS} = \sqrt{\frac{\sum_{i=1}^{n} (\theta_{S_i} - \theta_{MU_i})^2}{n}}. \tag{3.18}$$

A typical ensemble includes all points within a given range of SNR. For discrete source simulations with the source θ specified, calculation of (3.18) is straightforward. However, when computing σ_{RMS} for simulations using ROMS, the calculation is more complex. In this case, a DOA solution θ_{MU}, associated with a given $\mathbf{v}_r$, results from signal that may originate from a wide range of bearings. For example, the radial currents in Fig. 3.2 has $\mathbf{v}_r = 40$ cm s^{-1} for bearings between $150^o - 170^o$ and $185^o - 190^o$, meaning that θ_S can take on any value in this range. When computing the error with a DOA solution θ_{MU}, we retain the smallest difference $\theta_{S_i} - \theta_{MU_i}$ for use in (3.18), using the value of θ_S from the current field that is closest to the DOA solution.

3.5 Results

3.5.1 Simulations with Discrete Source Model

Figures 3.3a-c show the result of simulations of two point sources located at -22.5^o and 22.5^o for three different antenna arrays and variable SNR. For each value of SNR, ranging from 1 to 30 dB, we ran 500 simulations with $K = 9$. The figures show σ_{RMS} along with the average of σ_{MU} computed with (3.10), for 1 dB SNR bins. After averaging, σ_{MU} tracks σ_{RMS} for SNR>10 dB. The CRB (σ_{CRB}) from (3.16) is also shown, with

σ_{MU} approaching σ_{CRB} for SNR>25 dB. Each y-axis changes scale, demonstrating the different accuracies expected for each array. The signal sources were located near the broadside axis of the ULAs, where optimal performance is found, in contrast with the SeaSonde array which has no preferred direction. The change in accuracy also reflects the monotonic decrease in σ_{MU} (and σ_{RMS}) with increasing M [4].

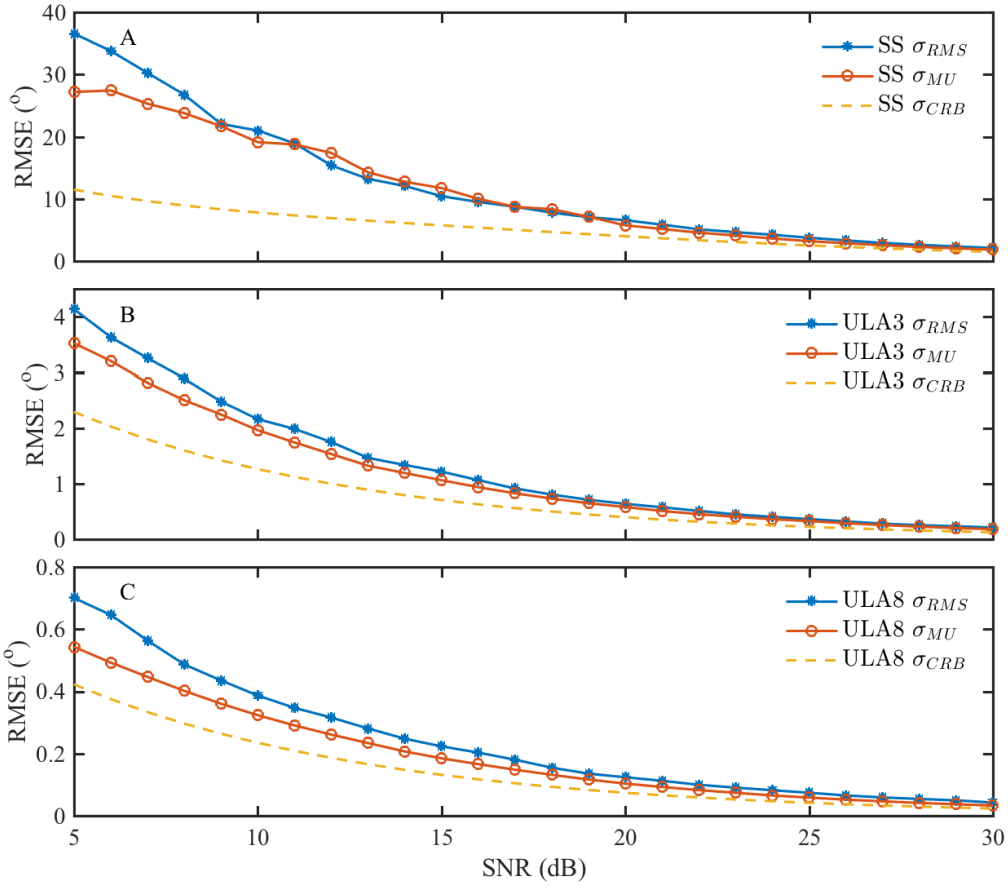

Figure 3.3: RMS error in a simulation of two point sources as measured (σ_{RMS}), as estimated with Eqn. 3.10 based on Stoica and Nehorai (1989) (σ_{MU}), and as predicted by the Cramer-Rao Lower Bound (σ_{CRB}); a) for a SeaSonde array; b) for a 3 element uniform linear array (ULA3); c) for an eight element ULA (ULA8).

The idealized simulation (3.4) allows us to investigate the effect of varying K on σ_{RMS} and σ_{MU} estimation. Uncertainties computed with (3.10) apply "for sufficiently

large values of" K [4], while suggested values of K when forming the data covariance matrix for MUSIC include $K > 3M$ [48], $K > M$ when SNR is "sufficiently strong" [50, 71], and $K = 10M$ (the "moderate snapshot region")[49]. Since oceanographic HF radars employing MUSIC observe a statistically non-stationary source of signal it is desirable to know a minimum value for K, along with the consequences for choosing small K. SeaSonde HF radars commonly use K = 2.34 (non-integer due to windowing), while other systems have used $K = 15$ to $K = 20$ (e.g.[58]).

Figure 3.4 illustrates the influence of K on σ_{RMS} and σ_{MU}. To produce this figure we simulated two sources 45^o apart, impinging on the SeaSonde array for three values of SNR and allowing K to vary between 1 and 15 (500 runs each). The uppermost curves show σ_{RMS} and σ_{MU} for SNR = 10dB. The curves show σ_{RMS} increasing rapidly for $K < 5$. We observer little improvement in σ_{RMS} for $K > 9$. When SNR = 10dB, σ_{MU} uncertainty estimates provide only a rough approximation of σ_{RMS}. However, as shown by the 15 dB and 20 dB curves σ_{MU} closely tracks σ_{RMS} when $K > 6$. For the SeaSonde these results suggest $K \geq 6$ (or $K \geq 2M$) will provide DOA observations with relatively low error while maintaining high temporal resolution. A values of $K = 6$ implies temporal averages of about 25 min when using 256 s FFTs. These figures also show the utility of σ_{MU} for estimating uncertainties in an idealized simulation.

3.5.2 Oceanographic Radar Simulations

Beginning with the $\mathbf{v}_r$ depicted in Fig. 3.2, we ran 100 Monte Carlo simulations for each SNR on the interval 5-30 dB, simulating signal voltages received on the SeaSonde array, and processing the signals as described in Section 3.2. After partitioning for each of these cases by empirically determined N, we bin averaged results by SNR with 2 dB bins. Fig. 3.5 shows σ_{RMS} and σ_{MU} for different values of N. Overall, σ_{RMS} are lower

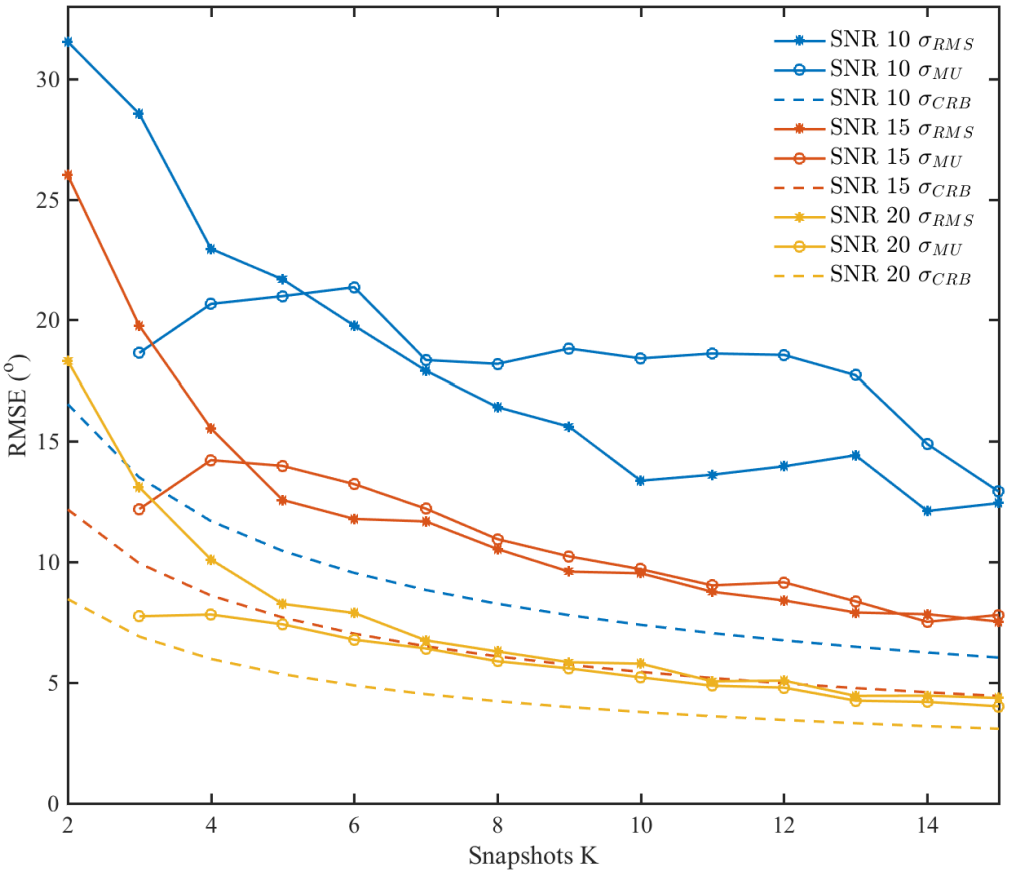

Figure 3.4: RMS error (measured σ_{RMS}, estimated σ_{MU}, and theoretical lower bound σ_{CRB}) in simulation of two point sources with variable snapshots (K), for SNR=10, 15 and 20 dB.

than those obtained with the point source simulation (e.g. Fig. 3.3a), likely due to the way we compute σ_{RMS} for ocean radar simulations. Values of σ_{RMS} increase with increasing complexity in the flow field, as shown comparing the single bearing case with two and three bearing cases. For two and three bearing cases, σ_{RMS} are large when SNR<10 dB. Averaged σ_{MU} values approximate σ_{RMS}, slightly over-estimating the error with increasing current field complexity. Shaded regions show widths of the σ_{MU} bin standard deviations. The bin standard deviations demonstrate the effectiveness of the σ_{MU} estimate for the one and two bearing cases, while showing the large scatter for the three bearing case when SNR<15 dB.

For the operational use of σ_{MU}, an important consideration is how many estimates of σ_{MU} to average for accurate estimation of σ_{RMS}. The curves of σ_{MU} and σ_{RMS} in Fig. 3.5 are averages of large numbers of ensembles, and these may have large standard deviations, such as when SNR<15, or when the flow field is complex. When processing real time data, we can average σ_{MU} in time and/or space to improve the estimation of σ_{RMS}. In order to address this issue we performed the following calculations. Beginning with MUSIC DOAs from simulations with ROMS, along with associated σ_{MU} estimates, we group results into 10 dB blocks by SNR, centered on 5 dB, 15 dB and 25 dB. Within each block, we randomly select n samples, computing the mean value of σ_{MU}, (defined as $\bar{\sigma}_{MU}$), and the mean value of σ_{RMS} ($\bar{\sigma}_{RMS}$). We repeat this process, resampling each time, producing many realizations ($N_{resample}$ =1000) of $\bar{\sigma}_{MU}$ and $\bar{\sigma}_{RMS}$ for a given value of n. From this sample, we then compute the RMS difference of $\bar{\sigma}_{MU}$ and $\bar{\sigma}_{RMS}$,

$$\sigma_n = \sqrt{\frac{\sum_{i=1}^{N_{resample}} (\bar{\sigma}_{MU_i} - \bar{\sigma}_{RMS_i})^2}{N_{resample}}}. \tag{3.19}$$

This process is repeated for $n = 1$ to $n = 40$. We then plot σ_n vs. n in Fig. 3.6. As n becomes large, the difference between $\bar{\sigma}_{MU}$ and $\bar{\sigma}_{RMS}$ (shown by σ_n) becomes small.

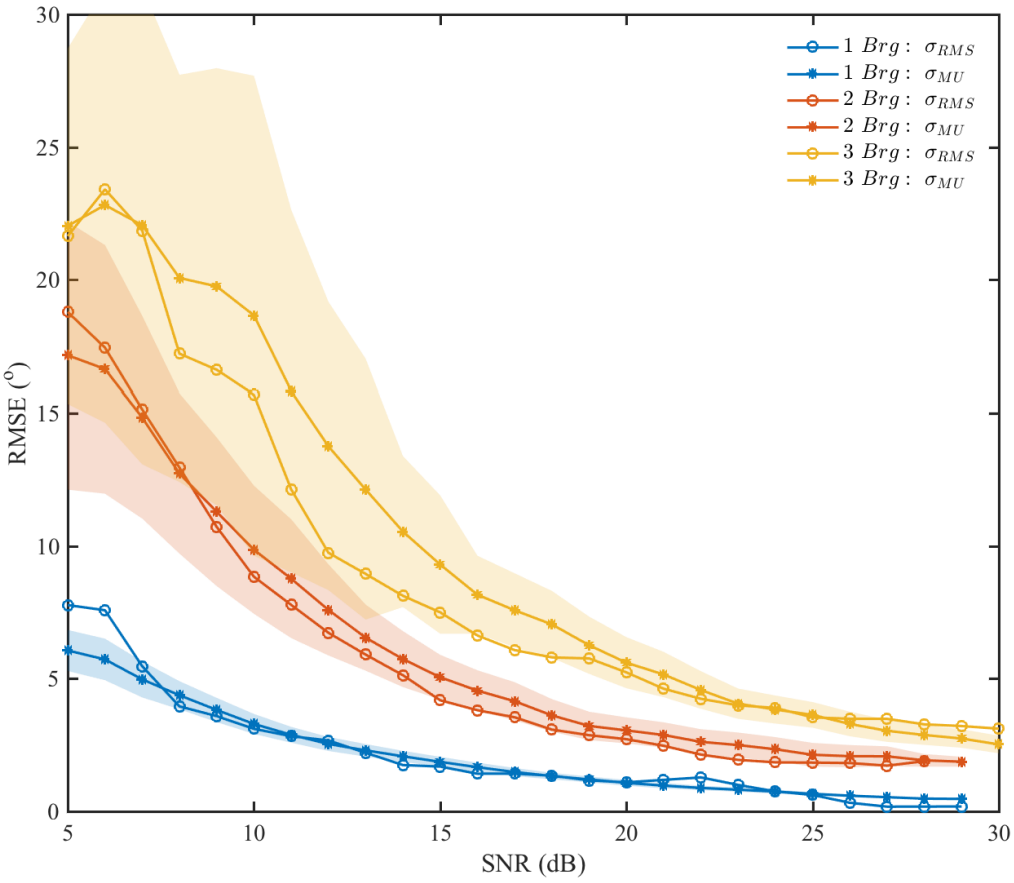

Figure 3.5: RMS errors (measured σ_{RMS}, estimated σ_{MU}), for radar simulations with input current field from ROMS, when the same velocity is present at a single bearing (1 Brg), two bearings (aka Dual bearing case: 2 Brg), and three bearings (3 Brg). Shaded regions show width of the bin standard deviations for the σ_{MU} curves.

The Fig. 3.6 results suggest that σ_{MU} approaches σ_{RMS} as $n \geq 10$, indicating that σ_{MU} estimates would be improved when HFR processing schemes include substantial averaging.

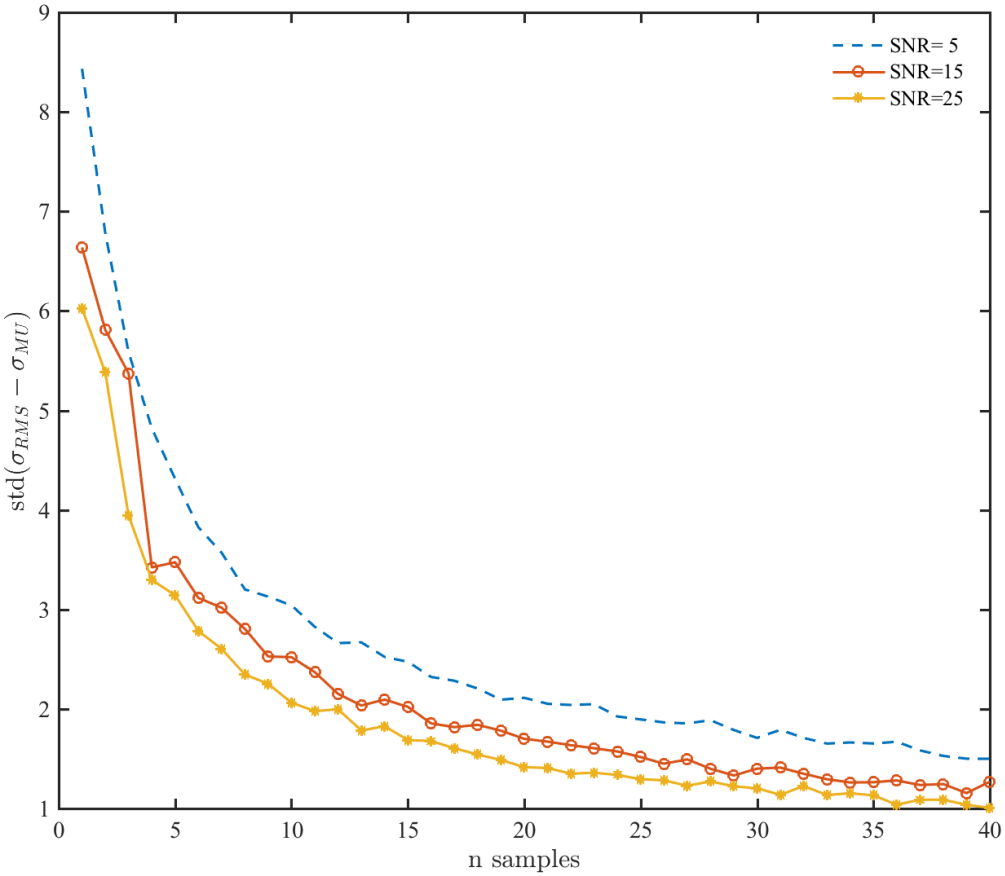

Figure 3.6: Standard deviation of the difference between measured σ_{RMS} and estimated σ_{MU} RMS error, for 1000 randomized trials when n samples are used to compute σ_{MU}: SNR = 5, 15 and 25 dB.

3.5.3 Application to Operational Radars

Uncertainty estimates were evaluated for use operationally by processing spectra from two SeaSondes, located at Santa Cruz Island, CA (SCI1) and San Nicolas Island, CA

(SNI1), using software we developed. Starting with unaveraged SeaSonde spectra files (CSQ), the software follows most of the methods and conventions of the SeaSonde processing scheme [54] with a few differences. First we increased temporal averaging of the cross spectra was performed in order to increase K and improve σ_{MU} estimates as suggested by the Fig. 3.4 results. Rather than running the DOA processing on 10 minute moving averages of auto and cross spectra, as is typical for SeaSonde processing, we computed moving averages of $K = 16$ auto and cross spectra every 10 minutes. Since each spectrum is the FFT of 256 s of data, the average covers 68.3 minutes. The other main difference was the use of the First Order Line (FOL) toolbox [59] for first order region identification. Antenna patterns were obtained for both sites using the methods of [1] with two months of data.

Figure 3.7 shows time series of $\mathbf{v}_r$ from near the baseline between SCI1 and SNI1, for the interval 10-12 Aug 2013. The plots show observations of $\mathbf{v}_r$ every 10 min from the spatial area within $\pm 1^o$ in bearing and ± 3 range cells of the mid-point between the sites for a total of 21 locations on each radial grid. Vertical bars at each velocity observation show the σ_{MU} error estimate in degrees. In general, smaller σ_{MU} occurs when $\mathbf{v}_r$ falls into groups, suggesting that the repeatable observations of $\mathbf{v}_r$ have lower DOA errors. Based on inspection of the cross spectra, observations of $\mathbf{v}_r$ near 100 cm s^{-1} in Fig. 3.7a result from ship backscatter. Slight differences overall in σ_{MU} from both sites are evident, with median σ_{MU} values (SCI1: 3.9, SNI1: 5.3) reflecting the slightly higher average SNR at SCI1.

Figure 3.8 shows the spatial distribution σ_{MU}, averaged over 10 days (10-20 Aug 2013). The figures shows a wide range of average values, along with high values found at particular bearings. The prevalence of bearings with high values of σ_{MU} in Fig. 3.8, and the outliers with high values of σ_{MU} in Fig. 3.7 suggest the use of σ_{MU} as a quality

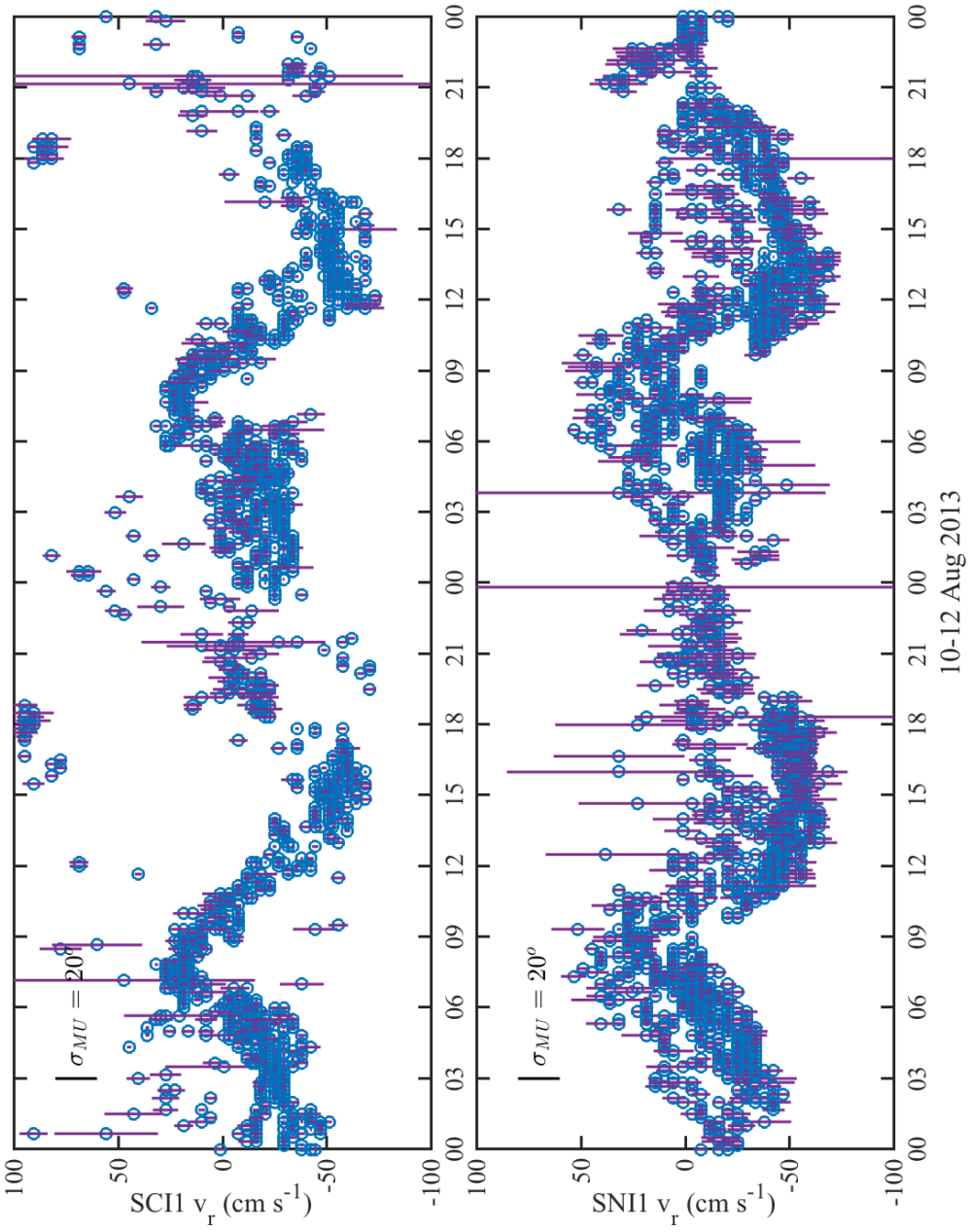

Figure 3.7: Radial velocity (cm s^{-1}) vs. time with σ_{MU} for HF radars at a) Santa Cruz Island (SCI1), and b) San Nicolas Island (SNI1), at 10 min intervals from 0000 10Aug2013 to 0000 12Aug2013.

control metric.

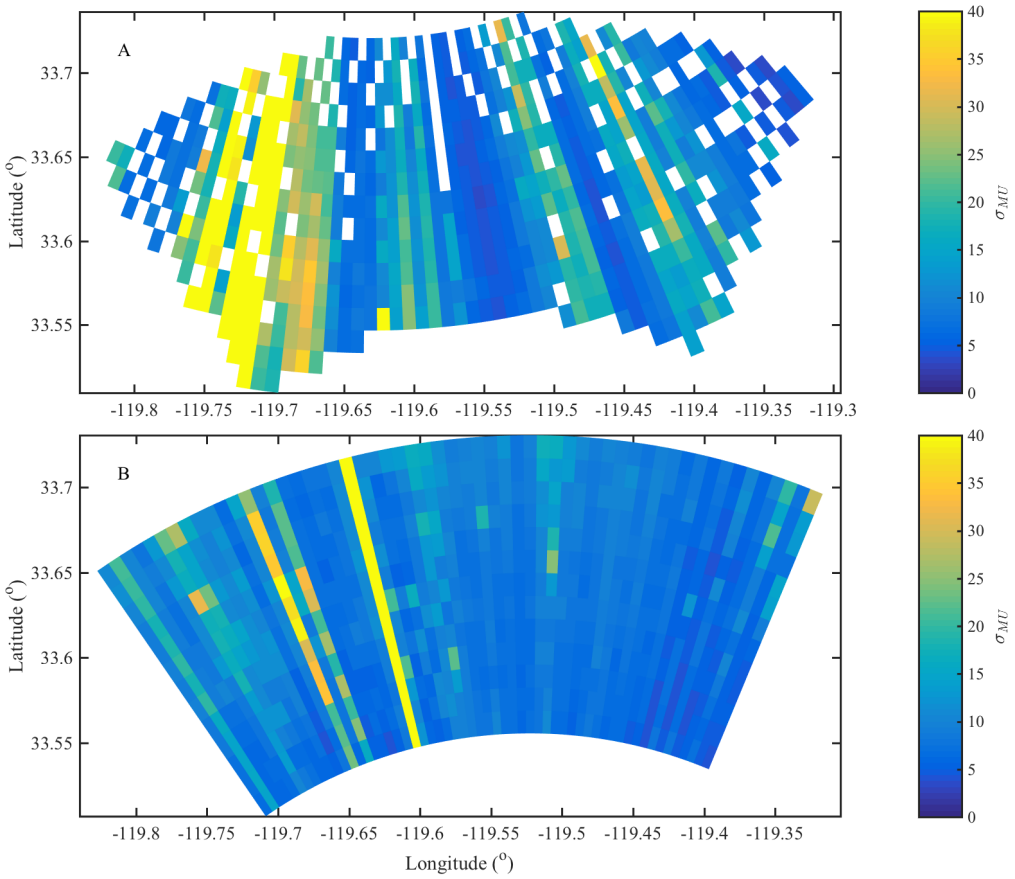

Figure 3.8: Average of σ_{MU} over 10-20 Aug2013 for a) SCI1 and b) SNI1.

Using the near the baseline data described for Fig. 3.7, we compute comparison statistics (RMS difference (RMSD) and r^2) between the two time series, varying the threshold value of σ_{MU} for removing data. To maintain a consistent number of data points in the comparison statistics, we draw random samples from the time series such that r^2 and RMSD are computed based consistently on 600 data points. Fig. 3.9 shows a) r^2 and b) RMSD, vs. the threshold value of σ_{MU} along with the standard deviation of the random samples. The comparison statistics improve for small values of the σ_{MU}

threshold. Assuming that σ_{MU} provides a valid estimate of the bearing uncertainty, Fig. 3.9 suggests that removing all but the lowest error data will provide the best comparison. Similar results were found for differences in the spatial area and sampling scheme. We interpret the Fig. 3.9 results as an indication that the σ_{MU} estimates contain useful information about the DOA uncertainty.

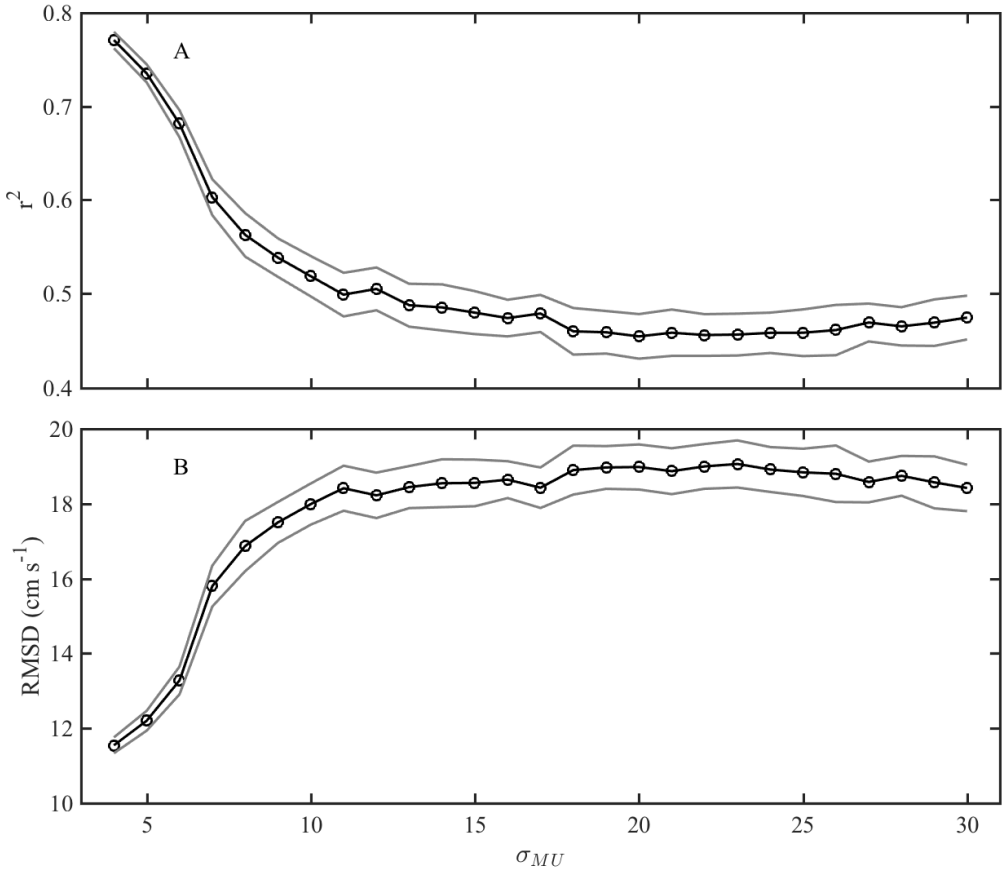

Figure 3.9: Comparison statistics between velocities measured at SCI1 and SNI1, after removing velocities with values of σ_{MU} greater than x-axis values. The statistics a) r^2 and b) RMS difference are computed for 100 random trials of 600 data points. Grey lines show region of one standard deviation of the results from the random trials.

3.6 Discussion

Both the σ_{MU} and σ_{CRB} estimates illuminate factors controlling error in the DOA of oceanographic radars. Taken together, σ_{CRB} and σ_{MU} show that error in the DOA estimate depends on K, the SNR, the specific receive array, and its antenna pattern. These include both the design of the receive array, such as linear array vs. SeaSonde, and the array derivative with respect to θ. Though not present in the expression for σ_{MU}, the number of array elements (M) implicitly factors into the DOA error and σ_{MU} estimate [4]. The dependence on array design implies different theoretical accuracies for different arrays.

Expressions for σ_{MU} and σ_{CRB} are useful indicators of the bearing error, but accurate estimates of the bearing error do not inform us of the implied error in the velocity magnitude. Oceanographic HF radar processing schemes, such as the SeaSondes, accurately estimate the the radial current speed, but less accurately estimate the bearing to the patch of ocean surface where the radial speed occurs. This property of data from individual HF radars suggests that algorithms used to form the total vector velocities should account for bearing errors. Furthermore, it seems likely that large bearing errors would be associated with large RMS velocity differences, but the velocity differences depend on the current field, and thus may be large or small depending on the spatial variation in the real currents.

The complex currents obtained from ROMS often present the same velocity at more bearings (N), than there are antennas (M), such that often $N \geq M$ (as stated above, MUSIC is limited to identifying $N = M - 1$ bearings). When $N \geq M$ MUSIC is unable to partition the signal and noise subspaces [35, 71], causing a corruption of the noise eigenvector. This causes an increase in the MUSIC DOA errors, errors that appear to be captured by the estimated σ_{MU}. For SeaSondes with $M = 3$, results suggest that σ_{MU}

accurately estimates the errors even when the current field presents $N > 2$.

Systems using larger numbers of antennas, such as phased arrays with $M = 8$ or $M = 16$, would encounter the problem of $N \geq M$ less often. The ability of these systems to resolve more flow complexity when using direction of arrival methods such as MUSIC instead of beam forming has been demonstrated [72]. With a few exceptions (e.g. [56, 73, 13, 74]), systems with $M \geq 8$ typically use beam-forming techniques that negate the possibility of within beamwidth resolution.

The $N \geq M$ situation possibly contributes to the intrinsic noise found in HF radar data, producing a random source of error the DOAs of operational radars [30, 11, 58]. A detailed investigation of the noise properties of WERA HF radar using MUSIC [58], showed that even with outlier removal and tight quality control an inherent noise persists. Alternatively, if $N > M$ seems unlikely for a given ocean current field, errors resulting from the determination of N in the DOA method could also contribute to the apparent random noise.

3.7 Conclusion

We evaluate an analytical approach given by Stoica and Nehorai (1989) [4] for estimating bearing error uncertainties (σ_{MU}) for HF radar ocean currents. By simulating the backscattered signals from a realistic example of the ocean surface currents, we show that σ_{MU} track errors in the DOAs produced by MUSIC. The number of data snapshots (K) required to form a reliable estimate of the covariance matrix as suggested by simulations, is $K \geq 6$. These results confirm published suggestions [4, 50] that σ_{MU} estimates become unreliable for smaller K, and that they are improved for larger values of K. Further results indicate that temporal averages of > 10 uncertainty estimates, for example when merging data to form hourly radial velocities, provide more reliable estimates of the DOA

error. Simulation-based evaluations demonstrate the utility of the σ_{MU} estimates. The analysis also shows improved comparison statistics between radars along an over-water baseline when screening out $\mathbf{v}_r$ with high values σ_{MU}.

Expressions from Stoica and Nehorai (1989) give bearing uncertainty estimates associated with each radial velocity. These estimates enable the mapping of uncertainty, and the calculation of the error covariance among surface current observations. The uncertainty estimates can also be incorporated into total vector calculations. It is expected that the uncertainty estimates will be useful for assimilation of HF radar data into numerical models of ocean circulation. These results along with previous results from the literature cited above support the following for the quantification of uncertainty in the radial velocity components of oceanographic radars:

$$\mathbf{v}_r(r,\theta) = \mathbf{v}_r(r \pm \sigma_r, \theta \pm \sigma_\theta) \pm \sigma_{\mathbf{v}_r}, \tag{3.20}$$

where (3.1) provides an estimate for the range uncertainty σ_r, (3.2) provides an estimate for the bin velocity uncertainty $\sigma_{\mathbf{v}_r}$, and (3.10) provides the estimate for the bearing uncertainty σ_θ when using MUSIC. Errors due to interfering signals, improper determination of the first order region, or imperfect knowledge of the antenna pattern are not quantified by (3.20). Estimating the contribution from these additional components of error is the subject of ongoing work.

Chapter 4

Evaluation of Alternative Direction of Arrival Methods for Oceanographic HF Radars

4.1 Introduction

Drivers of coastal ocean currents such as wind stress, pressure gradients, and buoyancy forcing interact with the coastal boundary resulting in highly variable and spatially complex flows. Observations that capture these flows in space and time would quantify the surface transport of particles or pollutants in spill responses and search and rescue operations. Land based HF radar is the only available observational approach capable of resolving the temporal and spatial scales essential for understanding the dynamics of coastal circulation in a cost effective manner.

Despite their success in many applications, HF radars are limited in their ability to observe complex, small scale flows. For example, a radar installation with 400 m resolution [40, 75], found substantial contribution to the total exchange across the shelf from

highly complex eddies with spatial scales $\sim$ 1 km and mean durations of $\sim$ 5 hours. A more in depth analysis of the eddy dynamics was hampered by the errors of the radar system, which increased by a factor of 2 in areas of increased flow complexity [76]. Furthermore, a high resolution numerical model of the Santa Barbara Channel [66] reveals vast complexity not found in HF radar observations. While HF radar observations are often usefully combined other observational approaches and models in coastal oceanographic studies (e.g. [77, 78]), investigations to quantify and or reduce inherent error in the measurements are warranted [6, 5, 79].

The growth in deployments of oceanographic HF radars in part resulted from advances in signal processing, particularly in direction of arrival (DOA) algorithms. The Multiple Signal Classification (MUSIC) algorithm [23, 24, 25, 27], with its computational efficiency applicable to arbitrary receive antenna arrays, enabled the development of the spatially compact and relatively low cost SeaSonde by CODAR Ocean Sensors, Ltd. The SeaSonde, with its 3-element receive antenna array and a personal computer for data processing, is largely responsible for growth in deployments, constituting the majority of deployed systems [80]. With a few exceptions (e.g. [55, 56, 73, 72]), application of MUSIC in oceanographic contexts has been specific to the SeaSonde, and until recently was protected by U.S. Patent [52]. In the decades since the publication of MUSIC and its application to oceanographic radars, many alternative methods for DOA processing have been developed, each claiming some advantage over MUSIC.

The purpose of this study is to revisit direction finding methods for oceanographic radars, identify improvements in the ocean current data they produce, and better resolve complex flow structures in coastal current systems. We investigate developments from other fields of science and technology in the general the problem of estimating directions of arrivals of signals propagating from remote sources. To evaluate the performance of

DOA algorithms we adopt the simulation based approach (e.g. [3, 41, 53, 17]), with the difference of using complex flows from the high resolution Regional Ocean Modelling System (ROMS; [66]) as the simulation inputs. Simulations allow the direct evaluation of algorithm performance in scenarios closely resembling the planned application, without the confounding factors associated with in situ comparison (e.g.[33, 36, 16]).

The paper is organized as follows. In Section 4.2, we review signal processing methods for oceanographic HF radars. In Section 4.3 we define the two signal models used for simulating signals received by the HF radar. We describe DOA methods used in the study in Section 4.4, review some experimental details in section 4.5, and present the results and conclusions in Sections 4.6, and 4.7 respectively.

4.2 HF Radar Techniques

Prior to discussing the models used to simulate HF radar backscatter, and the DOA methods investigated, we review the relevant signal processing used by oceanographic HF radars. This review generally follows previous discussions specific to the SeaSonde ([52, 54, 42, 79]), but can in theory be applied to arbitrary systems.

A typical HF radar operating in bands near 5, 13, or 24 MHz transmits a frequency modulated signal that couples with the sea surface in ground wave propagation. The signals backscatter from Bragg resonant ocean surface waves [81, 82] with a wavelength $\lambda = \frac{\lambda_{TX}}{2}$, where λ_{TX} is the wavelength of the transmitted radio wave. The ocean surface waves impart a Doppler shift due to the combination of their theoretical speed and that of the radial component of the underlying ocean surface current ($\mathbf{v}_r$). The effective depth of $\mathbf{v}_r$, also related to transmit frequency, ranges from 2.5-0.5 m [83]. Gating or demodulation sorts the signals received on each antenna as a function of range r, with

the range increment (δr) determined by the transmit bandwidth (BW)[84],

$$\delta r = \frac{c}{2BW}, \tag{4.1}$$

given the speed of light $c = 3 \times 10^5$ km s^{-1}. Windowing in the processing produces 15% overlap between range cells for SeaSondes, and up to 50% for other systems (e.g Wellen Radars (WERA))[85]. For a given range, observations from sequential transmit sweeps produce a time series of voltages (c.f. [52]). From the voltage time series we compute FFTs and then form auto- and cross-spectra as the conjugate products [53]. The resulting spectra sort the signal variance by Doppler frequency, revealing peaks near frequencies $f_B = \pm\frac{g}{2\pi\lambda_{TX}}$, where g is the acceleration of gravity, corresponding to the theoretical speed of the approaching and receding Bragg-resonant ocean waves [81]. Spread in the Bragg peaks around f_B results from variation in the underlying radial currents $\mathbf{v}_r$.

SeaSondes typically produce estimates of the Doppler spectra every 256 s, using a 2 Hz sampling rate (SWR) (n_{FFT} =512). The SeaSonde outputs averaged spectra every 10 minutes, combining 3 FFTs which cover a total of 12 min and 48 s. The FFT length sets the frequency bin width, $\delta f = \frac{SWR}{n_{FFT}}$, and from δf we compute the resolution of $\mathbf{v}_r$,

$$\delta \mathbf{v}_r = \frac{\lambda_{TX}\delta f}{2}. \tag{4.2}$$

For a 13 MHz radar with n_{FFT} =512, $\delta \mathbf{v}_r \approx 4$ cm s^{-1}. Longer FFT lengths improve bin resolution to ~ 1 cm s^{-1} [40, 85], particularly when combined with higher $SWR \approx 4$ [58].

Doppler power spectra typically resolve a main peak, centered on f_B for example, containing signal from the first order resonant backscatter, with lower peaks at adjacent frequencies resulting from higher order scattering processes [82]. Only signal from the first order scatter contains ocean current information for DOA processing. SeaSondes

use empirical methods [54] to identify the first order region, though image processing techniques have been adapted [59].

Once identified, for each f in the first order region we form the $M \times M$ covariance matrix $\mathbf{C}(f)$ (e.g.[54, 53]) from bin values of the averaged auto- and cross-spectra, where M is the number of receive antennas. Studies in the signal processing literature typically apply DOA processing to covariance matrices formed directly from the antenna voltage time series [65, 48], rather than to $\mathbf{C}(f)$ from the frequency domain. However, the FFT pre-processing step is crucial when applying DOA algorithms to ocean current radar data. The FFT processing essentially sorts variance by Doppler frequency, and hence velocity, allowing application of DOA processing to individual Doppler velocities. By considering a narrow range of frequencies, we increase the likelihood that the signal emanates from a small fraction of the total azimuth. This step, referred to as narrowband processing [49], decreases the number of simultaneous source bearings.

Determining the number of simultaneous DOAs present in $\mathbf{C}(f)$ constitutes the next step in the processing scheme. After performing the eigendecomposition of $\mathbf{C}(f)$, the SeaSonde uses a hypothesis testing approach [54] to determine if the data results from one or two bearings. Other methods solving the general problem of determining the number of signals (also known as signal detection and model order selection) exist (e.g. [86]) but will not be addressed here. In this study we use the known current input field to determine the number of source DOAs, which we describe in Section 4.5.

DOA processing associates $\mathbf{v}_r$ with direction, producing a polar map of $\mathbf{v}_r = \mathbf{v}_r(r, \theta, t)$ for the time represented by $\mathbf{C}(f)$. SeaSondes commonly produce these maps at 10-minute intervals, averaging together seven maps at hourly intervals. Further processing steps not discussed here combine radial maps from several HF radars to produce the total vector surface current estimates using least squares [8], optimal interpolation [87], or other

techniques [88, 89]. We focus our analysis on the production of $\mathbf{v}_r(r, \theta, t)$, since these form the basic data product of individual HF radars.

4.3 Simulation Signal Models

The simulation of signal backscattered from the ocean surface can be considered a special case of a more general array data model (e.g. [27, 4, 48]). The general model describes the voltages received on the M antennas in terms of the array response $\mathbf{A}$, the signal sources $\mathbf{X}(t)$, and the noise $\mathbf{e}(t)$,

$$\mathbf{Y} = \mathbf{A}\mathbf{X}(t) + \mathbf{e}(t). \tag{4.3}$$

The $M \times N$ matrix $\mathbf{A}$ gives the the response of the M antennas to the N signal sources located at $\theta_1, \theta_2, ..., \theta_N$ as a function of the antenna pattern $\mathbf{a}(\theta_1), \mathbf{a}(\theta_2), ..., \mathbf{a}(\theta_N)$ such that,

$$\mathbf{A} = \begin{bmatrix} | & | & & | \\ \mathbf{a}(\theta_1) & \mathbf{a}(\theta_2) & ... & \mathbf{a}(\theta_N) \\ | & | & & | \end{bmatrix}, \tag{4.4}$$

where $\mathbf{a}(\theta)$ is the $M \times 1$ vector representing the antenna pattern at θ. The $N \times K$ matrix $\mathbf{X}(t)$, where K is the number of independent data samples, or 'snapshots' [65], represents signal from the N sources. After computing the $M \times K$ matrix $\mathbf{Y}$ with (4.3), we compute the $M \times M$ covariance matrix,

$$\mathbf{C} = \frac{1}{K}\mathbf{Y}\mathbf{Y}^H, \tag{4.5}$$

where H denotes the Hermitian conjugate.

We use two implementations of this model as we describe elsewhere [79], the first with a relatively simple $\mathbf{X}(t)$, and the later with $\mathbf{X}(t)$ designed to model backscatter from the

ocean surface. In the simple model we define $\mathbf{X}(t)$ for up to $M-1$ point sources as an $N \times K$ collection of zero mean, normally distributed random numbers [65] with each time step $t = 1, 2, ..., K$ independent,

$$\mathbf{X}(t) = \begin{bmatrix} X_1 & X_2 & \cdots & X_K \end{bmatrix}. \tag{4.6}$$

Investigations with this model remove much of the complexity present in oceanographic HF radar data, while illuminating fundamental performance differences depending only on the receive antenna and the DOA method. Identifying the differences informs the analysis of more complex simulations.

The more complex simulation models signal received by oceanographic HF radars by using (4.3) with $\mathbf{X}(t)$ defined:

$$\mathbf{X}(t) = \mathbf{r}_+ \exp\left(i(\omega_B + \boldsymbol{\omega}_c)t\right) + \mathbf{r}_- \exp\left(i(-\omega_B + \boldsymbol{\omega}_c)t\right), \tag{4.7}$$

where $\mathbf{r}_\pm$ is a decorrelation factor (discussed below), $\pm\omega_B$ the frequency shift due to advancing and receding Bragg waves, and $\boldsymbol{\omega}_c$ is the frequency shift resulting from the ocean currents. In (4.7), the term $\exp\left(i(\pm\omega_B + \boldsymbol{\omega}_c)t\right)$ models the total frequency shift due to the combined effects of the Bragg waves and the currents. Given the radar parameters, we compute $\omega_B = (2k_{TX}g)^{\frac{1}{2}}$ as a function of the radar wave number $k_{TX} = \frac{2\pi f_{TX}}{c}$. We compute $\boldsymbol{\omega}_c = 2k_{TX}\mathbf{v_r}$ from the radial velocity component of the surface current field $\mathbf{v_r}$ obtained from the 100m resolution ROMS for all of the $\mathcal{O}(1 \times 10^4)$ grid points within a range cell. We assume that $\mathbf{v}_r$ is constant in time over all data snapshots. Since $\mathbf{v_r}$ is a function of θ, $\boldsymbol{\omega}_c$ is also: $\boldsymbol{\omega}_c = \boldsymbol{\omega}_c(\theta)$. Thus the dependence of (4.7) on $\mathbf{v}_r$ defines $X(t)$ at all θ in view of the simulated radar.

We include a random factor $\mathbf{r}_\pm$ in (4.7) to decorrelate the signals at an angular

separation that is below the angular resolution of the radar [79]. We construct $\mathbf{r}_\pm$ from $r_\pm$, an $N \times 1$ vector of zero mean random numbers drawn from a normal distribution, such that $\mathbf{r}_\pm = diag(r_\pm)$ is an $N \times N$ matrix. We draw new values for $\mathbf{r}_\pm$ for each data snapshot. $\mathbf{r}_\pm$ models an ocean surface processes that results in uncorrelated HF radar data for angular separations $\mathcal{O}(1^o)$ [67, 8, 3]. Previous simulation-based studies included the effect of wind [3, 41, 53, 17], some using it to decorrelate signals in the way that we use $\mathbf{r}_\pm$ [3, 41]. In order to reduce the experimental complexity we do not model the effect of wind, an assumption that is equivalent to assuming the uniform presence of Bragg waves at all θ.

Using (4.7) in (4.3) produces voltage timeseries that contain the combined signal for the frequencies given by $\pm\omega_B + \boldsymbol{\omega}_c$. Following the processing scheme described above, we form the auto and cross spectra of these timeseries, average K of them together, and populate a covariance matrix $\mathbf{C}(f)$ for each frequency bin separately. $\mathbf{C}(f)$ forms the input to the DOA methods.

4.4 Direction of Arrival Methods

The MUSIC algorithm [23, 24, 25, 27] was a major advance for problems requiring determination of the DOAs of multiple simultaneously incident sources. These problems arise in many branches of science and technology including seismology, astronomy, sonar, bomb detection, personal communications (e.g. cell phones), and biomedical research [35, 61]. MUSIC significantly reduced the computational requirements, enabling real time estimates of DOAs on the computers available at the time. We review the MUSIC algorithm prior to presenting alternative DOA methods and describing their known differences.

Beginning with the data covariance matrix $\mathbf{C}$, the MUSIC algorithm finds the eigen-

decomposition, associating the N largest eigenvalues with the signal and the $M - N$ eigenvalues with the noise. The eigenvectors associated with the signal then form the signal subspace $\mathbf{E}_S$ and those associated with the noise form the noise subspace $\mathbf{E}_N$. From $\mathbf{E}_N$ we compute the MUSIC DOA function P_{MUSIC} for each θ in $\mathbf{A}$ as:

$$P_{MUSIC} = \frac{1}{\mathbf{A}^H \mathbf{E}_N \mathbf{E}_N^H \mathbf{A}}, \tag{4.8}$$

where $\mathbf{A} = [\mathbf{a}(\theta)]$ is $M \times 1$. The DOA solutions are the θ_N found at peak values of (4.8). The advantage of MUSIC is that the search over all θ is 1-D.

Of the many alternative methods for DOA processing, we investigate several for application to oceanographic HF radar based on their reported performance characteristics. These include:

- Weighted MUSIC (W-MUSIC; [90],[35]);
- Maximum Likelihood Estimation by Alternating Projection (MLE-AP; [47]);
- Stochastic Maximum Likelihood (SML; [91]);
- Weighted Subspace Fitting (WSF; [92]).

We describe the methods below.

Weighted MUSIC

For Weighted MUSIC, a weighting matrix $\mathbf{W}$ is introduced into the MUSIC DOA function to modify the relative influence of each of the eigenvectors, with the goal of improving angular resolution without increasing error [35]:

$$P_{W-MUSIC} = \frac{1}{\mathbf{A}^H (\mathbf{E}_N \mathbf{E}_N^H) \mathbf{W} (\mathbf{E}_N \mathbf{E}_N^H) \mathbf{A}}. \tag{4.9}$$

We investigate W-MUSIC with $\mathbf{W}$ defined $\mathbf{W} = \begin{bmatrix}0 & 0 & 1\end{bmatrix}^T \begin{bmatrix}0 & 0 & 1\end{bmatrix}$ (for the 3 element SeaSonde case). With this definition of $\mathbf{W}$, W-MUSIC is known as the Min-Norm method [90]. The Min-Norm version of W-MUSIC exhibits improved performance at low SNR and small samples [35], and better resolution for uniform linear arrays [90].

Maximum Likelihood by Alternating Projection

Maximum likelihood estimation (MLE) methods in general produce the 'optimal' DOA solution, but due to their computational costs are rarely used in practice [61]. In the formulation of [47], MLE-AP seeks the θ_N that maximize:

$$P_{MLE} = \mathrm{Tr}(\mathbf{A}(\mathbf{A}^H\mathbf{A})^{-1}\mathbf{A}^H\mathbf{C}), \tag{4.10}$$

where Tr is the matrix trace operator, and $\mathbf{A}$ is $M \times N$ as in (4.4). The MLE-AP algorithm [47] reduces the costs of computing (4.10) through an efficient search method. Rather than a brute force search of the N-dimensional solution space, the method alternately fixes one parameter (e.g. $\mathbf{a}(\theta_i)$ in $\mathbf{A}$), while maximizing (4.10) for the other (θ_j), until the overall maximum is obtained. As the algorithm steps through θ, rather than compute the projection $\mathbf{A}(\mathbf{A}^H\mathbf{A})^{-1}\mathbf{A}^H$ in (4.10), which includes a matrix inversion, the method uses a projection update formula to further reduce computational cost. The method results in a substantial improvement in computational burden over brute force MLE - though it is still more demanding than MUSIC. This formulation of the maximum likelihood method is also known as the conditional maximum likelihood [49], and the deterministic maximum likelihood [35], which implies specific initial assumptions in the derivation of (4.10) - essentially that the signals are nonrandom but unknown. MLE-AP has been demonstrated to have lower errors and better angular resolution than MUSIC in a variety of scenarios [47, 35, 61].

Stochastic Maximum Likelihood

Derivation of the Stochastic Maximum Likelihood (SML) method starts with a slightly different initial assumption, which is that the signals result from a Gaussian random process. The derivation then results in a cost function that differs from (4.10). Instead the SML method finds the minimum of:

$$P_{SML} = \log(\det(\mathbf{A}(\mathbf{A}^{\dagger}(\mathbf{C} - \sigma\mathbf{I})\mathbf{A}^{\dagger H})\mathbf{A}^{H} + \sigma\mathbf{I})). \tag{4.11}$$

Where σ is defined,

$$\sigma = \frac{1}{M-N}\mathrm{Tr}((\mathbf{I} - \mathbf{A}\mathbf{A}^{\dagger})\mathbf{C}). \tag{4.12}$$

Here $\mathbf{I}$ is the $M \times M$ identity matrix, and $\mathbf{A}^{\dagger}$ is the Moore-Penrose inverse of $\mathbf{A}$. Our implementation of the SML method uses alternating projection search as in (4.10), but requires substantially more computational effort than MLE-AP. Better performance for SML compared to other MLE methods has been observed for scenarios with low SNR or 'small' M [91].

Weighted Subspace Fitting

The WSF method, alternatively known as the Method of Direction Estimation (MODE; [93, 49]), can be interpreted as an MLE method that fits the optimal subspace (e.g. spanned by $\mathbf{A}$) to the signal eigenvectors of $\mathbf{C}$ [49]. Beginning with an estimate of the noise variance from the noise eigenvalues λ_i of $\mathbf{C}$,

$$\sigma = \frac{\sum_{i=N+1}^{M}\lambda_i}{M-N}, \tag{4.13}$$

we compute the optimal weights with the matrix of signal eigenvalues $\mathbf{\Lambda}_S$:

$$\mathbf{W} = (\mathbf{\Lambda}_S - \sigma\mathbf{I})^2 {\mathbf{\Lambda}_S}^{-1}. \tag{4.14}$$

The WSF method then finds the minimum of the function:

$$P_{WSF} = \mathrm{Re}(\log(\mathrm{Tr}((\mathbf{I} - \mathbf{A}\mathbf{A}^\dagger)\mathbf{E}_S\mathbf{W}\mathbf{E}_S^H))). \tag{4.15}$$

Similar performance has been found for WSF when compared to SML, with reduced computational cost [35]. WSF also provides a method for determining the number of signals [92] - a feature not investigated here.

We validated our implementations of the above methods with test scenarios using (4.3), and by reproducing figures from the cited publications. An additional test was formulated based on a detailed example SeaSonde simulation [53]. Results discussed below are also compared with the Cramer-Rao Lower Bound (CRB) [4, 48, 49], which gives the theoretical bound on the accuracy of an estimator based on the characteristics of the receive array, the SNR, the number of data snapshots K, and the assumed number of signal sources N. We compute the CRB using methods detailed in Section 3.4.2 (also [79]).

4.5 Additional Methods

4.5.1 Empirical Signal Detection

An important aspect of the DOA calculation is the determination of the number of signal sources, known as the detection step. Detection methods developed for oceanographic HF radars [54] depend in part on parameters that are specific to MUSIC pro-

cessing, namely the eigenvalues and their ratios. In order to isolate performance aspects of the DOA methods, we remove the detection step by pre-determining the number of signal sources based on the current fields input to the simulation. This step allows us to analyze the performance results due solely to the DOA method, removing any additional performance factors resulting from imperfect signal detection.

When simulation inputs consist of surface currents from ROMS, the 'signal source' often consists of a spatial patch covering a range of bearings. For example, the region in Fig. 4.1 a, defined by $\mathbf{v}_r > 22$ spans bearings between 100^o and 135^o. In this case we specify this entire region as a single source, or $N = 1$. Figs. 4.1 a-f show the radial component of ROMS surface current fields (input $\mathbf{v}_r$), for range cells vs. bearing used in simulations. By inspection of these figures, we determine ranges of $\mathbf{v}_r$ to associate with single bearing ($N = 1$), dual bearing ($N = 2$), three bearing ($N = 3$), or $N > 3$ bearing solutions as identified by the colored regions in the figures. Since simulations described here employ the SeaSonde array with $M = 3$, cases with $N \geq 3$ identify situations where $N = M$ and $N > M$. We use empirical signal detection to specify N in the DOA calculations, and to parse their results in the subsequent analysis.

4.5.2 Calculation of Error Statistics

We evaluate DOA method performance with several statistics, based on the difference between the simulation input at $\hat{\theta}_i$ and the DOA output θ_i for each method. We compute the RMS error σ_{RMS} for n observations as,

$$\sigma_{RMS} = \sqrt{\frac{\sum_{i=1}^{n}(\hat{\theta}_i - \theta_i)^2}{n}}. \tag{4.16}$$

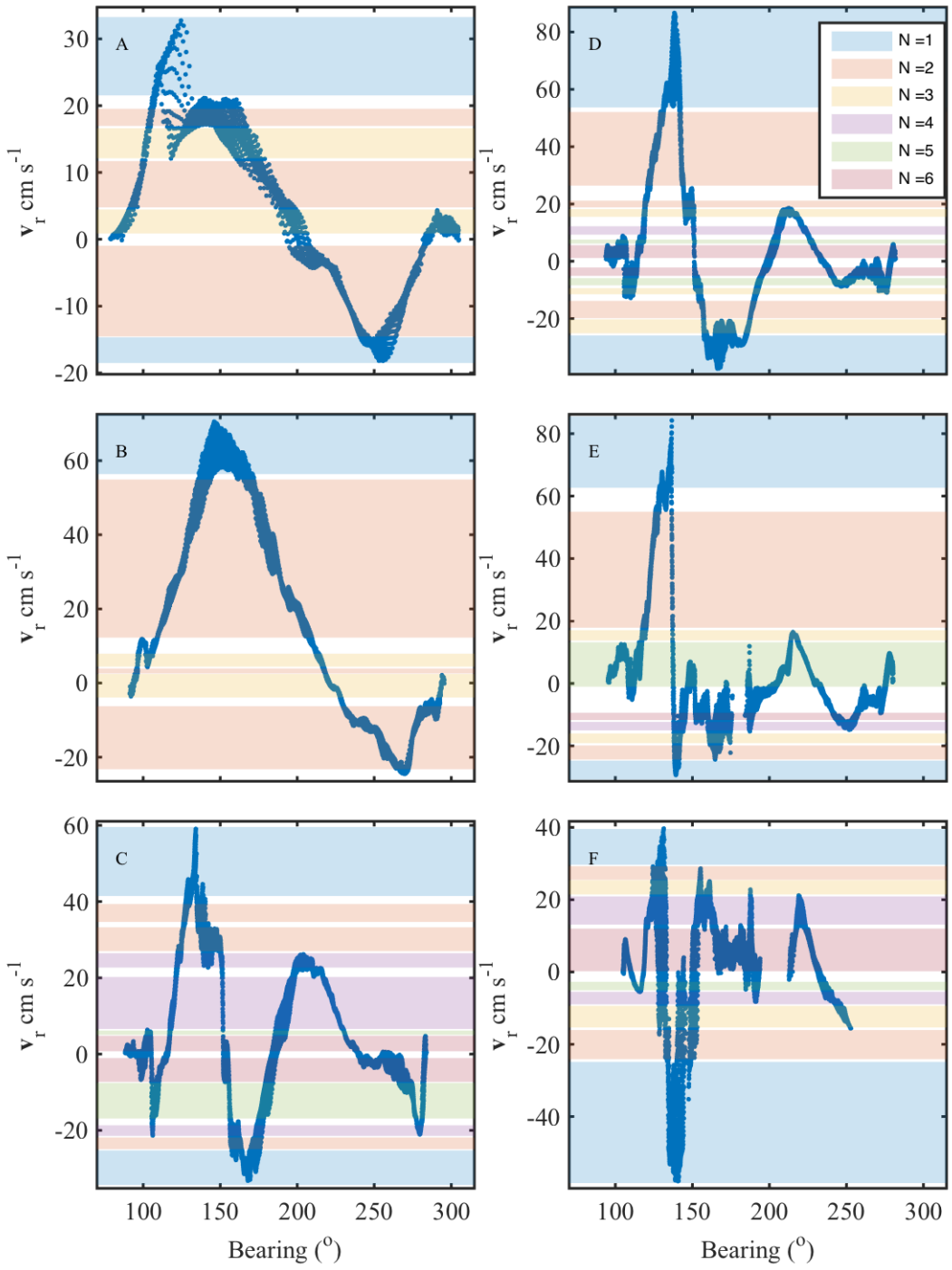

Figure 4.1: Profiles of $\mathbf{v}_r$ from ROMS with counts of source patches (N) shown by colored regions (see legend), for range cells a) 4.0 km, b) 11.5 km, c) 29.5 km, d) 34 km, e) 38.5 km, and f) 53.5 km

Since large values of error disproportionately influence σ_{RMS}, we also show curves based on the median, computed as:

$$\sigma_{MED} = \sqrt{median(\hat{\theta}_i - \theta_i)^2}. \tag{4.17}$$

When simulation inputs consist of surface currents from ROMS, the 'signal source' often consists of a spatial patch covering a range of bearings, and $\hat{\theta}_i$ takes on a range of possible values. In this case, when computing (4.16) and (4.17) we use the value of $\hat{\theta}_i$ that is closest to θ_i.

4.6 Results

4.6.1 Sources at two bearings

Fig. 4.2 shows results of simulations of a test scenario [49] using the signal model in (4.3), with K=100 and two sources 5^o apart. For the uniform linear array (ULA) used in this test scenario, the source spacing is a fraction of the half power beamwidth. Given the array manifold as in (4.4) but at all θ, we compute the half power beamwidth as the range of θ where the antenna power is equal to half the maximum:

$$HPBW = 0.5\left|\frac{1}{M}\mathbf{A_0}^H\mathbf{A}\right|^2, \tag{4.18}$$

where $\mathbf{A_0}$ is the array manifold evaluated at the reference angle θ_0. With $\lambda/2$ spacing between the $M = 10$ array elements, $HPBW = 10.2^o$ [49]. The $HPBW$ approximates the minimum resolution for beam forming methods.

By design the Fig. 4.2 scenario demonstrates differences in performance for the the DOA methods. For MUSIC and W-MUSIC σ_{RMS} increases rapidly as SNR drops below

5 dB. A similar increase in σ_{RMS} occurs for MLE-AP, SML and WSF, but not until SNR drops below -3 dB. Increased σ_{RMS} at a higher SNR for MUSIC when compared to MLE-based methods is referred to as MUSIC-breakdown [94].

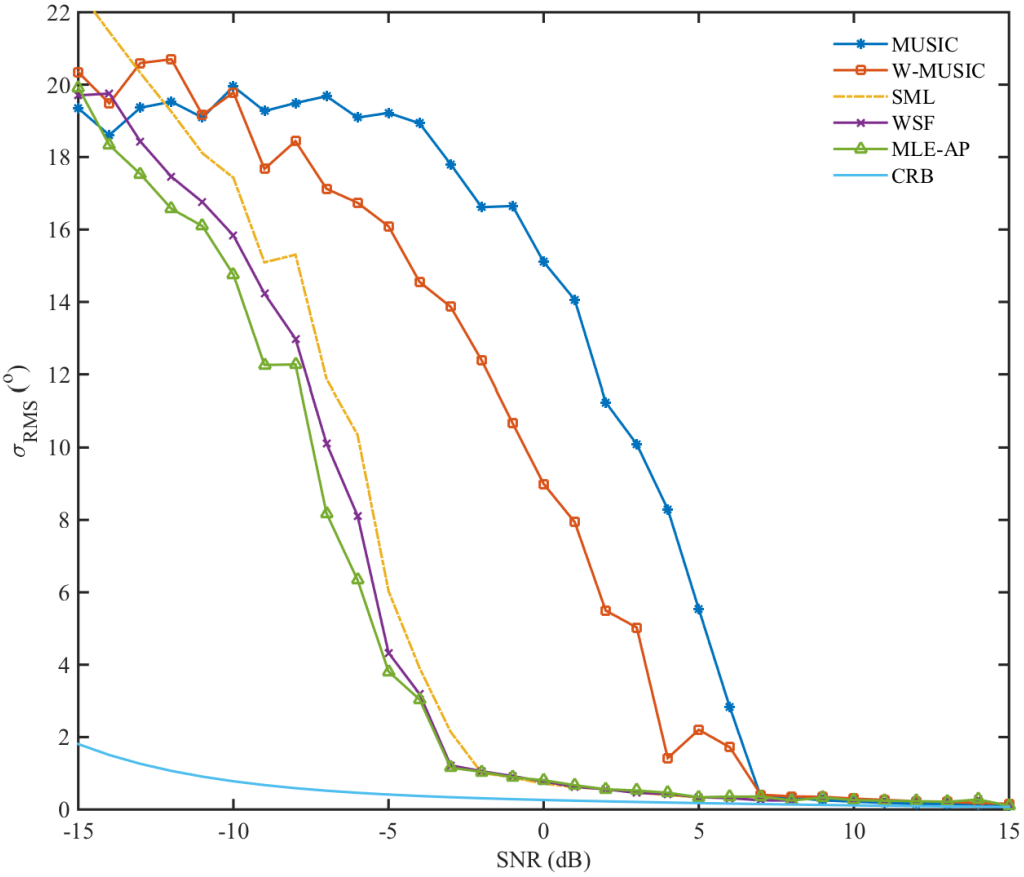

Figure 4.2: σ_{RMS} vs. SNR for the DOA methods, from simulations of two signal sources separated by 5^o, for a 10-element linear array with $K = 100$ as demonstrated in [49]. The CRB is shown for comparison.

MUSIC-breakdown is well known for standard array types [94, 71, 49] but has not been shown for the SeaSonde. Fig. 4.3a shows results of the test scenario with the SeaSonde array, with sources located at 65.5^o separation, or about half the SeaSonde $HPBW$ of 131^o computed with (4.18). MUSIC-breakdown demonstrated for the 10-

element ULA is not observed for the SeaSonde. Instead Fig. 4.3a shows similar σ_{RMS} for all DOA methods, with MLE-AP, SML and WSF showing only slightly lower σ_{RMS} between 5-13 dB SNR. Below 4 dB SNR, σ_{RMS} for all methods becomes larger than half the source separation (or greater than 32^o).

In Fig. 4.3b we plot number of DOA solutions returned, expressed as a percentage of the number returned by MUSIC, or,

$$\% \; n_{MUSIC} = \frac{n}{n_{MUSIC}} * 100. \tag{4.19}$$

Fig. 4.3b shows the primary difference between the methods, with MLE-AP, WSF and SML returning up to 150% of n_{MUSIC}. In simulations with the SeaSonde antenna in this scenario, instead of breakdown, MUSIC and W-MUSIC lose the ability to resolve two sources, returning single DOA solutions even when explicitly searching for two sources. Essentially MUSIC and W-MUSIC fail to detect two solutions as SNR decreases, seeing the two sources as a single source.

Investigations varying source separation, SNR, and K with the SeaSonde array were unable to produce the characteristic MUSIC-breakdown as shown for the 10 element ULA. However the results of these investigations show the influence of changing source separation on performance for the DOA methods with the SeaSonde array. The plot of σ_{RMS} vs. SNR with source separations at 0.3 $HPBW$ (39.3^o) in Fig. 4.4a shows higher overall σ_{RMS} when compared with Fig. 4.3a. The figure shows lower σ_{RMS} for MUSIC and W-MUSIC compared with MLE-AP, WSF and SML for SNR<10 dB. However Fig. 4.4b shows that the lower σ_{RMS} for MUSIC and W-MUSIC results from fewer data returns compared with MLE-AP, WSF, and SML. Between 5-10 dB these methods return more than 140% of n_{MUSIC}. In contrast, Fig. 4.5 shows that with sources at 0.7 $HPBW$ (91.1^o separation), MUSIC and W-MUSIC demonstrate improved

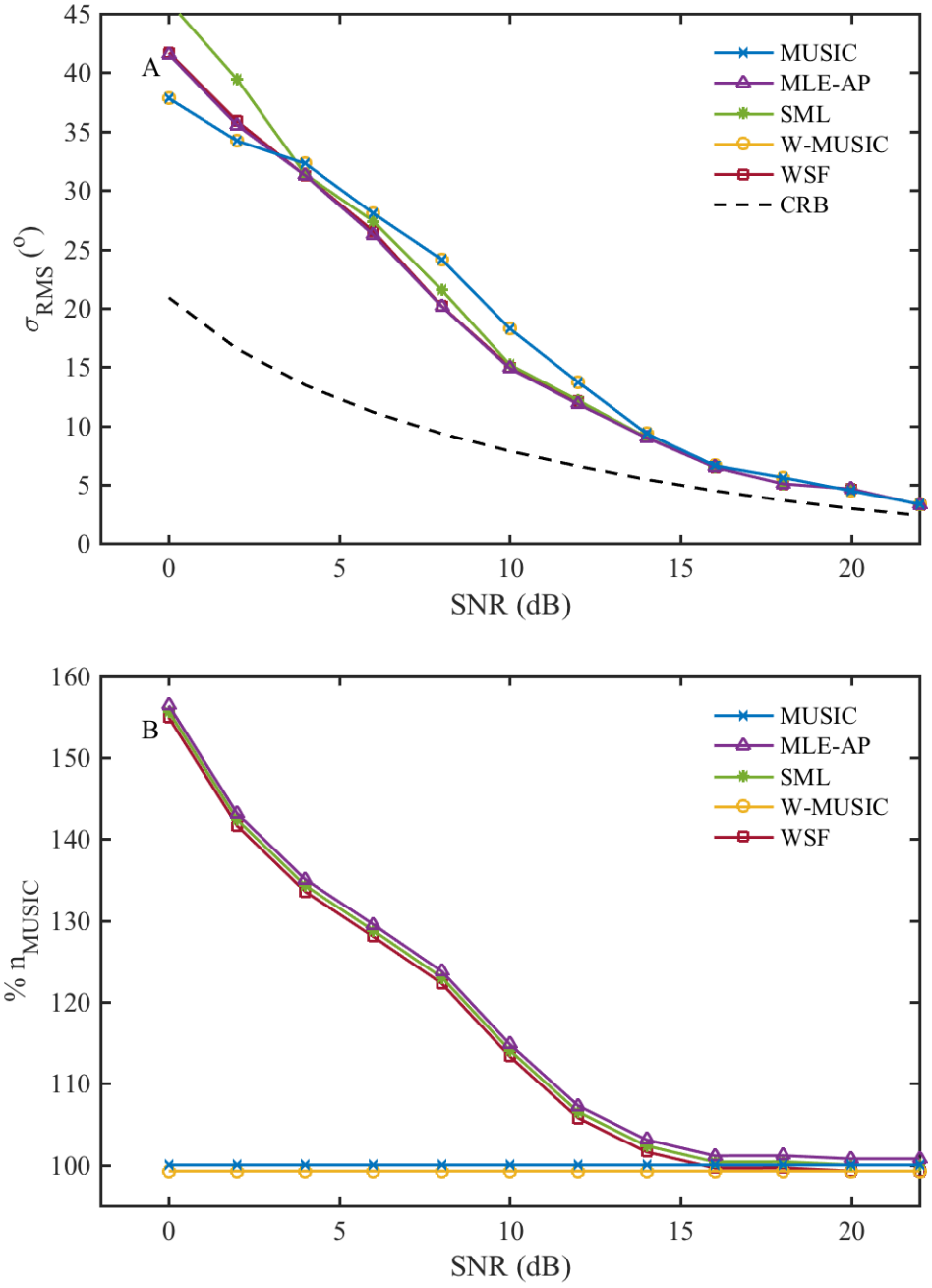

Figure 4.3: a) σ_{RMS} vs. SNR for the DOA methods from simulations of two signal sources separated by 65.5^o, for a 3-element SeaSonde array with $K = 10$. b) The number of DOA solutions returned by each method, expressed at a percentage of the solutions returned by MUSIC (eqn. 4.19). WSF, MLE-AP and W-MUSIC have been slightly offset for clarity.

ability to resolve both sources. Overall as the source spacing increases, the difference in the % n_{MUSIC} diminishes, and σ_{RMS} improves.

Results of the two source simulations aid the interpretation of the results of more complex simulations. The increased DOA returns for MLE-AP, SML and WSF suggest that the use of alternatives to MUSIC could increase HF radar coverage at lower SNR and improve resolution of closely spaced sources. Prior to simulations of ocean backscatter, we look at a slightly more complex case study involving more than two sources.

4.6.2 Sources at M bearings

Preliminary simulations using ROMS for the input velocity field suggest the likelihood of situations with more signal sources (at the same $\mathbf{v}_r$) than antennas, or $N > M$. When using ROMS we define a 'source' as a patch of ocean surface with radial velocities within the bin value of $\mathbf{v_r}$. Considering an individual range cell, if N patches with the same $\mathbf{v_r}$ occur at different bearings, and $N < M$ then we can determine direction to the patch locations (θ_N). If however $N \geq M$ then we can only determine $M - 1$ DOA solutions.

Fig. 4.6 shows σ_{RMS} vs. SNR for simulations with equal power sources located at three bearings, -65^o, 0^o, and 65^o using the SeaSonde array. Elevated σ_{RMS} results from the presence of the third source, with minimum σ_{RMS} near 20^o. With equal spacing between the sources, bias is introduced equally into the two DOA solutions. Further investigations varying the location of the central source suggest that as the central source moves closer to one source, the simulated scenario approaches a two source system, with one DOA solution produced at the mean of the two adjacent sources and the other produced near the third source. Investigations varying the power (SNR) of the central source suggest that the bias generated by this source is moderated by SNR, with its influence diminishing as its SNR approaches the noise level. These investigations demonstrate an

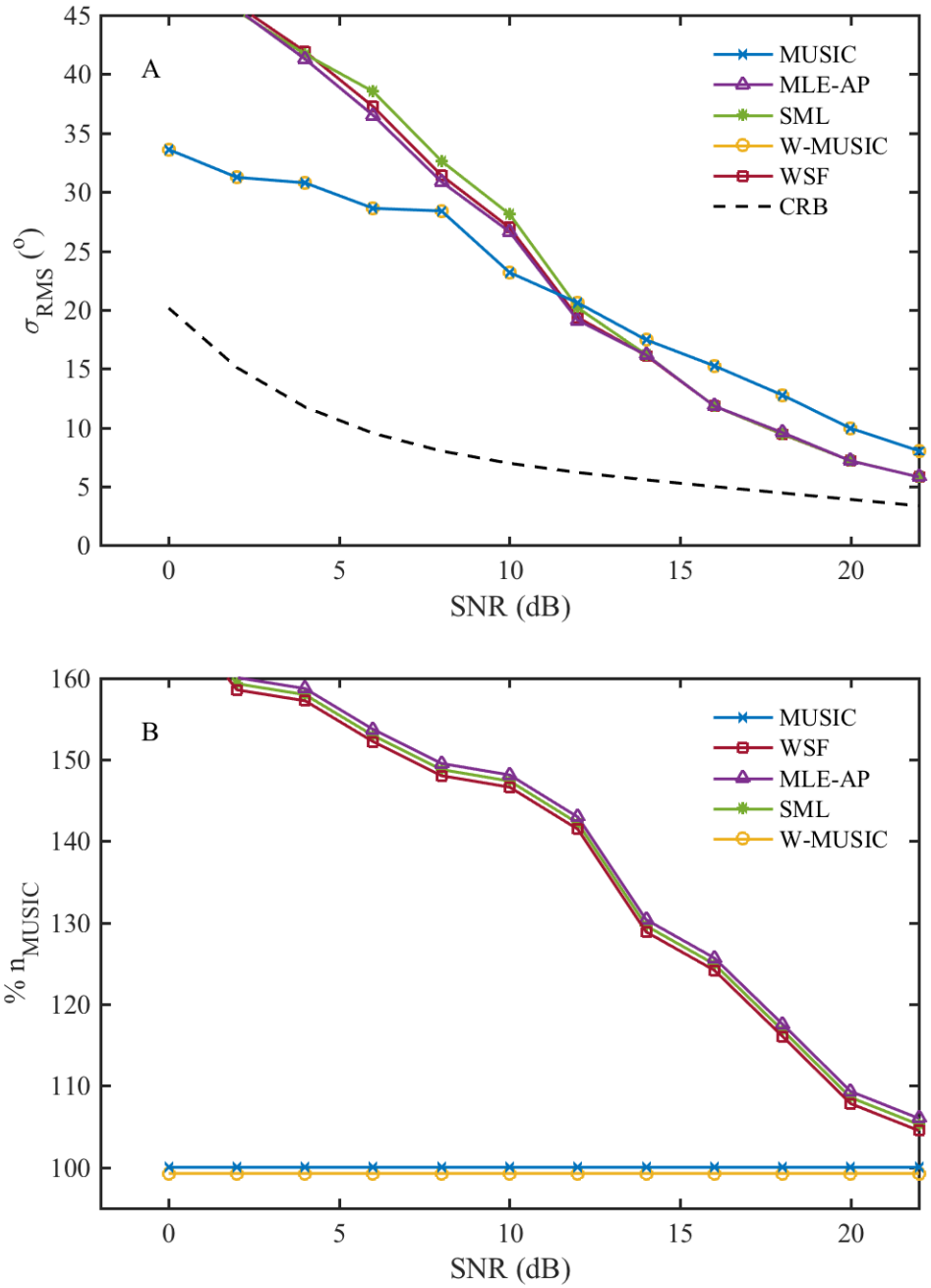

Figure 4.4: As in Fig. 4.3, for sources 52.4^o apart ($0.4\ HPBW$)

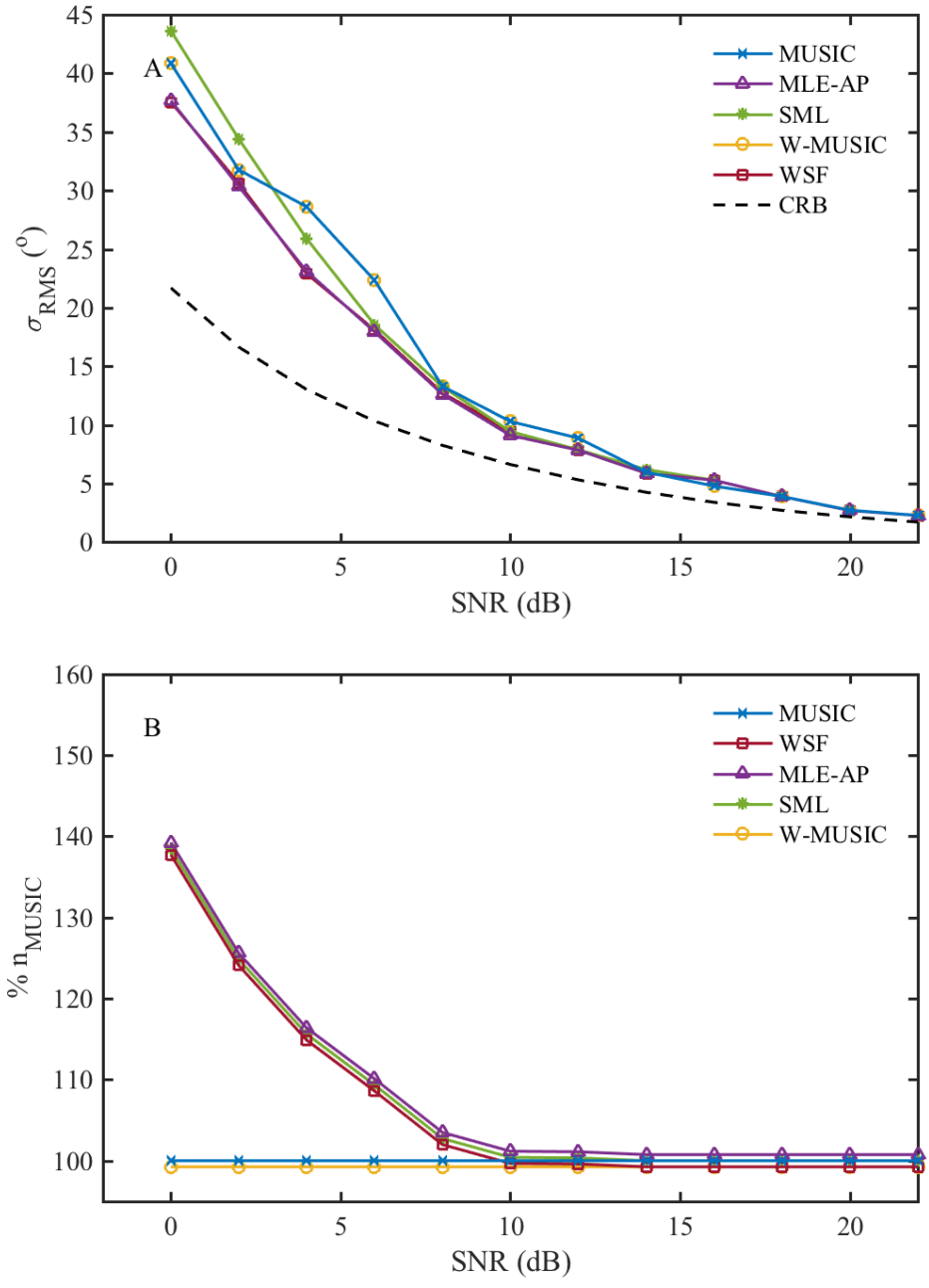

Figure 4.5: As in Fig. 4.3, for sources 78.6^o apart ($0.6\ HPBW$)

influence on the DOA when the assumptions underpinning the DOA methods are violated. In the case of MUSIC and W-MUSIC, essentially the eigen decomposition is unable to separate the signal and noise subspaces, introducing a bias in the noise subspace - a phenomenon known as subspace leakage [35, 61]. Fig. 4.6 shows the performance of the DOA methods when $N = M$. We infer from these figures that in similar scenarios, such as when the ocean surface presents $N \geq 3$ for an $M = 3$ array, the DOA methods will identify the two source locations that are furthest apart, or that have the higher SNR values. We also infer that the resulting DOAs will have higher σ_{RMS}.

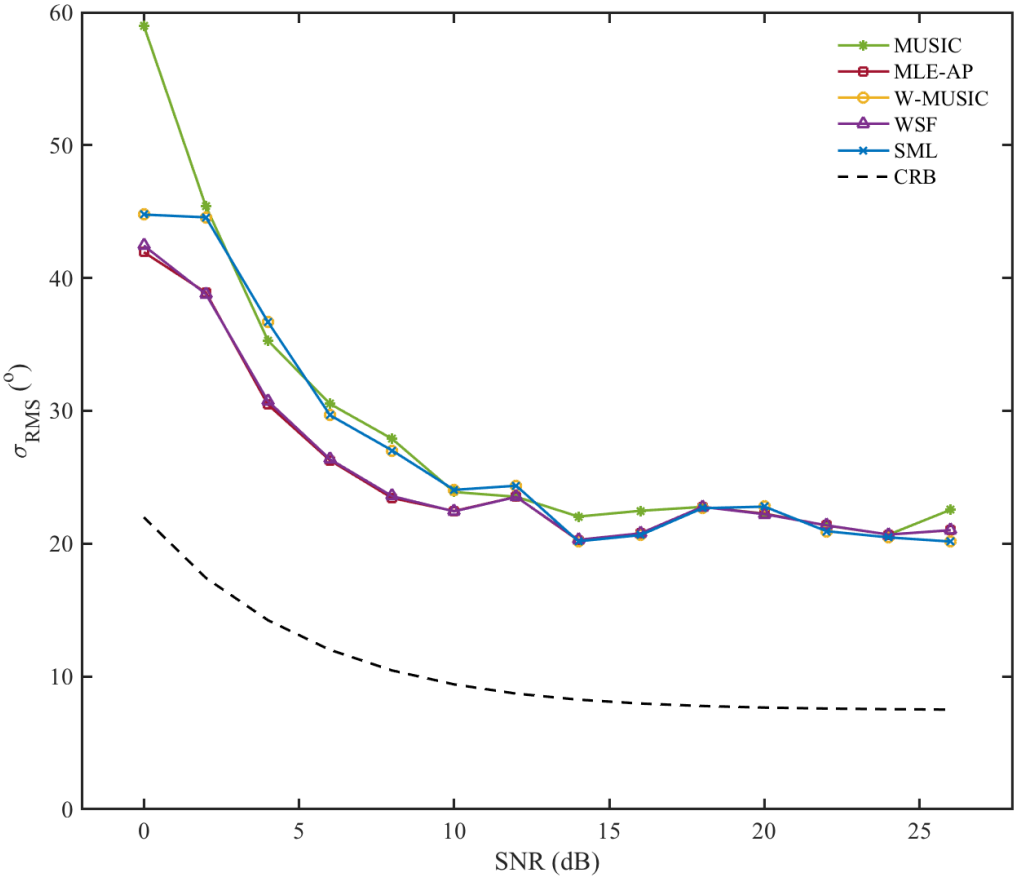

Figure 4.6: σ_{RMS} vs. SNR for the DOA methods from simulations of 3 signal sources at -65^o, 0^o and 65^o, for a 3-element SeaSonde array with $K = 10$.

4.6.3 Sources based on ROMS

Figs. 4.7 a-d show results obtained with the DOA methods when applied to simulations with ROMS inputs shown in Fig. 4.1. We parse the results by the number of signal sources as described above, with Figs. 4.7 showing results: a) for the ROMS surface current fields presenting a single source patch ($N = 1$) at a given $\mathbf{v}_r$; b) source patches at two bearings ($N = 2$); c) source patches at three bearings ($N = 3$); and d) source patches located at more than three bearings ($N > 3$). As quantified by σ_{RMS}, we observer similar performance for MUSIC, MLE-AP, and WSF, with higher σ_{RMS} for SML and W-MUSIC. Fig. 4.7a shows higher σ_{RMS} for W-MUSIC at all SNR, and for SML at SNR between 20-30 dB. The latter appears to result from a cloud of anomalous results that occur near the ends of the APM (data not shown). MLE-AP, MUSIC and WSF, produce similar σ_{RMS} except when SNR < 4 dB, where MLE-AP and WSF produce slightly lower σ_{RMS}. When $N \geq 2$ (Fig. 4.7 b-d), MLE-AP, WSF, MUSIC and W-MUSIC all produce similar σ_{RMS}. In each of the Figs. 4.7 a-c, σ_{RMS} increases with increasing complexity of the flow field, as suggested by the simulations in sections 4.6.1 and 4.6.2 above. In Fig. 4.7d the decreased σ_{RMS} results when the distance between $\hat{\theta}_i$ presented by the flow field and θ_i obtained by the DOA method is never large due to the presence of many possible values of $\hat{\theta}_i$ given by the complex flow field (see Fig. 4.1f for $0 < \mathbf{v}_r < 10$ cm s $^{-1}$ for example).

The curves of σ_{MED} (Figs. 4.8 a-d) show similar shapes as the curves of σ_{RMS} but with lower values overall. The curves for SML show a decreased sensitivity to outliers, indicating similar performance from that method compared to the others when outliers are accounted for. When gauged by σ_{MED} and σ_{RMS}, we find nearly identical, performance for MLE-AP, MUSIC and WSF, all with superior performance relative to W-MUSIC and SML.

In contrast, Figs. 4.9 a-d indicate that the advantages in data returns identified

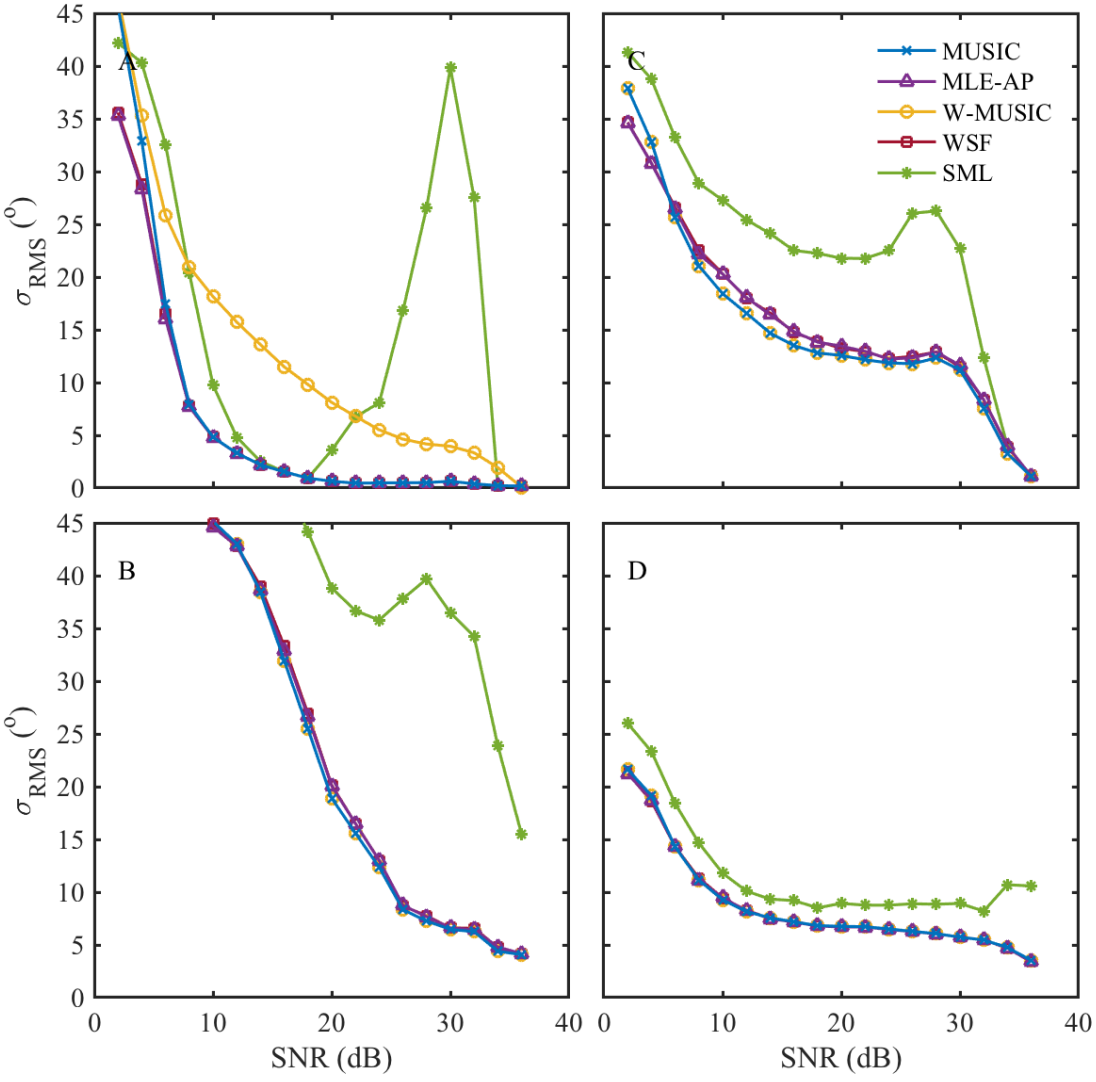

Figure 4.7: σ_{RMS} vs SNR for ROMS radial velocities in Fig. 4.1

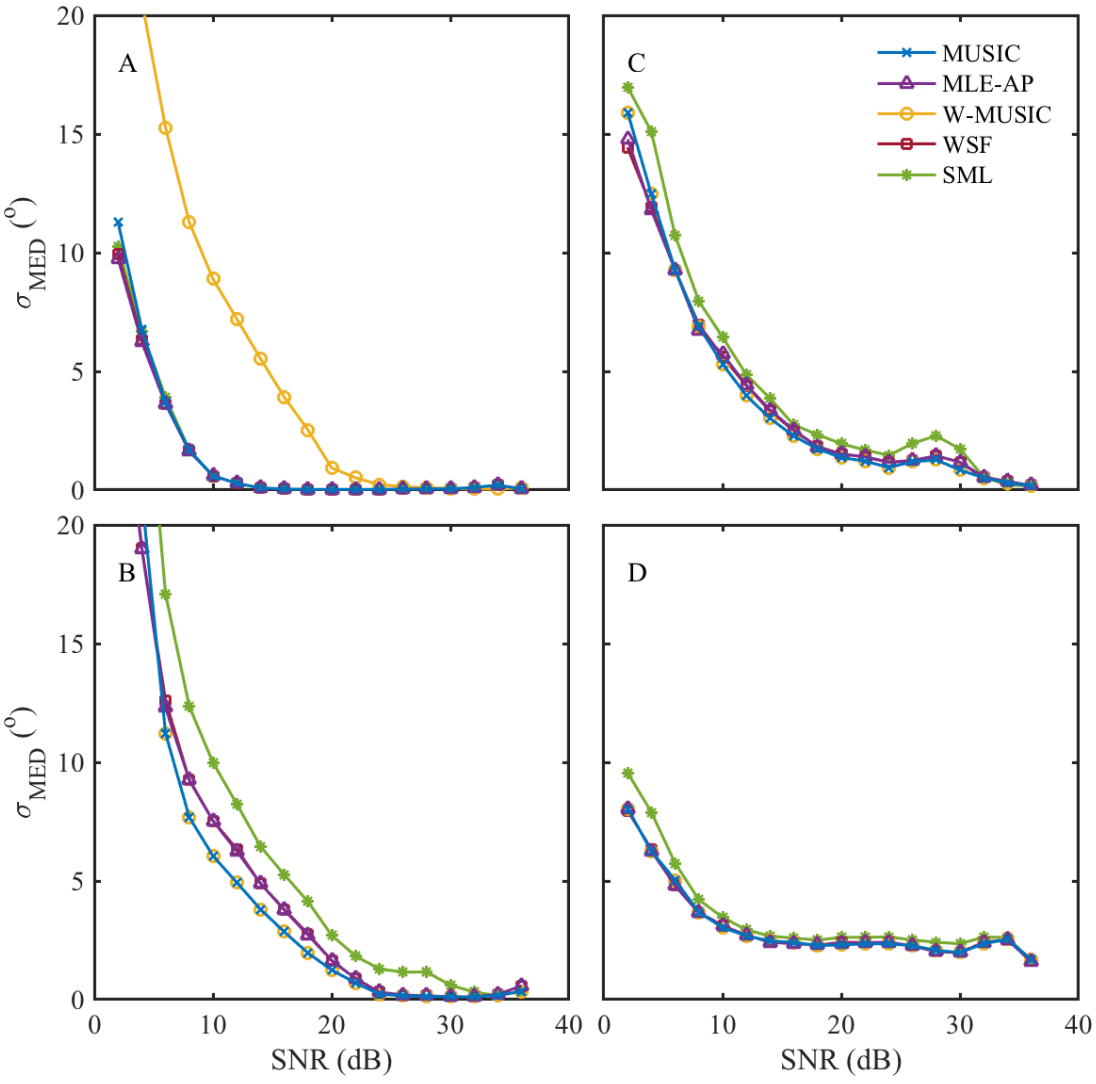

Figure 4.8: σ_{MED} vs SNR for ROMS radial velocities in Fig. 4.1

above also occur in the simulations with ROMS. Figs. 4.9 a-d show the number of DOA solutions in each 2 dB SNR bin as a percentage of the number returned by MUSIC, $\%n_{MUSIC}$ as in (4.19), again parsing the results by the number of source patches. In the $N = 2$ case (Fig. 4.9b, MLE-AP produces 120% of n_{MUSIC} between 10-28 dB, with up to 130% obtained at 6 dB. Fig. 4.9c shows results for $N = 3$, with MLE-AP producing up to 110% of n_{MUSIC}.

Fig. 4.9 shows an improvement in the number of DOA solutions returned when using MLE-AP, WSF and SML compared with MUSIC. Based on these figures we would expect superior performance from MLE-AP at low SNR, and in situations when the flow field presents $N \geq 2$. Since SNR decreases with range for oceanographic HF radars, we would expect $\%n_{MUSIC}$ for MLE-AP, WSF and SML to increase with range. To simulate this scenario we used all ROMS range cells, running 400 simulations each, with the maximum SNR set as a decreasing function of range. We use empirical signal detection as described above, to identify $\mathbf{v}_r$ with $N = 1$ and $N = 2$. Fig. 4.10 summarizes the results, showing $\%n_{MUSIC}$ for the DOA methods. We observe significant variability in $\%n_{MUSIC}$ with range, but as expected MLE-AP, WSF and SML produce up to 130% of n_{MUSIC} with the greatest increase occurring at the greatest range.

4.6.4 Computational cost

Table 4.1 summarizes the computational costs for the DOA methods, as the normalized total time relative to MUSIC. To produce Table 4.1, we logged run times for each of the methods over the 8600 simulations with ROMS. Results demonstrate a substantial computational advantage for MUSIC (and W-MUSIC), approximately a factor of 10, compared to MLE-AP. SML and WSF require considerably more computational time. Our implementation of MLE-AP uses the projection update formula [47], which signifi-

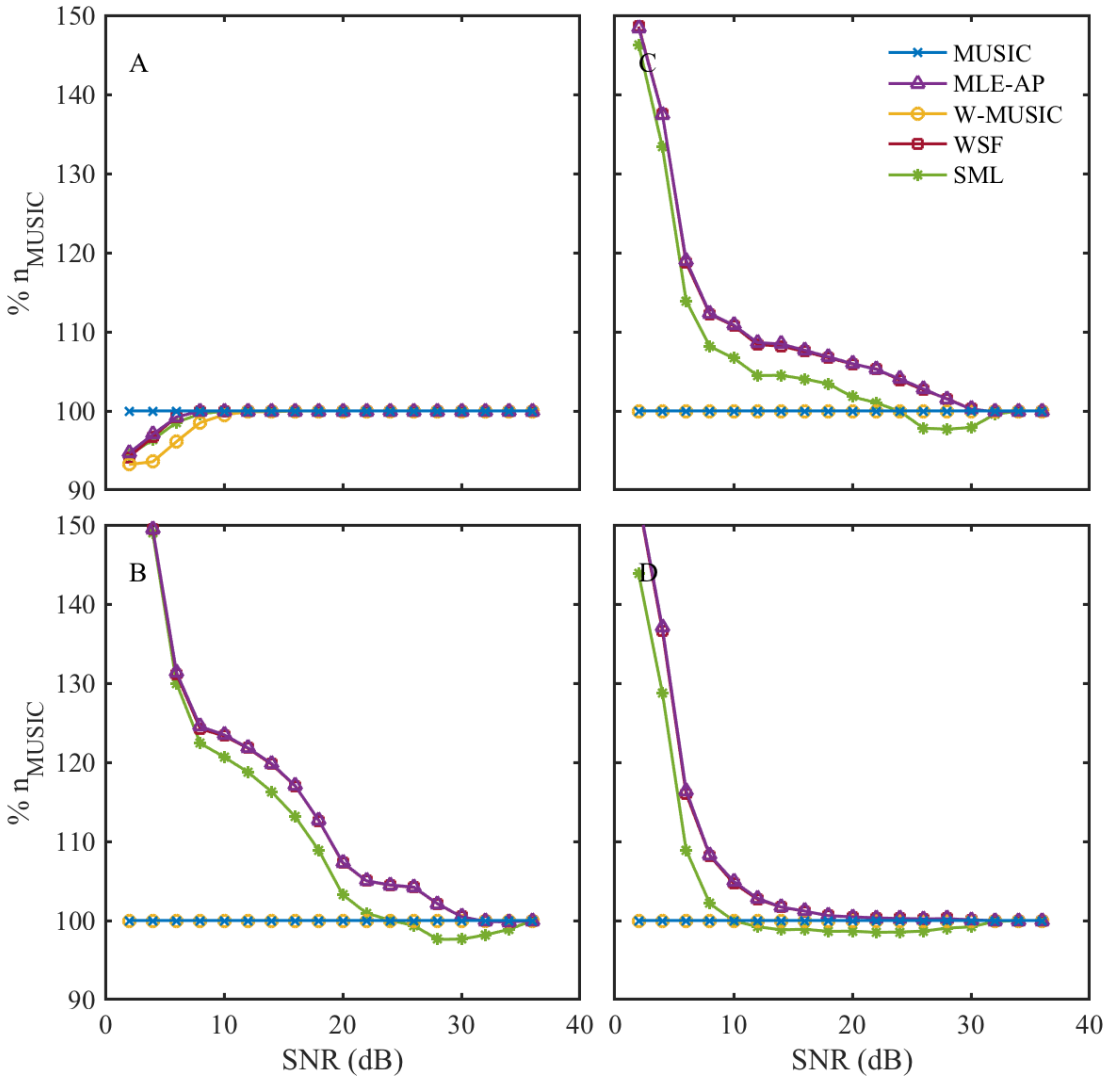

Figure 4.9: Percent of MUSIC solutions vs. SNR for ROMS radial velocities in Fig. 4.1

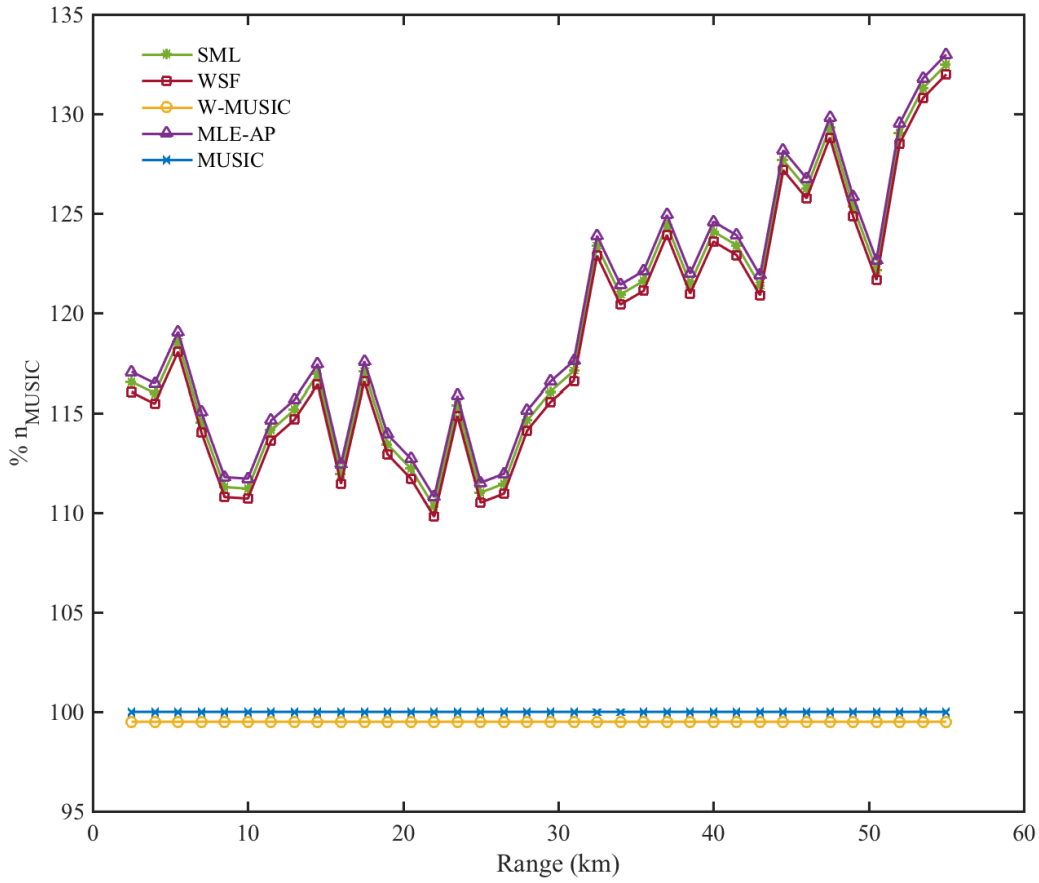

Figure 4.10: The number of DOA solutions returned by each method, expressed at a percentage of the solutions returned by MUSIC, for all ROMS range cells. WSF, MLE-AP and W-MUSIC have been slightly offset for clarity.

cantly decreases the computational demands relative to SML and WSF, both of which use the alternating projection search described for MLE-AP [47].

DOA Method	t/t_{MUSIC}
MUSIC	1.0
W-MUSIC	1.3
MLE-AP	12.8
WSF	36.5
SML	42.5

Table 4.1: Computational times relative to MUSIC for 8600 simulation runs.

4.7 Conclusion

Simulations of oceanographic HF radars using ROMS surface currents as input provide a complex and demanding test of DOA methods. Findings here suggest improved performance from MLE-AP compared to MUSIC in terms of the number of DOAs returned, particularly in situations when signals arrive from two or more bearing, with SNR < 20 dB. These improvements come with similar accuracy, though at higher computational cost. Increased DOA returns may improve maps produced by oceanographic radars by reducing gaps and improving the sample sizes on which the averaged maps are based.

While differences between the methods were demonstrated by the simulation-based evaluations, further work may be required for these gains to translate to operational systems. To some extent, DOA methods work in conjunction with methods to identify the number of signal sources generating the data. Present 'detection methods' as they are known in the literature, work closely with the MUSIC algorithm (such as for the SeaSonde [54]) and would not be appropriate for other DOA methods. Also, empirical detection methods used here may perform better than operational detection methods,

such that the improved data returns we observe for MLE-AP, SML and WSF would be lost with imperfect signal detection.

Another possible influence on the results is the validity of our assumptions about the use of wind in the radar simulations. Our simulations assume no wind, equivalently assuming ubiquitous Bragg waves. As a consequence of this assumption, along with the complex surface current fields from ROMS, our simulations often result in more simultaneous signal sources than there are antennas ($N \geq M$). Adding the effect of wind to the simulation, while adding experimental complexity, would likely reduce the number of simultaneous signal sources by creating sectors of bearing with high SNR. Our assumptions about wind may explain the high fraction of 'dual bearing' ($N \geq 2$) MUSIC DOA solutions observed in the simulation data. The simulations produce about 78% dual bearing solutions for MUSIC, compared with publish values of $< 50\%$ [54], and $20 - 30\%$ obtained from our operational radars.

Future work aims to extend this analysis to other array types, to apply the MLE-AP method to observational data, and to identify other improvements to the signal processing methods. By reviewing advances in DOA and signal processing methods, and evaluating these with demanding, realistic simulations, we hope to enable better ocean current data and improved understanding of the coastal ocean.

Bibliography

[1] B. M. Emery, L. Washburn, C. Whelan, D. Barrick, and J. Harlan, *Measuring antenna patterns for ocean surface current hf radars with ships of opportunity*, *Journal of Atmospheric and Oceanic Technology* **31** (2014), no. 7 1564–1582.

[2] B. M. Emery and L. Washburn, *Improved direction of arrival methods for oceanographic hf radars*, in *Antenna Measurements & Applications (CAMA), 2016 IEEE Conference on*, (Syracuse, NY), pp. 1–4, IEEE, 2016.

[3] D. E. Barrick and B. J. Lipa, *Comparison of direction-finding and beam-forming in HF radar ocean surface current mapping*, *Phase 1 SBIR Final Report, Contract 50-DKNA-5-00092. National Oceanic and Atmospheric Administration* (1996), no. Rockville, MD, 81 pp.

[4] P. Stoica and A. Nehorai, *Music, Maximum Likelihood, And Cramer-Rao Bound*, *IEEE Transactions on Acoustics, Speech, and Signal Processing* **37** (1989), no. 5 720–741.

[5] J. O'Donnell, D. Ullman, M. Spaulding, E. Howlett, T. Fake, P. Hall, T. Isaji, C. Edwards, E. Anderson, T. McClay, J. Kohut, A. Allen, S. Lester, C. Turner, and M. Lewandowski, *Integration of Coastal Ocean Dynamics Application Radar (CODAR) and Short-Term Predictive System (STPS) Surface Current Estimates into the Search and Rescue Optimal Planning System (SAROPS)*, tech. rep., National Technical Information Service, Springfield, VA 22161, Washington, DC 20593-0001, 2005.

[6] P. R. Oke, J. S. Allen, R. N. Miller, G. D. Egbert, and P. M. Kosro, *Assimilation of surface velocity data into a primitive equation coastal ocean model*, *Journal of Geophysical Research* **107** (2002), no. C9 1–25.

[7] D. E. Barrick, *Accuracy of Parameter Extraction from Sample-Averaged Sea-Echo Doppler Spectra*, *IEEE Transactions on Antennas and Propagation* **28** (1980), no. 1 1–11.

[8] B. J. Lipa and D. E. Barrick, *Least-squares methods for the extraction of surface currents from CODAR crossed-loop data: Application at ARSLOE*, *IEEE J. Oceanic Eng.* **8** (1983) 226–253.

[9] D. E. Barrick and B. J. Lipa, *Using antenna patterns to improve the quality of SeaSonde HF radar surface current maps*, in *IEEE Sixth Working Conference on Current Measurement*, pp. 5–8, 1999.

[10] J. T. Kohut and S. M. Glenn, *Improving HF radar surface current measurements with measured antenna beam patterns*, *Journal of Atmospheric and Oceanic Technology* **20** (2003), no. 9 1303–1316.

[11] J. D. Paduan, K. C. Kim, M. S. Cook, and F. P. Chavez, *Calibration and validation of direction-finding high-frequency radar ocean surface current observations*, *IEEE Journal of Oceanic Engineering* **31, 4** (2006) 862–875.

[12] T. Cook, L. Hazard, M. Otero, and B. Zelenke, *Deployment and maintenance of a high-frequency radar for ocean surface current mapping: Best practices*, *Coastal Observing Research and Development Center* (2008).

[13] A. Molcard, P. M. Poulain, P. Forget, A. Griffa, Y. Barbin, J. Gaggelli, J. C. De Maistre, and M. Rixen, *Comparison between VHF radar observations and data from drifter clusters in the Gulf of La Spezia (Mediterranean Sea)*, *Journal of Marine Systems* **78** (2009), no. SUPPL. 1 S79–S89.

[14] D. E. Barrick, B. J. Lipa, P. M. Lilleboe, and J. Isaacson, *Gated fmcw df radar and signal processing for range/doppler/angle determination*, 1994. U.S. Patent 5,361,072.

[15] D. Barrick and B. Lipa, *Correcting for distorted antenna patterns in CODAR ocean surface measurements*, *IEEE Journal of Oceanic Engineering* **11** (1986), no. 2.

[16] H. C. Graber, B. K. Haus, R. D. Chapman, and L. K. Shay, *HF radar comparisons with moored estimates of current speed and direction: Expected differences and implications*, *Journal of Geophysical Research* **102** (1997), no. C8 18749.

[17] K. Laws, J. D. Paduan, and J. Vesecky, *Estimation and assessment of errors related to antenna pattern distortion in CODAR SeaSonde high-frequency radar ocean current measurements*, *Journal of Atmospheric and Oceanic Technology* **27** (2010), no. 6 1029–1043.

[18] D. M. Fernandez, J. F. Vesecky, and C. C. Teague, *Calibration of HF radar systems with ships of opportunity*, *Geoscience and Remote Sensing Symposium, 2003. IGARSS '03. Proceedings. 2003 IEEE International* **7** (2003), no. C 4271–4273 vol.7.

[19] D. M. Fernandez, J. F. Vesecky, and C. Teague, *Phase Corrections of Small-Loop HF Radar System Receive Arrays With Ships of Opportunity*, *IEEE Journal of Oceanic Engineering* **31** (2006), no. 4 919–921.

[20] X. Flores-vidal, P. Flament, R. Durazo, C. Chavanne, and K. W. Gurgel, *High-frequency radars: Beamforming calibrations using ships as reflectors*, *Journal of Atmospheric and Oceanic Technology* **30** (2013), no. 3 638–648.

[21] B. J. Tetreault, *Use of the Automatic Identification System (AIS) for Maritime Domain Awareness (MDA)*, *Proceedings of MTS/IEEE OCEANS, 2005* **2005** (2005).

[22] Centro de Observação Astronómica no Algarve, "ShipPlotter (v. 11.1.2)." `http://www.shipplotter.com.`, 2012.

[23] R. O. Schmidt, *Multiple Emitter Location and Signal Parameter Estimation*, in *Proc. RADC Spectrum Estimation Workshopo*, (Griffiths AFB, Rome, New York), pp. 243–258, 1979.

[24] G. Bienvenu and L. Kopp, *Adaptivity to background noise spatial coherence for high resolution passive methods*, *ICASSP '80. IEEE International Conference on Acoustics, Speech, and Signal Processing* **5** (1980), no. 1 307–310.

[25] R. O. Schmidt, *A signal subspace approach to multiple emitter location and spectral estimation*, *PhD thesis, Stanford University, California. Schmidt, R* **34** (1981), no. 3 276–280.

[26] G. Bienvenu and L. Kopp, *Optimality of high resolution array processing using the eigensystem approach*, *IEEE Transactions on acoustics, speech, and signal processing* **31** (1983), no. 5 1235–1284.

[27] R. Schmidt, *Multiple emitter location and signal parameter estimation*, *IEEE Transactions on Antennas and Propagation* **34** (1986), no. 3 276–280.

[28] G. Strang, *Linear algebra and its applications, 3rd ed.*, .

[29] A. Long and D. Trizina, *Mapping of North Atlantic Winds by HF Radar Sea Backscatter Interpolation*, *IEEE Transactions on Antennas and Propagation* **AP-21** (1973), no. 5 680–685.

[30] B. Emery, L. Washburn, and J. Harlan, *Evaluating radial current measurements from CODAR high-frequency radars with moored current meters*, *Journal of Atmospheric and Oceanic Technology* **21** (2004), no. 8.

[31] D. Barrick, *Bearing accuracy against hard targets with SeaSonde DF antennas*, tech. rep., CODAR Ocean Sensors, Los Altos, CA, 2003.

[32] H. J. Roarty, D. E. Barrick, J. T. Kohut, and S. M. Glenn, *Dual-use of compact HF radars for the detection of mid and large-size vessels*, *Turkish Journal of Electrical Engineering and Computer Sciences* **18** (2010), no. 3 373–388.

[33] R. Chapman, L. Shay, H. Graber, J. Edson, A. Karachintsev, C. Trump, and D. Ross, *On the accuracy of HF radar surface current measurements: Intercomparisons with ship-based sensors*, *Journal of Geophysical Research* **102** (1997), no. C8 18737.

[34] K. W. Gurgel, G. Antonischki, H. H. Essen, and T. Schlick, *Wellen Radar (WERA): A new ground-wave HF radar for ocean remote sensing*, *Coastal Engineering* **37** (1999), no. 3-4 219–234.

[35] H. Krim and M. Viberg, *Two decades of array signal processing research: the parametric approach*, *IEEE Signal Processing Magazine* **13** (1996) 67–94.

[36] R. D. Chapman and H. C. Graber, *Validation of HF radar measurements*, *Oceanography* **10** (1997), no. 2 76–79.

[37] H. H. Essen, K. W. Gurgel, and T. Schlick, *On the accuracy of current measurements by means of HF radar*, *IEEE Journal of Oceanic Engineering* **25** (2000), no. 4 472–480.

[38] S. Cosoli, A. Mazzoldi, and M. Gačić, *Validation of surface current measurements in the northern Adriatic Sea from high-frequency radars*, *Journal of Atmospheric and Oceanic Technology* **27** (2010), no. 5 908–919.

[39] C. Ohlmann, P. White, L. Washburn, E. Terrill, B. Emery, and M. Otero, *Interpretation of coastal HF radar-derived surface currents with high-resolution drifter data*, *Journal of Atmospheric and Oceanic Technology* **24** (2007), no. 4.

[40] A. R. Kirincich, T. De Paolo, and E. Terrill, *Improving HF radar estimates of surface currents using signal quality metrics, with application to the MVCO high-resolution radar system*, *Journal of Atmospheric and Oceanic Technology* **29** (2012), no. 9 1377–1390.

[41] K. E. Laws, D. M. Fernandez, and J. D. Paduan, *Simulation-based evaluations of HF radar ocean current algorithms*, *IEEE Journal of Oceanic Engineering* **25** (2000), no. 4 481–491.

[42] T. de Paolo and E. Terrill, *Skill assessment of resolving ocean surface current structure using compact-antenna-style HF radar and the MUSIC direction-finding algorithm*, *Journal of Atmospheric and Oceanic Technology* **24** (2007), no. 7 1277–1300.

[43] T. Cook, T. DePaolo, and E. Terrill, *Estimates of radial current error from high frequency radar using music for bearing determination*, in *OCEANS 2007*, pp. 1–6, IEEE, 2007.

[44] D. Barrick. personal communication.

[45] B. J. Lipa, *Uncertainties in SeaSonde current velocities*, *Current Measurement Technology, 2003. Proceedings of the IEEE/OES Seventh Working Conference on* (2003) 95–100.

[46] S. Cosoli, G. Bolzon, and A. Mazzoldi, *A real-time and offline quality control methodology for seasonde high-frequency radar currents*, *Journal of Atmospheric and Oceanic Technology* **29** (2012), no. 9 1313–1328.

[47] I. Ziskind and M. Wax, *Maximum Likelihood Localization of Multiple Sources by Alternating Projection*, *IEEE Transactions on Acoustics, Speech, and Signal Processing* **36** (1988), no. 10 1553–1560.

[48] B. Friedlander, *Wireless Direction-Finding Fundamentals*, in *Classical and Modern Direction-of-Arrival Estimation* (T. E. Tuncer and B. Friedlander, eds.), ch. 1, pp. 1–49. Elsevier, 2009.

[49] H. L. Van Trees, *Optimum array processing: Part IV of detection, estimation and modulation theory*, vol. Part IV. Wiley Online Library, 2002.

[50] X.-L. Xu and K. M. Buckley, *Statistical Performance analysis of the MUSIC location estimator*, *IEEE Trans. Signal Processing* **40** (1992), no. 10.

[51] P. Forster, *Methodes de traitenient d'antenne apres filtrage spatial*. Ph.d. dissertation, Universite de Rennes, France, 1988.

[52] D. E. Barrick and B. J. Lipa, *Radar angle determination with music direction finding*, Nov. 23, 1999. U.S. Patent 5,990,834.

[53] T. de Paolo, T. Cook, and E. Terrill, *Properties of hf radar compact antenna arrays and their effect on the music algorithm*, in *OCEANS 2007*, pp. 1–10, IEEE, 2007.

[54] B. Lipa, B. Nyden, D. S. Ullman, and E. Terrill, *SeaSonde radial velocities: Derivation and internal consistency*, *IEEE Journal of Oceanic Engineering* **31** (2006), no. 4 850–861.

[55] P. Broche, Y. Barbin, D. J. Maistre, P. Forget, and J. Gaggelli, *Antennas processing and design for VHF COSMER coastal radar*, in *ROW-4 Radiowave Oceanography Workshop*, (Townsville, Australia, April 21-23), 2004.

[56] Y. Barbin, P. Broche, J. de Maistre, P. Forget, and J. Gaggelli, *Practical results of Direction Finding method applied on a 4 antenna linear array WERA*, in *ROW-6 Radiowave Oceanography Workshop, May 1518.*, (Hamburg, Germany), 2006.

[57] J. S. Bendat and A. G. Piersol, *Random data: analysis and measurement procedures*, .

[58] P. Forget, *Noise properties of HF radar measurement of ocean surface currents*, *Radio Science* **50** (2015), no. 8 764–777.

[59] A. R. Kirincich, *Improved detection of the first-order region for direction-finding HF radars using image processing techniques*, *Journal of Atmospheric and Oceanic Technology* **34** (2017), no. 8 1679–1691.

[60] CODAR Technical Manual, *Defining first order region boundaries*, tech. rep., CODAR Ocean Sensors, Ltd., Los Altos, CA, 2002.

[61] E. Tuncer and B. Friedlander, *Classical and modern direction-of-arrival estimation*. Academic Press, 2009.

[62] B. M. Emery and L. Washburn, *Evaluation of Alternative Direction of Arrival Methods for Oceanographic HF Radars*, .

[63] P. Stoica, A. Eriksson, T. Beron, and K. D. Ward, *DOA estimation method for unknown noise fields*, *IEE Proceedings Radar, Sonar and Navigation* **141** (1994), no. 3 149–150.

[64] D. M. Fernandez and J. D. Paduan, *Simultaneous CODAR and OSCR measurements of ocean surface currents in Monterey Bay*, *Geoscience and Remote Sensing Symposium, 1996. IGARSS '96. 'Remote Sensing for a Sustainable Future.', International* **3** (1996) 1749–1752 vol.3.

[65] P. Stoica and R. L. Moses, *Spectral analysis of signals*. Pearson Prentice Hall, Upper Saddle River, NJ, 2005.

[66] A. F. Shchepetkin and J. C. McWilliams, *The regional oceanic modeling system (ROMS): A split-explicit, free-surface, topography-following-coordinate oceanic model*, *Ocean Modelling* **9** (2005), no. 4 347–404.

[67] D. E. Barrick and J. B. Snider, *The Statistics of HF Sea-Echo Doppler Spectra*, *IEEE Journal of Oceanic Engineering* **2** (1977), no. 1 19–28.

[68] A. Amar and A. J. Weiss, *Resolution of Closely Spaced Deterministic with Given Success Rate Signals*, *IEEE International Symposium on Information Theory, Nice* (2007) 1791–1795.

[69] W. J. Pierson and L. Moskowitz, *A proposed spectral form for fully developed wind seas based on the similarity theory of S. A. Kitaigorodskii*, *Journal of Geophysical Research* **69** (dec, 1964) 5181–5190.

[70] R. J. LeVeque, *Finite difference methods for ordinary and partial differential equations: steady-state and time-dependent problems*. SIAM, 2007.

[71] Y. I. Abramovich, B. A. Johnson, and X. Mestre, *DOA Estimation in the Small-Sample Threshold Region*, in *Classical and Modern Direction-of-Arrival Estimation* (T. E. Tuncer and B. Friedlander, eds.), ch. 7, pp. 219–287. Academic Press, 2009.

[72] A. Sentchev, P. Forget, Y. Barbin, and M. Yaremchuk, *Surface circulation in the Iroise Sea (W. Brittany) from high resolution HF radar mapping*, *Journal of Marine Systems* **109-110** (2013), no. SUPPL. 153–168.

[73] P. Forget, Y. Barbin, and G. Andre, *Monitoring of Surface Ocean Circulation in the Gulf of Lions (North-West Mediterranean Sea) Using WERA HF Radars*, *IGARSS 2008 - 2008 IEEE International Geoscience and Remote Sensing Symposium* (2008) I–375–I378.

[74] A. Orfila, A. Molcard, J. M. Sayol, J. Marmain, L. Bellomo, C. Quentin, and Y. Barbin, *Empirical forecasting of HF-radar velocity using genetic algorithms*, *IEEE Transactions on Geoscience and Remote Sensing* **53** (2015), no. 5 2875–2886.

[75] A. Kirincich, *The occurrence, drivers, and implications of submesoscale eddies on the Marthas Vineyard inner shelf*, *Journal of Physical Oceanography* **46** (2016), no. 9 2645–2662.

[76] A. Kirincich. personal communication.

[77] P. M. Kosro, *On the spatial structure of coastal circulation off Newport, Oregon during spring and summer 2001 in a region of varying shelf width*, *Journal of Geophysical Research C: Oceans* **110** (2005), no. 10 1–16.

[78] R. Castelao, S. Glenn, O. Schofield, R. Chant, J. Wilkin, and J. Kohut, *Seasonal evolution of hydrographic fields in the central Middle Atlantic Bight from glider observations*, *Geophysical Research Letters* **35** (2008), no. 3 6–11.

[79] B. M. Emery and L. Washburn, *Uncertainty Estimates for Oceanographic HF Radars, in prep.*, .

[80] J. Harlan, E. Terrill, and B. Burnett, *National high frequency radar network: Update*, in *OCEANS 2009, MTS/IEEE Biloxi-Marine Technology for Our Future: Global and Local Challenges*, pp. 1–7, IEEE, 2009.

[81] D. D. Crombie, *Doppler spectrum of sea echo at 13.56 Mc./s.*, *Nature* (1955) 681–682.

[82] D. E. Barrick, *First-order theory and analysis of MF-HF-VHF scatter from the sea*, *IEEE Transactions on antennas and propagation* **AP-20** (1972), no. 1 2–10.

[83] R. H. Stewart and J. W. Joy, *HF radio measurements of ocean surface currents*, *Deep Sea Research* **21** (1974) 1039–1049.

[84] C. C. Teague, J. F. Vesecky, D. M. Fernandez, and L. P. Atkinson, *HF radar instruments, past to present*, *Oceanography* **10** (1997), no. 0704 40–44.

[85] J. Martinez-Pedraja, L. K. Shay, B. K. Haus, and C. Whelan, *Interoperability of seasondes and wellen radars in mapping radial surface currents*, *Journal of Atmospheric and Oceanic Technology* **30** (2013), no. 11 2662–2675.

[86] M. Wax and T. Kailath, *Detection of signals by information theoretic criteria*, *Acoustics, Speech and Signal Processing* **33** (1985), no. 2 387–392.

[87] S. Y. Kim, E. J. Terrill, B. D. Cornuelle, AA, S. Y. Kim, E. J. Terrill, and B. D. Cornuelle, *Mapping surface currents from HF radar radial velocity measurements using optimal interpolation*, *Journal of Geophysical Research: Oceans* **113** (2008), no. 10 1–16.

[88] D. M. Kaplan and F. Lekien, *Spatial interpolation and filtering of surface current data based on open-boundary modal analysis*, *Journal of Geophysical Research: Oceans* **112** (2007), no. 12 1–20.

[89] M. Yaremchuk and A. Sentchev, *Mapping radar-derived sea surface currents with a variational method*, *Continental Shelf Research* **29** (2009), no. 14 1711–1722.

[90] F. Li, R. Vaccaro, and D. Tufts, *Min-Norm linear prediction for arbitrary sensor arrays*, *Acoustics, Speech, and Signal ...* (1989), no. 2 2613–2616.

[91] P. Stoica and A. Nehorai, *Performance Study of Conditional and Unconditional Direction-of-Arrival Estimation*, *IEEE Transactions on Acoustics, Speech, and Signal Processing* **38** (1990), no. 10 1783–1795.

[92] M. Viberg, B. Ottersten, T. Kailath, and M. V. Ottersten, *Detection and estimation in sensor arrays using weighted subspace fitting*, *IEEE Transactions on Signal Processing* **39** (1991), no. I 2436–2449.

[93] P. Stoica and K. C. Sharman, *Maximum likelihood methods for direction-of-arrival estimation*, *Acoustics, Speech and Signal Processing, IEEE Transactions on* **38** (1990), no. 7 1132–1143.

[94] B. A. Johnson, Y. I. Abramovich, and X. Mestre, *MUSIC, G-MUSIC, and maximum-likelihood performance breakdown*, *IEEE Transactions on Signal Processing* **56** (2008), no. 8 3944–3958.